FABRICATION OF PRISTINE AND DOPED GRAPHENE NANOSTRIPES AND THEIR APPLICATION IN ENERGY STORAGE

Thesis by

Jacob Bagley

In Partial Fulfillment of the Requirements for the Degree of

Doctor of Philosophy

CALIFORNIA INSTITUTE OF TECHNOLOGY

Pasadena, California

2021

(Defended Jan 25, 2021)

Jacob Bagley

ORCID: 0000-0001-9490-1341

Dedicated to my wife, Alina, for her resilience during this time

Acknowledgements

Both the starting and completion of this thesis would not have been possible without the support and influences of family, mentors, and co-workers. I will acknowledge these chronologically.

My parents deserve the first acknowledgement in this thesis. From an early age they fostered a love of learning, particularly in the sciences, and encouraged and valued the pursuit of higher education.

My two undergraduate research mentors, Professor Matthew Linford and Professor Jeremy Johnson, at Brigham Young University also deserve acknowledgement. It was while working in Professor Linford's research laboratory that I discovered the excitement of scientific research, and both Professor Linford and Professor Johnson provided excellent career and schooling advice.

My wife, Alina, must be acknowledged for her courageous and adventurous spirit in moving away from family and friends to start a new life, and also for her emotional support and encouragement throughout the time of my doctoral studies.

My research advisor, Professor Nai-Chang Yeh, deserves acknowledgement for organizing and leading our research group, wisely advising my research, teaching research skills, and supporting my experimental proposals. Our group staff scientist, Dr Marcus Teague, also provided sage research mentorship.

I also must acknowledge Professor Kimberly See and her research group members for providing technical knowledge and equipment that enabled me to complete significant parts of my doctoral research.

Abstract

Fossil fuel usage causing rising CO_2 levels and leading to climate change is, perhaps, the most pressing issue of our time. However, our economic dependence on energy necessitates its usage such that reducing energy usage is not possible leaving transitioning to renewable energy technologies as the only sustainable option. Currently, the largest barrier to large scale incorporation of renewable energy sources (*e.g.*, solar, wind) is the high cost of energy storage technologies. Electrochemical energy storage technologies (*e.g.*, lithium-ion batteries and supercapacitors) have been identified as a key approach for enabling the transition to renewable energy technologies.

Graphene is a material with exceptional properties that is receiving much attention for application in various energy storage technologies and could help reduce the cost of energy storage technologies. This thesis describes a novel fabrication procedure for low-cost and efficient synthesis of high quality graphene nanostripes (GNSPs) and their application in lithium-ion battery and supercapacitor electrodes.

This thesis is structured as follows. Chapter 1 outlines the motivation and technical background of this research. Chapter 2 describes the instrumentation and procedures for fabricating GNSPs. Chapter 3 describes *in situ* exfoliation of GNSPs as electrodes in supercapacitors to increase the capacitance. Chapter 4 describes synthesis and application of pyridinic-type nitrogen-doped GNSPs as a lithium-ion battery anode. Chapter 5 describes the synthesis and application of silicon-, germanium-, and tin-doped GNSPs and their application in lithium-ion battery anodes. Chapter 6 concludes and synthesizes the

findings of the thesis holistically. Additionally, future outlook and potential research objectives are presented.

Published Content and Contributions

1. Chen-Chih Hsu, **Jacob D. Bagley**, Marcus L. Teague, Wei-Shiuan Tseng, Kathleen L. Yang, Yiran Zhang, Yiliang Li, James M. Tour, N.-C. Yeh, High-yield single-step catalytic growth of graphene nanostripes by plasma enhanced chemical vapor deposition, *Carbon*, *129*, 537-536 (**2018**). DOI: 10.1016/j.carbon.2017.12.058

   J.D.B. made essential contributions for method development for GNSPs growth and exfoliation, including exploring alternate precursors, residual gas analyzer data curation and interpretation, scanning electron microscopy data curation and interpretation, Raman spectroscopy data curation, and mechanistic conjectures.

2. Nai-Chang Yeh, Chen-Chih Hsu, **Jacob Bagley**, Wei-Shiuan Tseng, Single-step growth of graphene and graphene-based nanostructures by plasma-enhanced chemical vapor deposition, *Nanotechnology*, *30*, 162001 (**2019**). DOI: 10.1088/1361-6528/aafdbf

   J.D.B. performed background research regarding vertically oriented graphene and participated in writing the section regarding vertically oriented graphene.

3. **Jacob D Bagley**, Deepan Kishore Kumar, Kimberly A. See, Nai-Chang Yeh, Selective formation of pyridinic-type nitrogen-doped graphene and its application in lithium-ion battery anodes, *RSC Advances*, *10*, 39562-39571 (**2020**). DOI: 10.1039/D0RA06199A

   J.D.B. conceived the synthesis procedure, fabricated materials, performed most characterizations, and participating in writing the manuscript.

4. **Jacob D Bagley**, Dorte R. Danielsen, Nai-Chang Yeh, Significant capacitance enhancement via *in situ* exfoliation of quasi-one dimensional graphene nanostripes in supercapacitor electrodes, accepted by *ACS Omega*.

   J.D.B. fabricated the materials, performed all characterizations except SEM, conceived exfoliation procedure, and participated in writing the manuscript.

5. **Jacob D Bagley**, Nai-Chang Yeh, Group IV element (silicon, germanium and tin)-doped graphene application in lithium-ion battery anode and implications on cause of capacity enhancement in doped graphene, *submitted*.

   J.D.B. conceived the synthesis procedure, fabricated materials, performed characterizations, and participated in writing the manuscript.

Table of Contents

List of Figures

List of Tables

List of Abbreviations and Symbols

AD	Access door
BDE	Bond dissociation energy
BrBz	Bromobenzene
CNT	Carbon nanotube
CPE	Constant phase element
CT	Cold trap
CVD	Chemical vapor deposition
DBB	Dibromobenzene
DBN	Dibromonapthalene
DCB	Dichlorobenzene
EDS	Energy dispersive spectroscopy
EIS	Electrochemical impedance spectroscopy
EV	Electric vehicle
FWHM	Full-width at half-maximum
Ge-GNSP	Germanium-doped graphene nanostripe
GNR	Graphene nanoribbon
GNSP	Graphene nanostripe
HIM	Helium-ion microscopy
IoBz	Iodobenzene
LIB	Lithium-ion battery
LV	Leak valve
MFC	Mass flow controller
MSE	Mean squared error

N-GNSP	Nitrogen-doped graphene nanostripe
NIST	National Institute of Standards and Technology
NMP	N-Methyl-2-Pyrrolidone
OES	Optical emission spectroscopy
P1	Precursor 1
P2	Precursor 2
PECVD	Plasma enhanced chemical vapor deposition
PG	Pressure gauge
PVDF	Polyvinylidene fluoride
RGA	Residual gas analyzer
RV	Regulator valve
SAD	Selected area diffraction
SBP	Substituted benzene precursor
SEI	Solid electrolyte interface
SEM	Scanning electron microscopy
Si-GNSP	Silicon-doped graphene nanostripe
Sn-GNSP	Tin-doped graphene nanostripe
SOC	State of charge
TEM	Transmission electron microscopy
TV	Throttle valve
UPS	Ultraviolet photoelectron spectroscopy
VOG	Vertically oriented graphene
VP	Vacuum pump
XPS	X-ray photoelectron spectroscopy
XRD	X-ray diffraction
μWA	Microwave antenna

C	Capacitance
d	Distance
E	Enhancement
I	Current
i	Imaginary number
I_{2D}	Raman *2D* peak intensity
I_D	Raman *D* peak intensity
$I_{D'}$	Raman *D'* peak intensity
I_G	Raman *G* peak intensity
l	Bragg order
L_a	Crystallite size
m	Mass
n	Constant phase element constant
Q	Constant phase element constant
R	Resistance
V	Voltage
Z	Impedance
θ	Angle
v	Scan rate

Φ	Work function
ω	Radial frequency

Chapter 1—Introduction

1.1 The Climate Crisis and Renewable Energy

1.1.1 The Climate Crisis

The Intergovernmental Panel on Climate Change reports with "high confidence" that irreversible climate damage will take place if greenhouse gas emissions are not substantially reduced within the decade.[1] Projected environmental damages include an increase in average global surface temperature, hot extremes in inhabited areas, heavy precipitation in some regions, drought and precipitation deficits in some regions, rising sea levels, reduction in biodiversity, and ecosystem destruction. Projected direct risks for humanity include heat waves, increased disease transmission (*e.g.*, malaria), reduction in crop and livestock yields, and reduction in fresh water supply. This demonstrates the pressing need to substantially reduce greenhouse gas emissions.

Globally, 72% of greenhouse gas emissions result from energy usage in the forms of electricity and heat, transportation, manufacturing and construction, fugitive emissions, and other fuel combustions.[2] Within energy usage, the primary greenhouse gas is CO_2, and the vast majority of CO_2 is produced from energy results from usage of fossil fuels (*e.g.*, coal, natural gas and oil).[3] As such, the greatest effort to mitigate climate change should be concentrated on reducing and/or eliminating the use of fossil fuels, which account for 85% of global energy usage.[4] However, energy usage is directly related to economic growth, reducing poverty, increasing living standards, and food and water production.[5] Therefore, reducing greenhouse gas emissions while avoiding a humanitarian crisis will require replacing fossil fuels with greenhouse gas emission-free energy technologies.

1.1.2 Energy Technologies to Combat Greenhouse Gas Emissions

A greenhouse gas emission-free energy infrastructure will involve the two components of I) emission-free energy production and II) energy storage.

Energy production

Compared to fossil fuels, both wind and solar power produces negligible greenhouse gas emissions,[3] and wind and solar power have the practical potential to supply several orders of magnitude more energy than the whole of humanity uses.[6] Additionally, in recent years the levelized unsubsidized cost of electricity produced from utility scale solar power has become cheaper than electricity produced from coal.[7] However, wind and solar energy output is variable and uncertain such that their energy supply does not typically match energy demand (*e.g.*, in a utility electrical grid).[8] Additionally, wind power and solar power are not effective in portable applications such as transportation. These barriers can be overcome by energy storage technologies.

Energy Storage

Efficient energy storage technology is key to enabling the widespread use of clean energy sources such as solar and wind power as well as making fossil fuels more efficient. Energy storage in the electrical grid can be used for load leveling, *i.e.*, storing energy during times when energy production is greater than energy demand, which is then used during times when energy production is lower than energy demand. Load leveling can enable, for example, solar power by storing excess energy produced during high solar output to be used during times of peak energy demand and dark times.[8] In addition, even under fossil fuel based energy production, load leveling via energy storage can still reduce carbon

emissions by improving energy efficiency, *e.g.*, energy can be stored during times of low demand and used during times of high demand, reducing the necessary base load.

Energy storage also enables portable electricity generation (*e.g.*, via batteries) which can reduce greenhouse gas emissions particularly in transportation, which currently relies on fossil fuels and accounts for ~ 11% of greenhouse gas emissions.[2] Energy storage for portable electricity generation in transportation can reduce greenhouse gas emissions by enabling the use of energy derived from renewable sources (*e.g.*, solar) and also by utilizing energy from fossil fuels more efficiently. Electric cars, for example, use fossil fuel energy more efficiently than internal combustion engine vehicles (gasoline and diesel) when considering the entire energy cycle,[9] in part because electric motors have a typical efficiency of > 77%, whereas internal combustion engine motors typically have an efficiency of 12% ~ 30%.[10,11]

Despite the advantages of grid scale energy storage and electric vehicles, the current global energy storage capacity is just 8 GWh,[12] which is only 0.06% of the total energy consumption (13.8 TWh),[4] reflecting the reality that energy storage technologies are not yet widely used. For energy storage to become economically relevant (and thus widely used) in utilities and transportation, the following five figures of merit must be considered: *i*) energy density (the amount of energy stored per unit weight or unit volume), *ii*) power density (the power, *i.e.*, the rate of work output per unit weight or unit volume), *iii*) lifetime, *iv*) safety/toxicity and *v*) cost. Each application of energy storage has different requirements for each of these aspects, but, in general, energy storage technology needs to improve in each category. Currently, pumped hydro-electric power (*e.g.*, energy stored via dams) accounts for 96% of the global energy storage capacity and is a cost effective and well-

established technology. However, hydro-electric power cannot meet the world energy storage demand because it has low energy density, is geographically limited, and has a substantial environmental impact.[13,14]

Amongst the technologies that are expected to provide an advantage to grid scale energy storage are lithium-ion batteries, flow batteries, supercapacitors and fuel cells.[14] Lithium-ion batteries have a relatively high energy density, but are expensive and have low power density. Flow batteries have a long lifetime, but low energy density and power density and involve hazardous chemicals. Supercapacitors have long lifetimes and high power densities, but have low power densities and are expensive. Fuel cells have very high energy density, but are expensive.[13,14] Each of these technologies has merits, but each must be improved to be economically relevant either individually or in combination.

As an alternative energy source for transportation, lithium-ion batteries in particular are growing in market acceptance. Lithium-ion batteries are used in electric vehicles (EVs) to entirely replace the internal combustion engine and in hybrid vehicles to complement the internal combustion engine to reduce fossil fuel consumption. Currently, electric vehicle usage is primarily limited by technological factors, *i.e.*, high cost (due to battery costs), limited driving range (due to insufficient energy density), limited trunk space (due to large batteries) and low top speed (due to insufficient power density).[15–19] Therefore, we can expect that improvements in lithium-ion battery cost and energy and power densities will enable improved adoption of EVs.

Supercapacitors are also receiving attention as a potential energy source in transportation. Due to their low energy densities, supercapacitors could not be a vehicle's

sole power source; rather, the fast charging/discharging enabled by their high power densities make supercapacitors a promising technology for regenerative braking, *i.e.*, supercapacitors could charge during vehicle braking and discharge during acceleration.

Many technologies are being explored to improve energy storage technologies. Because lithium-ion batteries and supercapacitors already have some market penetration, they are receiving particular research attention. Nearly every aspect of lithium-ion batteries is being considered for improvement including altering anode and cathode materials,[20] electrolytes,[21,22] and separators.[23] Supercapacitors are receiving similar attention.[24] Of the materials being explored for lithium-ion battery and supercapacitor electrodes, graphene and modified graphene materials demonstrate appealing properties including high energy and power densities.

1.2 Graphene

1.2.1 Graphene Structure and Properties

Graphene was first isolated in 2004, and its interesting structure and properties gave rise to a landslide of fundamental research and applications.[25] Graphene is a two-dimensional (2D) sheet of carbon atoms arranged in a repeating hexagonal pattern resembling a honeycomb lattice. Common carbon materials such as graphite, carbon nanotubes and fullerenes are derived from graphene (**Figure 1.1a**[26]). The electrons of the carbon atoms in graphene are sp^2 hybridized, and carbon atoms bond to their nearest neighbors by sp^2 σ bonds. The final p orbital of the carbon atoms is perpendicular to the planar structure, and all of the perpendicular p orbitals bond to form a π band of delocalized electrons throughout the graphene lattice.[25,26]

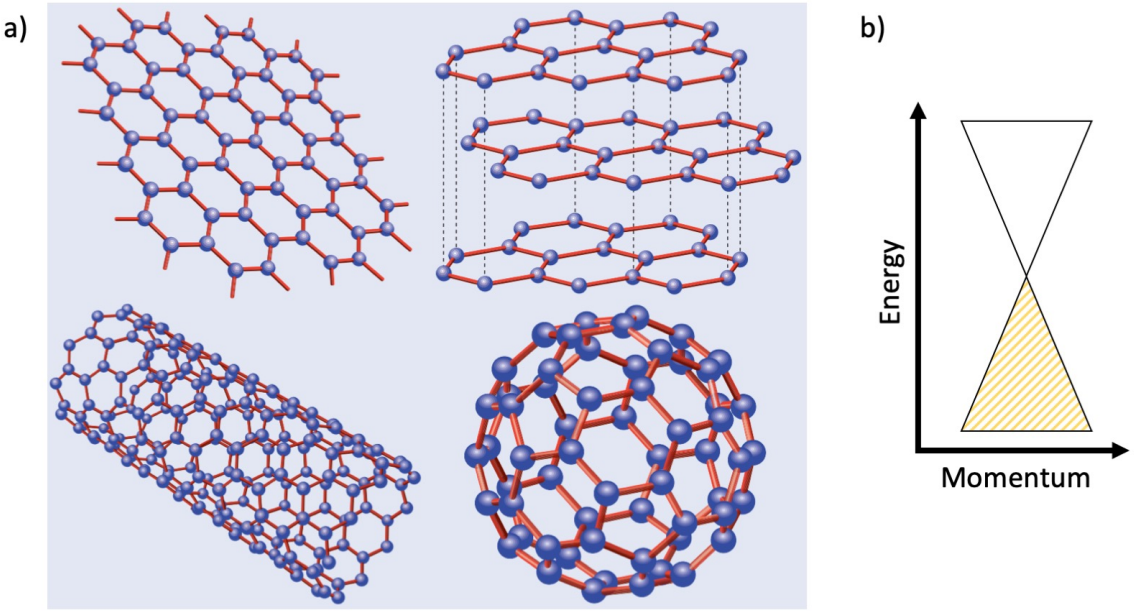

Figure 1.1: (a) Graphene and graphene-derived allotropes. Reproduced from reference[26] (b) The energy-momentum dispersion relation of graphene at one of the inequivalent valleys (K and K′) in the first Brillouin zone. The conduction band and valence band merge at the Dirac point and the Fermi level of undoped graphene locates at the Dirac point so that graphene is a semi-metal.

The graphene structure results in many spectacular properties. The π band results in the electronic band structure shown in **Figure 1.1b**. The linear dispersion in the energy-momentum relationship is termed a "Dirac cone" and gives graphene the highest known electron mobility in graphene due to the massless nature of Dirac fermions.[25] Mechanically, graphene also has the highest recorded tensile strength of any material.[27] As a 2D material, graphene has extremely high surface area. Additionally, graphene demonstrates chemical stability in electrochemical applications, yet also demonstrates sufficient chemical reactivity to be functionalized to lend it novel properties.[28]

1.2.2 Graphene in Electrochemical Energy Storage

The properties of graphene are being extensively exploited for application in electrochemical energy storage including supercapacitor electrodes and lithium-ion battery anodes.

Supercapacitor electrodes

A supercapacitor consists of two electrodes separated by an electrolyte, and upon an applied voltage bias, cations and anions in the electrolyte migrate to the negatively and positively biased electrodes, respectively, as shown in **Figure 1.2**. The ions cover the surface of the electrodes, but (in an ideal supercapacitor) do not participate in any faradaic charge transfer reactions. That is, electrons do not transfer between electrodes and ions, and the energy storage mechanism is capacitive, *i.e.*, energy is stored by the potential energy of separated charges. Therefore, the electrode surface (and its surface area, in particular) is the primary factor determining performance of a supercapacitor electrode material. Mathematically this is described as $C = A\varepsilon_0 / d$, where C is the electrode

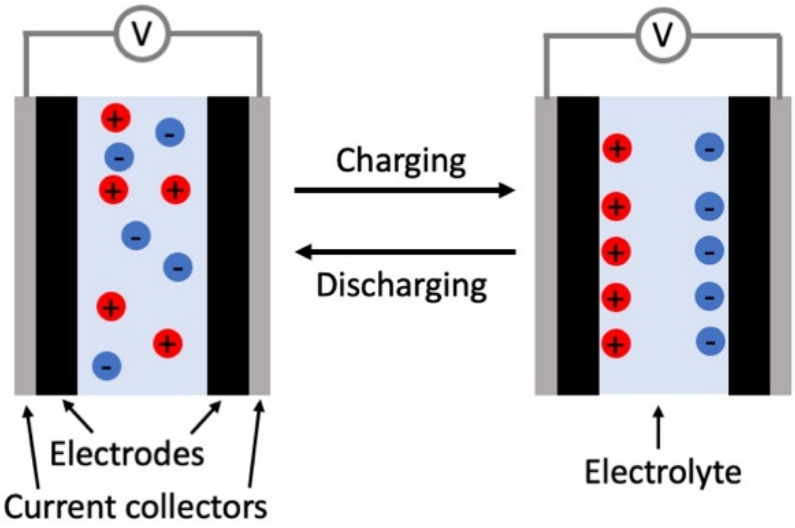

Figure 1.2: Supercapacitor diagram and charge storage mechanism.

capacitance, A is the electrode surface area, ε_0 is the permittivity of free space and d is the distance between the ions in solution and the mirror charges in the electrode.[29] Graphene as a 2D material has high surface area and is an appealing material for supercapacitor electrodes.

The energy storage in a supercapacitor electrode is described mathematically as $E = CV^2$, where E is energy, C is capacitance and V is the voltage difference between charged and discharged states. The energy stored in a supercapacitor electrode then can be increased by increasing the capacitance (which depends strongly on surface area) and the voltage. However, because energy increases quadratically with voltage, electrode materials will perform best if they are stable under large voltage biases as graphene is.[30] (This is also true of the electrolyte, but that is beyond the scope of this thesis.)

Even when the supercapacitor surface area and operating voltage are maximized, however, the capacitive energy storage mechanism results in relatively low energy densities (compared to batteries, fuel cells, fossil fuels, etc).[31] Although practical applications require a certain amount of energy density which researchers are striving to improve, the practical advantage of supercapacitors is their power density rather than their energy density. Because the capacitive energy storage mechanism is free from kinetically sluggish charge transfer reactions, the fundamental process of capacitive energy storage is very fast such that electrode materials must have good electron mobility in order to match the speed of the capacitive process. Graphene, as the material with the highest electron mobility, is ideal for high power density supercapacitors.

Although graphene has many ideal properties for supercapacitors, in practice these properties are difficult to exploit. Achieving a large active surface area and maintaining the high electron mobility are particularly difficult. When packaged into an electrode, graphene sheets tend to stack together, losing the advantage of its high surface area.[32] To combat this problem, many researchers are striving to fabricate three-dimensional (3D) graphene structures where graphene sheets are bonded together in skew configurations resulting in a robust porous network of graphene materials.[33] Though this method increases the surface area, it compromises the graphene crystal structure and reduces the electron mobility, which affects the resulting supercapacitor's power density. Researchers are currently searching for methods/configurations that preserve the high electron mobility of graphene yet enable high electrolyte coverage of the graphene.

Lithium-ion battery anodes

Similar to supercapacitors, lithium-ion batteries consist of two electrodes and an electrolyte. Contrary to supercapacitors, the primary energy storage mechanism in lithium-ion batteries involves faradaic charge transfer. $LiCoO_2$ and graphite are typical lithium-ion battery cathode and anode materials, respectively. Energy is stored under appropriate voltage bias according to

$$6C + LiCoO_2 \rightarrow Li_xC_6 + Li_{1-x}CoO_2$$

where 6C represents graphite. That is, electrons transfer away from lithium atoms in $LiCoO_2$ such that become Li^+ exits the crystal and enter the electrolyte, and electrons transfer to Li^+ in the electrolyte to incorporate it into the graphite crystal structure.[34]

The work in this thesis is focuses on the graphite anode where lithium intercalates between individual graphene sheets with a theoretical maximum capacity corresponding to LiC_6. The faradaic charge transfer that enables a high lithium storage capacity in graphite depends on this intercalation involving a phase change.[35] Given that the faradaic charge transfer requires an intercalation medium, graphene (a single layer of graphite) itself cannot participate in faradaic charge transfer and has a low lithium storage capacity. However, similar to supercapacitors, when graphene is packaged into an electrode, graphene sheets tend to stack together and form turbostratic graphite, a graphite material where individual graphene sheets may have good crystalline order, but their stacking is disordered. Turbostratic graphite, unlike single graphene sheets, can intercalate lithium and participates in faradaic charge transfer to enable high lithium storage capacity.[36]

When packaged into an electrode, if graphene simply forms a graphitic material, what is the motivation for using graphene in the first place? The answer is that using graphene is effectively a bottom-up synthesis of graphite such that the properties of the electrode can be tailored, and by doing so the lithium storage capacity can be enhanced beyond the theoretical capacity of graphite. The two methods that are typically used to boost lithium storage capacity of graphene materials is inducing disorder and incorporating heteroatom dopants. Disordered graphene materials are conjectured to store additional lithium at defect sites or to be able to intercalate more lithium due to increased interlayer spacing.[35,37] Heteroatom dopants (*e.g.*, nitrogen, boron, phosphorus, etc.) also enhance lithium storage capacity allegedly because they have higher lithium affinity than carbon. In this field, research is focused on developing synthesis methods to incorporate dopants and increase the lithium storage capacity of graphene while maintaining good cycle life.

1.3 Large Scale Graphene Synthesis Methods

Practical application of graphene in energy storage devices typically requires a large-scale synthesis method in order to have a sufficient amount of graphene material. Several typical large-scale synthesis methods are introduced here.

1.2.1 Exfoliation of Graphite

The first method to produce graphene was the scotch tape exfoliation method that resulted in the Nobel Prize where graphene layers are successively peeled off a graphite sample using scotch tape until a single layer of graphene is obtained.[38] This method itself is not a large-scale synthesis method of graphene, but it inspired many exfoliation methods that are large-scale.

Liquid phase exfoliation

Liquid phase exfoliation of graphite to produce graphene involves putting a graphite sample in some liquid and sonicating it to separate it into individual layers. This process has been demonstrated to produce single-layer graphene in high yields. Exfoliation becomes possible in liquids that have a surface tension comparable to graphene such that solvent molecules can wedge between individual layers. The advantages of this method are that it is low cost and scalable. The disadvantages are that the solvents that happen to work well (*e.g.*, N-methyl pyrrolidine) are toxic and have high boiling points, it is time intensive, and the exfoliation procedure tends to break graphene domains into smaller pieces.[39,40]

Chemical exfoliation

Chemical exfoliation of graphite typically takes place in aqueous solution with strong oxidizers that oxidize graphene sheets such that they become soluble in aqueous

solution and separate into single layers of graphene oxide. The graphene oxide can then be chemically reduced to graphene resulting in single layers of graphene. The advantages of this method include its scalability and that it takes place in aqueous solution using common chemicals. Disadvantages include that it involves toxic chemicals, it is time intensive, and the resulting graphene material is highly defective and contaminants can be difficult to remove.[41]

Electrochemical exfoliation

Electrochemical exfoliation involves separating graphite to single layers of graphene by applying a voltage bias to intercalate ions. Advantages of this method include control over the degree of exfoliation and that it is relatively fast. Disadvantages include that the graphene is typically functionalized/contaminated during exfoliation.[42]

1.2.2 Chemical Vapor Deposition

Chemical vapor deposition (CVD) is a standard industrial process involving the mixture of chemicals in vapor phase in a reaction chamber to fabricate some material on a substrate. To overcome reaction energy barriers, the chamber is often heated and/or includes a plasma source. Thermal CVD of graphene has been extensively studied and has been shown to produce large-area single-layer graphene. However, this method is time consuming and expensive. In particular, it cannot produce graphene in high yield, which is necessary for application in energy storage.[43]

Plasma enhanced CVD (PECVD), on the other hand, can produce either large-area single-layer graphene or vertically oriented graphene, depending on growth parameters. Vertically oriented graphene (VOG), also known as carbon nano-walls, is a class of

graphene materials that grow vertically with respect to the growth substrate such that the graphene sheet is perpendicular to the substrate. This configuration has the advantage that large amounts of graphene can be fabricated per unit of substrate area, *e.g.*, enough for application in energy storage applications. Scanning electron microscope (SEM) images of a VOG material is provided in **Figure 1.3**.[44] **Figure 1.3A** is a normal incidence image that shows the random orientation and branching nature of VOG materials. **Figure 1.3B** is a cross sectional image showing that VOG materials can be a dense "forest" of graphene, demonstrating that fabricating graphene in this method can yield large amounts of graphene.

Bo *et al*[45] wrote an extensive review in 2013 about the growth of vertically oriented graphene including a discussion of the effects of plasma sources, chemical precursors, substrate heating, chamber pressure, and substrate choice, and the author recently participated in a mini update review discussing advances in fabrication and characterization.[46] These reviews can be referenced for a detailed description of the field, but a brief summary will be provided here.

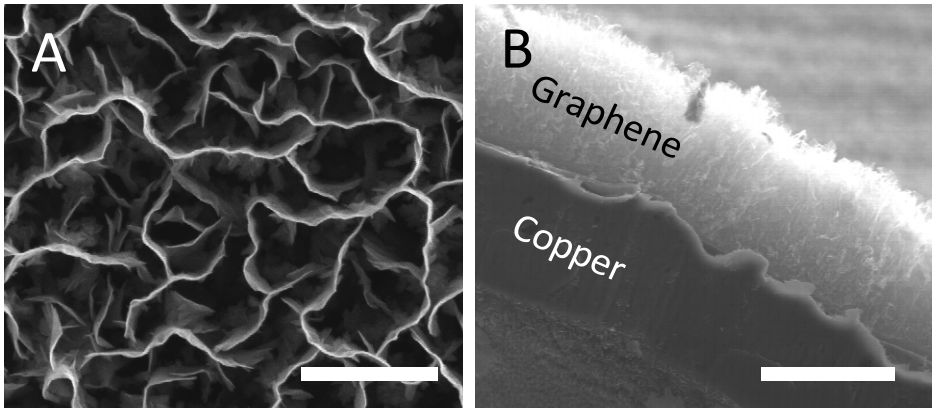

Figure 1.3: Normal incidence (scale bar: 2 µm) (A) and cross sectional (scale bar: 20 µm) (B) SEM images of a VOG material.

Growth of VOG traditionally requires a carbon precursor (*e.g.*, methane), a carbon etchant (*e.g.*, hydrogen), a heated substrate (*e.g.*, copper heated to 700 K) and a plasma source (*e.g.*, a microwave cavity). The carbon precursor contributes to growth while the carbon etchant removes defects, ensuring good crystalline quality, the plasma source creates reactive radicals from the carbon source and etchant and the heated substrate overcomes energy barriers to growth. Adjusting parameters may result in varying defect content, sheet size, growth rate, *etc*.

1.4 VOG in Electrochemical Energy Storage

The subject of this thesis is advancements that the author developed in the fabrication, characterization and application of VOG in electrochemical energy storage. In particular, we developed a room temperature synthesis of VOG (*i.e.*, without substrate heating) with high aspect ratios (*e.g.*, graphene sheets with dimensions 400 nm x 70 μm) and high yield. Due to the high aspect ratios we term our material graphene nanostripes (GNSPs). In the broad context of graphene synthesis, GNSPs are unique in that they are a single-step, room-temperature, and high yield synthesis of graphene with good crystallinity. Additionally, we developed a procedures for chemical doping of GNSPs and studied doped and undoped GNSPs in lithium-ion battery applications and supercapacitor applications.

Chapter 2—Synthesis of GNSPs

In this chapter, we will describe our developments regarding the synthesis of GNSPs and the procedures for scaling to high yield. We also discuss the growth mechanism of GNSPs and the doping procedures and present the characterizations of both undoped and doped GNSPs.

2.1 GNSPs growth instrumentation and characterization

At the time of writing this thesis we have used three separate deposition systems for fabrication of GNSPs, and although each system is unique, all systems contain the same fundamental which include a methane source, a hydrogen source, a substituted benzene precursor (SBP) source, a plasma source and a low pressure chamber. The initial deposition system (termed "generation 0" here) was retrofitted to accommodate the requirements of this fabrication. Then the following deposition systems ("generation I" and "generation II") were designed and built specifically for this synthesis, and each progressive deposition system was designed to produce GNSPs in higher yield. In the following, the physical components and experimental parameters that result in GNSPs growth for each of these systems will be described, and perspectives on scaling this process to an industrial scale will be provided.

2.1.1 Generation 0 GNSPs growth system description and performance

The generation 0 growth system, its performance and the motivation for growth of GNSPs was described in detail in a publication. Here an adapted version of that publication is provided, which includes additional details and further insights that we have gained since its publication.

Adapted from

> C.-C. Hsu, J. D. Bagley, M. L. Teague, W.-S. Tseng, K. L. Yang, Y. Zhang, Y. Li, Y. Li, J. M. Tour, N.-C. Yeh, High-yield single-step catalytic growth of graphene nanostripes by plasma enhanced chemical vapor deposition. Carbon 129, 527-536 (2018). DOI: 10.1016/j.carbon.2017.12.058

Personal contribution: Made essential contributions for method development for GNSPs growth and exfoliation, including exploring alternate precursors, residual gas analyzer data curation and interpretation, scanning electron microscopy data curation and interpretation, Raman spectroscopy data curation, and mechanistic conjectures.

Introduction

Among many intriguing properties and promising applications of graphene-based materials,[25,47,48] reduced dimensional graphene nanostructures, such as graphene nanoribbons (GNRs) that often refer to one-dimensional crystals with nanoscale widths, have attracted much attention for their quantum confinement effects in extremely narrow ribbons,[49,50] novel edge characteristics,[25,51–53] mechanical strength,[54,55] and a wide range of technological prospects in such areas as nano-electronics,[56–60] spintronics,[61,62] plasmonics,[63–65] biosensors,[66,67] energy storage,[68] and energy production.[69]

One of the primary challenges to fully realize the technological promises of reduced dimensional graphene nanostructures is to reliably produce a large quantity of high-quality nanomaterials with large aspect ratios. In general, the structural and physical properties of reduced dimensional graphene nanostructures are strongly depending on the synthesis method. To date, the best known methods for synthesizing quasi-one dimensional graphene nanostructures include the following primary categories: [1] The top-down approach, which utilizes lithographic techniques to produce GNRs from two-dimensional graphene sheets on a substrate. The quantities of GNRs thus produced are limited due to the time

consuming lithographic processes, and the edges of these GNRs are usually jagged.[70,71] [2] The bottom-up approach, which may be further divided into the surface-assisted[72,73] and solution-phase synthesized[74–80] approaches. The surface assisted method involves pre-synthesis of polymer chains on metallic substrates and has the advantage of achieving atomically precise armchair- or zigzag-edges.[52,53,72,73] However, this approach generally involves multiple steps of processing, which leads to very low yields and relatively short GNRs. Moreover, these GNRs are not easily transferrable to other substrates. Similarly, the solution-phase synthesized approach also involves multiple steps and the resulting GNRs exhibit a range of controlled widths on the order of 1–2 nm and typical lengths over 100 nm.[74–80] While both types of bottom-up approaches can achieve better control of the structures of GNRs, the complexity in the synthesis procedures and the relatively low yields are not ideal for mass production in large-scale applications. [3] Unzipping carbon nanotubes (CNTs): Multi-walled CNTs can be unzipped along the longitudinal direction to form GNRs.[81,82] Compared to the first two methods, this approach has the potential of mass production and lower costs. However, the process is time consuming and also requires initial mass production of CNTs. The GNRs thus produced also contain excess metallic impurities.[83,84] [4] Growth by thermally assisted plasma enhanced chemical vapor deposition (PECVD): Synthesis of vertically oriented graphene "nanowalls" or "nanosheets" by means of PECVD have been reported for a variety of precursor gases.[45,85] However, this method faces three major challenges: [44] First, all processes reported to date involve multiple steps of pretreatment of the substrates as well as high-temperature (ranging from 500 °C to 1150 °C) substrate heating and high plasma power (>10^2 W and up to ~ 10^3 W) during the graphene growth.[45,85] Second, the yields are generally too low to

be practical for mass production.[45,85] Third, the morphology and structures of vertically grown graphene nanosheets are not well controlled[45,85] because the growth mechanisms under different growth parameters and precursor molecules are not fully understood.

To overcome the aforementioned challenges, we report in this work a new single-step seeded growth method of "graphene nanostripes" (GNSPs) by PECVD techniques that can achieve high-yield and high-quality growth of GNSPs reliably without any active heating. The lengths of these GNSPs range from a few to tens of micrometers and the widths range from tens to hundreds of nanometers. Therefore, they exhibit large aspect ratios (typically from 10:1 to 130:1) but do not manifest effects of quantum confinement. Further, their widths are typically narrower than most nanowalls and nanosheets reported to date.[45,85] Therefore, we refer these quasi-one dimensional nanostructures to "graphene nanostripes" (GNSPs) to indicate their large aspect ratios and to differentiate them from GNRs that exhibit quantum confinement and also from graphene nanosheets[45] or nanowalls[85] that are generally wider and are with smaller aspect ratios than our GNSPs.

In comparison with our single-step PECVD growth process of high-quality large graphene sheets laterally on copper substrates without active heating,[86] these GNSPs of large aspect ratios are grown vertically on various transition-metal substrates by PECVD with the addition of substituted aromatics such as 1,2-dichlorobenzene (1,2-DCB), 1,2-dibromobenzene (1,2-DBB), 1,8-dibromonaphthalene (1,8-DBN) and toluene as the seeding molecules. Among these substituted aromatics, we find that 1,2-dichlorobenzene (1,2-DCB) is most effective for the growth of GNSPs at room temperature, as detailed in the supplementary information. Therefore, we focus hereafter on the studies of PECVD-grown GNSPs that are seeded by 1,2-DCB.

The entire growth process occurs in a single step within less than 20 min at a relatively low plasma power (≤60 W), and the resulting GNSPs exhibit large aspect ratios and high yields. Studies of the Raman spectroscopy, scanning electron microscopy (SEM), transmission electron microscopy (TEM), energy dispersion x-ray spectroscopy (EDS), ultraviolet photoemission spectroscopy (UPS) and electrical conductivity all confirm the high quality of the GNSPs thus obtained. Based on these experimental findings together with data from the residual gas analyzer (RGA) spectra and optical emission spectroscopy (OES) taken during the plasma process, we propose a growth mechanism and suggest that the introduction of substituted aromatics in the hydrogen plasma plays a critical role in achieving rapid vertical growth of GNSPs with high aspect ratios.

Experimental

Experimental setup. A schematic of this system is provided in **Figure 2.1a**. Methane (Airgas, 99.999%), argon (Airgas, 99.999%) and hydrogen (Airgas, 99.999%) gases are injected into the system from high pressure gas cylinders with the flow rate controlled either by automated mass flow controllers (MFCs, MKS Instruments) or manual leak valves. The SBPs (*e.g.*, 1,2-DCB) are liquid at room temperature and are placed in a vacuum sealed vial which is connected to the system via manual leak valve. The SBPs are not introduced to the system as liquids; rather, they are introduced via vapor phase, relying on room temperature evaporation.

The gases enter a ½" outer diameter quartz tube which is where the deposition takes place. The quartz chamber is fitted with an Evenson microwave cavity (Opthos, Inc.),

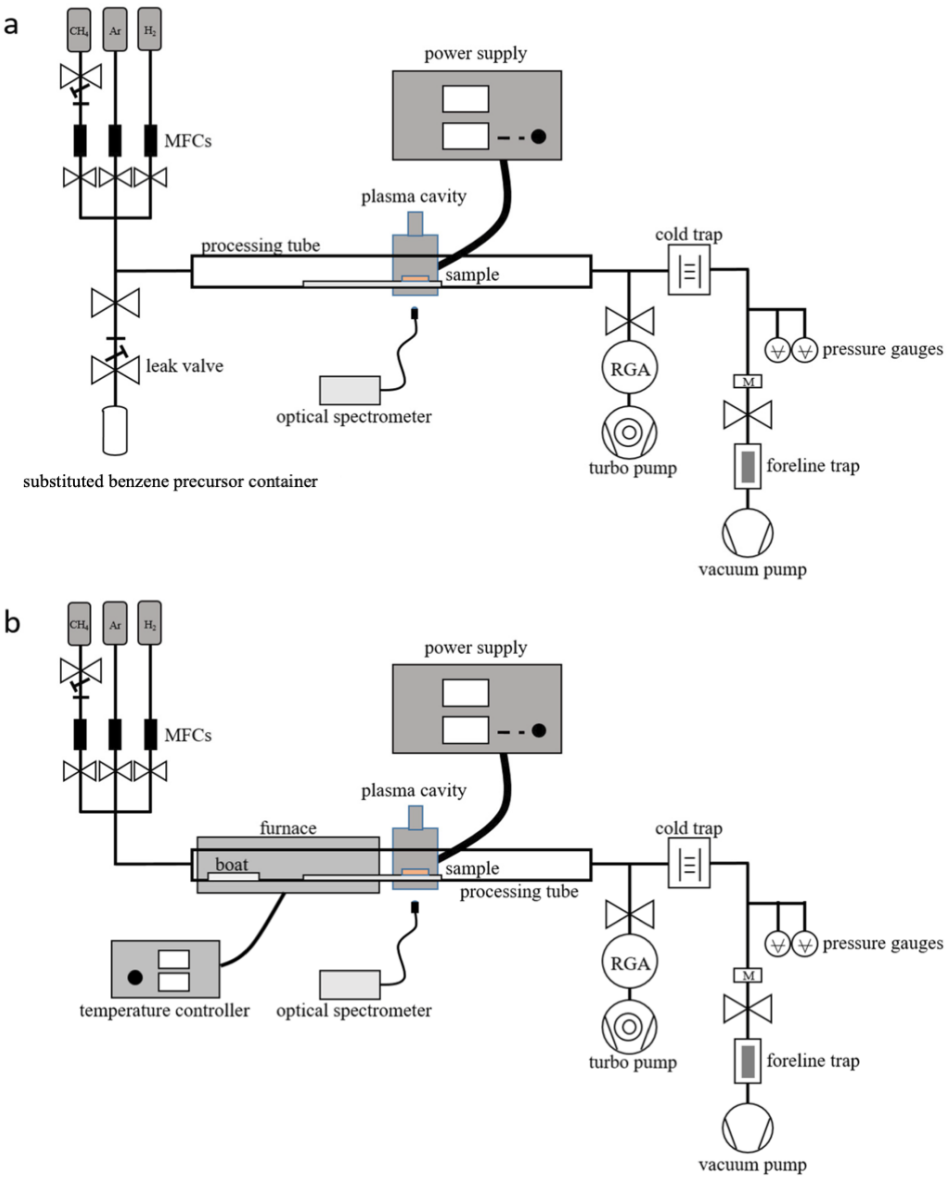

Figure 2.1: Schematic of generation 0 GNSPs deposition system. (a) A schematic of the experimental setup used for 1,2-DCB and 1,2- DBB. We control the partial pressures of 1,2-DCB and 1,2- DBB via a leak valve between the molecule container and growth chamber. (b) A schematic of the experimental setup used for 1,8-DBN. The precursor was heated from 60 °C to 100 °C to introduce different precursor partial pressures.

which resonates microwave radiation provided by the microwave power source (Opthos, Inc.) to create constructive interference of microwaves. In order to ensure the resonance condition in the Evenson cavity, the cavity includes two tuning rods that are adjusted to maximize transmission of the microwave radiation, as determined by minimizing the

"reflected power" signal on the microwave power source. Within the region of the deposition chamber that is fitted with the Evenson cavity the electric field is strong enough to maintain a plasma at the reduced pressure inside the chamber. A copper foil on a quartz boat is inserted in the chamber, and the Evenson cavity is placed near the copper foil.

After the gases flow through the quartz chamber they enter a junction with one path leading to the primary vacuum pump of the system and the other path leading a residual gas analyzer (RGA, Stanford Research Systems). An RGA is an electron-ionization quadrupole mass analyzer, *i.e.*, it detects the masses of molecules (and their fragments) present in the gas, which we use to determine the composition of gas in the system. The path to the RGA goes through a ~ 1 m long capillary then enters the ultrahigh vacuum RGA chamber. The capillary creates a pressure gradient between deposition chamber (held at medium vacuum) and the RGA chamber. The RGA is pumped by a turbomolecular vacuum pump (Pfeiffer, HiPace 80) and a mechanical roughing pump (Agilent, DS 102). I also note that the RGA does not directly measure the concentration of components in the system because i) molecules may have differing rates of diffusion into the RGA and ii) the electron-ionization process fragments molecules at differing rates.

The other path at the junction after the quartz chamber leads to the primary vacuum pump of the deposition system. Due to corrosive nature of SBPs and their reaction byproducts during deposition, vapor traps are used to protect the vacuum pump. Here we use a liquid nitrogen cold trap, wherein the chamber gases flow past a compartment that is chilled with liquid nitrogen (the liquid nitrogen is not in the chamber—it is in a compartment which is in physical contact with the chamber). Upon contact with the liquid nitrogen-cooled compartment, hazardous gases condense in the cold trap.

Downstream of the cold trap are two pressure gauges (MKS Instruments) and then an automated regulator valve (MKS Instruments, 153D) that opens/closes to achieve a user defined set point pressure. Next is a foreline trap that ensures oil from the pump does not travel upstream and contaminate the system, and finally the gases leave the system through a mechanical roughing pump (Agilent, DS102). A final component of the system is an optical emission spectrometer (OES) that measures radiation emitted from the plasma. The OES does not play a role in the GNSPs fabrication, but can be used to characterize the composition of the plasma.

The adjustable parameters in this system are MFC gas flow rates (1 ~ 100 sccm), the fraction that leak valves are open, input microwave radiation power (0 ~ 100 W) and the chamber pressure (the two pressures gauges have respective ranges of 0.01 ~ 10 Torr and 1 ~ 1000 Torr, but the practical pressure range of deposition is 0.1 ~ 30 Torr as pressures lower than ~ 0.1 Torr are not achievable while gases are being injected, and the cavity cannot sustain a plasma at pressures above ~ 30 Torr).

Additionally, the size of the copper foil growth substrate is important. For example, when using copper foil that is 50 μm thick, the areal size of the copper foil must be less than ~ 1 cm^2, or growth would not occur. Conversely, for thin films of copper (thickness < 1μm) no areal constraints were found. This phenomenon may be attributed to heating of the copper substrate. This is, since copper has a high thermal conductivity,[87] a large and thick copper substrate enables plasma-induced heat to be transferred away so that the reduced temperature of the substrate inhibits GNSPs growth. This is not a problem in thinner copper substrates because they have a lower heat capacity (due to a smaller volume)

and so maintain a higher temperature despite the potential heat transfer away from the plasma growth area.

1,8-DBN is a solid at room temperature and has a low vapor pressure, so placing it in the SBP precursor vial was ineffective. Instead, we used the schematic shown in **Figure 2.1b**. Here, 1,8-DBN was placed on a boat in the chamber upstream of the copper growth substrate, and the 1,8-DBN was heated to vaporize it for growth of GNSPs.

Growth of GNSPs. The quartz tube was pumped down to 27 mTorr. During the growth, the total pressure of the tube was maintained at 500 mTorr with 2 sccm hydrogen. The additional methane and 1,2-DCB was controlled by a precision leak valve and the partial pressure was monitored by a RGA. Typical methane and 1,2-DCB partial pressures were $(10 \sim 900)\times10^{-9}$ Torr and $(1 \sim 10)\times10^{-9}$ Torr, respectively, as measured in the RGA. Hydrogen plasma was formed away the substrate and then moved to the substrate in order to prevent any plasma transient damages. Typical plasma power ranged from 40 to 60 W with a plasma size of $1 \sim 2$ cm^3, and growth time ranged from 0.5 to 20 min.

Characterization. The PECVD-grown GNSPs were characterized by Raman spectroscopy, UPS, XPS, SEM, TEM and electrical conductivity studies. Raman spectra were taken via a Renishaw M1000 micro-Raman spectrometer system using a 514.3 nm laser (2.41 eV) as the excitation laser source. The laser spot size was ~1 μm in diameter and the exposure time was 30 s. A 50 × objective lens with a numerical aperture of 0.75 and a 2400 lines/mm grating were chosen during the measurement to achieve better signal-to-noise ratio. The UPS were performed via the Kratos-Ultra-XPS model which uses a magnetic immersion lens with a spherical mirror and concentric hemispherical analyzers

with a delay-line detector for both imaging and spectroscopy. He I (21.2 eV) were used as excitation sources for UPS measurement in an ultrahigh vacuum chamber with a base pressure of 2×10^{-10} Torr. The SEM images were taken by a FEI Nova 600 SEM system with the following parameters: acceleration voltage = 5 kV, beam current = 98 pA, and working distance ~5 mm. The TEM measurements were performed on a FEI Tecnai TF30 STEM (TF30) with an operating voltage of 300 KV. The electrical conductivity measurements were made by means of the four-probe method on GNSPs aligned on patterned electrodes via electrophoresis techniques.

Results

The seeded PECVD growth process is schematically illustrated in **Figure 2.2a**. We use 1,2-DCB to act as seeds for vertically aligned carpets of GNSPs grown on Cu surfaces. The hydrogen plasma with a slight trace of CN radicals is used to remove the surface copper oxide and expose fresh copper surface upon which 1,2-DCB molecules can seed,[85] resulting in the initial formation of vertical GNSPs. Additionally, methane is introduced into the hydrogen plasma as another carbon source to enhance the growth rate. We have also demonstrated the feasibility of using other carbon based, substituted aromatics such as 1,2-DBB, 1,8-DBN, and toluene as precursors and different transition-metal substrates (such as Ni foam and Ni foil besides Cu foil).

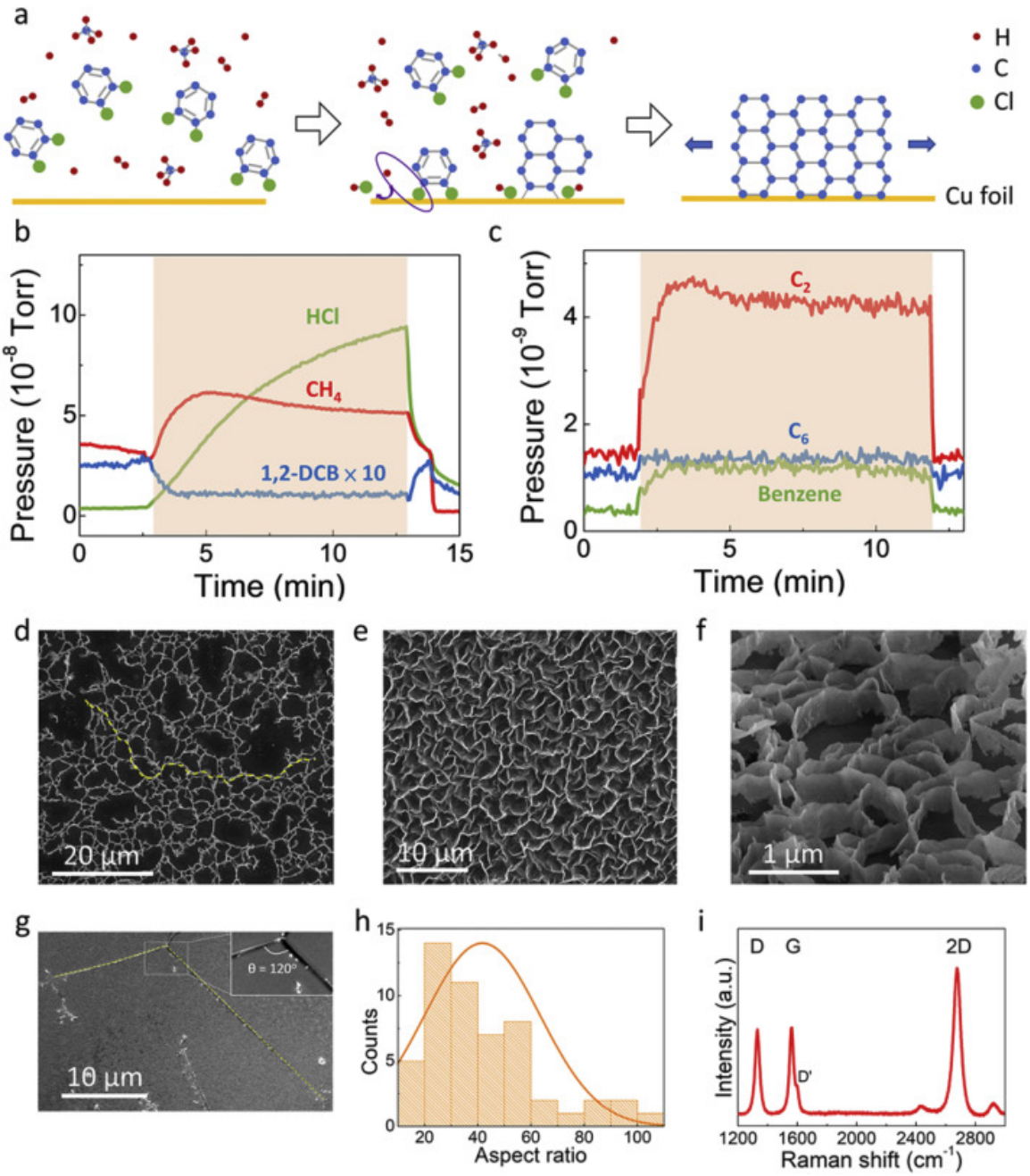

Figure 2.2: (a) Schematic illustration of the seeded growth process of PECVD-grown GNSPs. (b)–(c) RGA spectra of gas pressures in the growth chamber as a function of time, where the shaded area indicated the duration of the plasma process. (d)–(e) Two representative SEM images of the top view of GNSPs on Cu foil fabricated by PECVD with 1,2-DCB molecules for 10 min (f) SEM image of the tilted view (at 52°) of GNSPs shown in (d), revealing a relatively constant width of ~500 nm for all GNSPs within the field of view. (g) SEM image of one GNSP isolated from the batch of GNSPs in (e) and placed on a silicon substrate, showing a length of ~66 μm (main panel) and a three-fold branching point near the end of the GNSP (inset). The GNSP in the main panel is highlighted by yellow dashed lines for clarity. (h) A representative histogram of the aspect ratios of GNSPs obtained from multiple sets of SEM images within their field of view. (i) A typical Raman spectrum of GNSPs.

The PECVD system is equipped with a residual gas analyzer (RGA) and an optical emission spectrometer (OES), which are used to monitor the gases in the growth chamber during the PECVD process. Two representative RGA spectra are shown in **Figure 2.2b** and **2.2c**, where the shaded band indicates the time interval from turning on to turning off the plasma. The spectrum in **Figure 2.2b** reveals that hydrogen chloride (HCl) is a main byproduct of the seeded PECVD growth process. This indicates that hydrogen radicals can react with chlorine in 1,2-DCB to form hydrogen chloride and render the resulting vertical GNSPS mostly free of chlorine. Additionally, substantial amounts of C_2 and C_6 radicals together with C_6H_6 molecules are found during the plasma growth process, as shown in **Figure 2.2c**. We note that while C_2 are common radicals found in all previously reported thermally assisted PECVD growth,[45] the eminent presence of C_6 radicals and C_6H_6 molecules are unique in our low-temperature PECVD process.

We have also monitored the optical emission spectra (OES) of the plasma during the growth process as a function of the 1,2-DCB/CH_4 partial pressure ratio, as shown in **Figure 2.3**. We find that the intensities of all hydrogen related peaks (H_α, H_2 and H_β) decrease with increasing 1,2-DCB partial pressure, consistent with the reaction of hydrogen with increasing chlorine radicals. On the other hand, the intensity of C_2 radicals is enhanced upon the introduction of 1,2-DCB precursor molecules, although no further increase appears with increasing 1,2-DCB partial pressure.

Figure 2.2d and **2.2e** show two representative SEM images of the top view of GNSPs grown for 10 min with the growth parameters listed in the first row of **Table 2.1**, and **Figure 2.2f** is the SEM image of a tilted view (at 52°) of the GNSPs shown in **Figure 2.2d**. We note that the widths of all GNSPs synthesized with a given set of PECVD growth

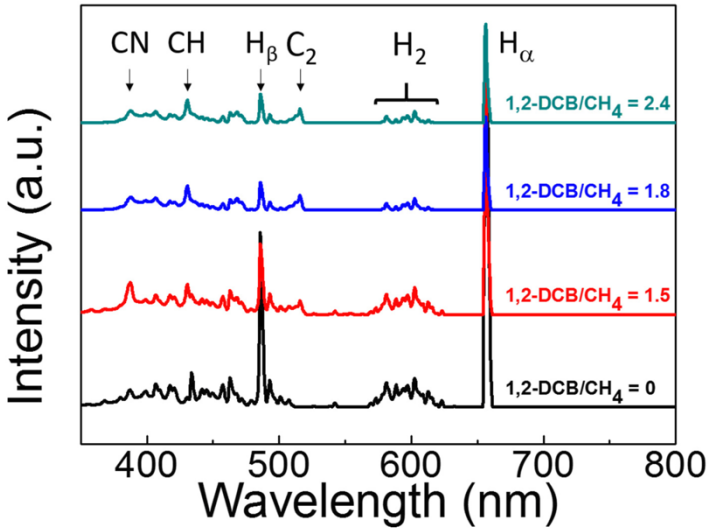

CN = 388 nm, CH = 431 nm, H_β = 486 nm, C_2=516 nm, H_α = 656 nm

Figure 2.3: OES of plasma for GNSPs growth under different 1,2-DCB/CH_4 partial pressure ratios, showing decreasing intensities of all hydrogen related peaks with increasing 1,2-DCB partial pressure. On the other hand, the intensity of C_2 radicals, critically important for graphene growth, is enhanced upon introduction of 1,2-DCB precursor molecules, although no further increase appears with increasing 1,2-DCB partial pressure.

parameters appeared to be nearly the same, as exemplified by the tilted view shown in **Figure 2.2f** where the average width of GNSPs is ~500 nm. On the other hand, there is a range of length distributions for the GNSPs, and they are typically on the order of tens of micrometers, as exemplified by the yellow line in **Figure 2.2d** from one open end to the other open end, and by the SEM image shown in **Figure 2.2g** for an isolated GNSP that was transferred to a silicon substrate. Here we note that the real lengths of individual GNSPs are generally much longer than the distances between joint points revealed in the SEM images of as-grown GNSPs, as corroborated by **Figure 2.2g**.

To isolate and image individual GNSPs by SEM, we first immersed the copper substrate with as-grown GNSPs in N-methyl pyrrolidone (NMP) solvent for ~ 9 h and

Table 2.1: Experimental parameters for the growth process, showing the gas partial pressures of 1,2-DCB and CH_4, plasma power, and time for the PECVD growth of GNSPs. The gas partial pressures were as measured in the RGA.

1,2-DCB (nTorr)	CH_4 (nTorr)	Power (W)	Growth time (min)	Yield (μg)
1 ~ 10	10 ~ 40	40	10	≤ 1
1 ~ 10	10 ~ 40	60	10	12 ± 6
1 ~ 10	900	60	5	350 ± 280
1 ~ 10	900	60	10	530 ± 130
1 ~ 10	900	60	15	800 ± 270
1 ~ 10	900	60	20	1300 ± 430

then sonicated the solution for 3 min. A drop of the solution with dispersed GNSPs was placed on a silicon substrate and then heated at 175 °C until the solvent completely boiled off. GNSPs left on the silicon substrate were then imaged by SEM without further modification.

By analyzing the top views of multiple sets of SEM images for the length distributions of GNSPs and the tilted views for the average widths, we obtained a representative histogram for the aspect ratios of GNSPs in **Figure 2.2h**, showing a distribution from 10 ~ 130.

A representative Raman spectrum of the GNSPs is shown in **Figure 2.2i**, where three distinct peaks are visible:[88–91] The peak at ~ 2700 cm^{-1} is known as the *2D*-band that represents a double-resonance process of graphene; the peak at ~1590 cm^{-1} is the *G*-band associated with the doubly degenerate zone-center E_{2g} mode of graphene, and the peak at ~1350 cm^{-1} is the *D*-band that corresponds to zone-boundary phonons due to defects,

edges, and/or folds of graphene sheets.[88–91] Given that the laser spot of our Raman spectrometer (~ 1 μm) is larger than the typical widths (tens to hundreds of nanometers) of our GNSPs, we attribute the intense *D*-band of our GNSPs to the prevailing presence of edges and/or the presence of folds as observed in SEM and transmission electron microscopy (TEM) images. We further note that the *2D*-to-*G* intensity ratio, (I_{2D}/I_G), is typically greater than 1 and that the full-width-half-maximum (FWHM) of the *2D*-band is relatively sharp, which seems to suggest that our GNSPs are largely monolayer.[88–92] However, this notion contradicts the findings of multilayer GNSPs from our AFM and TEM studies. These seemingly inconsistent results can be reconciled by the presence of incommensurate rotation of one layer relative the adjacent layers of these multilayer GNSPs, as elaborated later in this manuscript. Moreover, the turbostratic multilayer structures of GNSPs may also be responsible for the appearance of a slight shoulder in the *G*-band peak, which is known as the *D′*-band that results from defects-induced intra-valley scattering.[88,89]

To investigate the dependence of GNSPs growth on various parameters, we show in **Figure 2.4a ~ 2.4c** SEM top view images of PECVD-grown GNSPs on Cu under different 1,2-DCB/CH_4 partial pressure ratios. The total gas pressure was 500 mTorr and the flow rate of H_2 was 2 sccm. With the CH_4 partial pressure kept constant at ~6×10^{-9} Torr during the growth, we found that the morphology of GNSPs was strongly dependent on the ratio of 1,2-DCB to CH_4 partial pressures. For instance, when the 1,2-DCB/CH_4 partial pressure ratio was ~1.5 or less, the resulting GNSPs grown on Cu had typical lengths of a few to tens of micrometers and relatively large aspect ratios, as exemplified in **Figure 2.4a**. With the partial pressure ratio of 1,2-DCB/CH_4 increased to ~1.8, the GNSPs began to

branch out, as shown in **Figure 2.4b**. Upon further increase of the 1,2-DCB/CH_4 partial pressure ratio to ~2.4, a highly branched, flower-like nanostructure developed. These graphene "nano-flowers" (see **Figure 2.4c**) were thinner and shorter than the typical GNSPs grown with a smaller 1,2-DCB/CH_4 partial pressure ratio. This trend was in part attributed to the high 1,2-DCB concentration that saturated the substrate and led to a high density of nucleation sites and therefore an overall decrease in the lateral size of GNSPs, as manifested in **Figure 2.4c**. The branching behavior in addition to the shorter lengths of the graphene nanostructures may be attributed to the large amount of 1,2-DCB that resulted in excess chlorine ions terminated along the edges of the GNSPs and activated the formation of the branching behavior. This scenario is consistent with studies of the ultraviolet photoelectron spectroscopy (UPS), TEM and energy-dispersive x-ray spectroscopy (EDS) of GNSPs as a function of the 1,2-DCB/CH_4 partial pressure ratio, to be elaborated below.

UPS experiments were conducted to investigate the work functions of GNSPs grown under different 1,2-DCB/CH_4 partial pressure ratios and to provide direct information about possible doping effects on GNSPs.[93–95] As shown in **Figure 2.4d** and summarized in **Figure 2.4g**, the work function value (Φ) deduced from the secondary electron cutoff of the UPS spectrum was found to be 4.45 eV for GNSPs grown with a 1,2-DCB/CH_4 partial pressure ratio = 1.5, which is a value close to that of pristine graphene (~ 4.5 eV).[96] The work function value decreased to 4.16 eV for GNSPs grown with a 1,2-

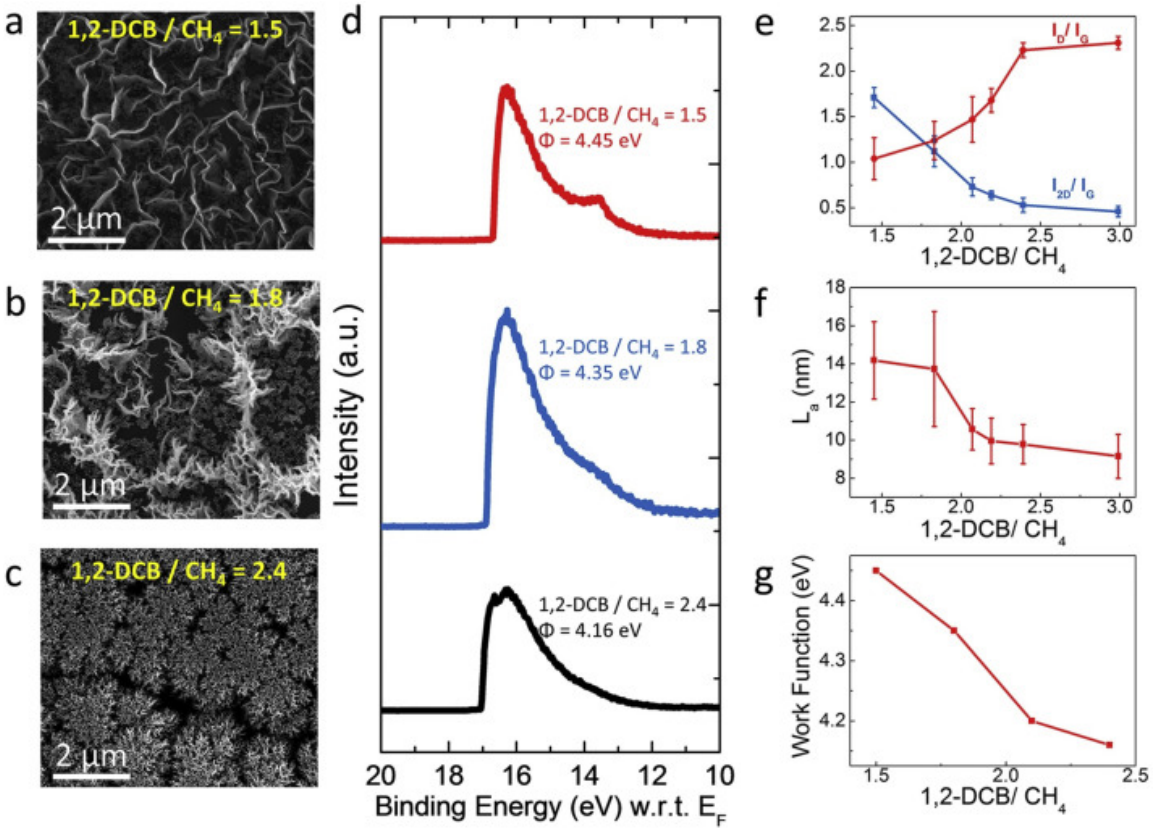

Figure 2.4: Dependence of the surface morphology, work function, Raman spectroscopy and crystalline size of GNSPs on the 1,2-DCB/CH_4 partial pressure ratio: (a)-(c) SEM images of GNSPs with 1,2-DCB/CH_4 partial pressure ratio=1.5 in (a), 1.8 in (b) and 2.4 in (c), showing increasing branching phenomena. (d) UPS data taken on GNSPs grown under 1,2-DCB/CH_4 partial pressure ratio = 1.5, 1.8 and 2.4, showing increasing electron doping. (e) Raman 2D/G and D/G intensity ratios of GNSPs grown under different 1,2-DCB/CH_4 partial pressure ratios. (f) planar sp^2 crystallite size (L_a) and (g) work function of our GNSPs as a function of the 1,2-DCB/CH_4 partial pressure ratio.

DCB/CH_4 partial pressure ratio increased to 2.4, implying significant electron doping. This finding suggests that excess 1,2-DCB not only resulted in the formation of branches and excess chlorine in the GNSPs (see TEM and EDS results) but also introduced additional electron doping.

We further performed Raman spectroscopic studies on GNSPs grown under different 1,2-DCB/CH_4 partial pressure ratios. **Figure 2.4e** shows the *2D* to *G* intensity ratios, (I_{2D}/I_G), and *D* to *G* intensity ratios, (I_D/I_G), of GNSPs grown at different 1,2-DCB/CH_4 partial pressure ratios. The (I_{2D}/I_G) ratio decreases with the increase of 1,2-DCB/CH_4 partial pressure ratio, suggesting that more layers of GNSPs were grown[88,89] with larger amounts of 1,2-DCB. On the other hand, the (I_D/I_G) ratio increases with the increase of 1,2-DCB/CH_4 partial pressure ratio, which is consistent with more edges[88,89] due to branching. Additionally, the in-plane sp^2 crystallite size (L_a) of the GNSPs may be estimated by using the (I_D/I_G) ratio and the following empirical formula.[97]

$$L_a\ (\text{nm}) = \frac{560}{E_L^4}\left(\frac{I_D}{I_G}\right)^{-1}$$

where E_L denotes the excitation energy of the laser source, which is 514 nm for our Raman spectrometer. We find that both the crystallite size L_a and the work function Φ of the GNSPs decrease steadily with increasing 1,2-DCB/CH_4 partial pressure ratio, as illustrated in **Figure 2.4f** and **2.4g**, respectively.

In order to achieve high yields of GNSPs growth, we experimented various parameters for synthesizing typical GNSPs with 1,2-DCB/CH_4 partial pressure ratios <~ 1, as summarized in **Table 2.1**. We found that the yield of GNSPs, determined in units of

mass per unit area, increased by more than one order of magnitude when the power was increased from 40 W to 60 W. This finding may be attributed to the presence of more energetic gas molecules and radicals (particularly C_2, C_6 and C_6H_6) in the plasma to initiate and maintain the growth of GNSPs. Additionally, higher CH_4 partial pressure and longer growth time provided more carbon sources and therefore also help increase the yield of GNSPs. On the other hand, further increase of either the plasma power above 60 W or the CH_4 partial pressure could not result in higher yields, which may be the result of a limited surface area of the Cu substrate in our growth chamber for initiating the vertical growth of GNSPs. Moreover, excess plasma power tends to increase the amount of C_2 radicals at the expense of reducing the amount of C_6 radicals and C_6H_6 molecules. Given that C_6 radicals and C_6H_6 molecules are likely playing an important role in enhancing the growth rate of GNSPs, proper balance between the plasma power and the amount of C_6 and C_6H_6 is necessary to achieve high yields of GNSPs.

By optimizing various growth parameters, we found that the best yield for 20 min of growth time could reach (1.30 ± 0.43) mg/cm2, or equivalently, (13.0 ± 4.3) g/m2. The high-yield growth of GNSPs resulted in a completely darkened surface of the substrate due to dense coverage of GNSPs on the metallic substrate, as exemplified by the optical micrographs in **Figure 2.5a** and **2.5b** and the nearly zero optical transmission from 400 nm to 800 nm shown in the main panel of **Figure 2.5**. The completely darkened substrate surface by the coverage of GNSPs and the vanishing optical transmission is indicative of strong light absorption by GNSPs, which may be attributed to effective light trapping in stacks of GNSPs due to multiple subwavelenth scattering. Thus, GNSPs may be considered

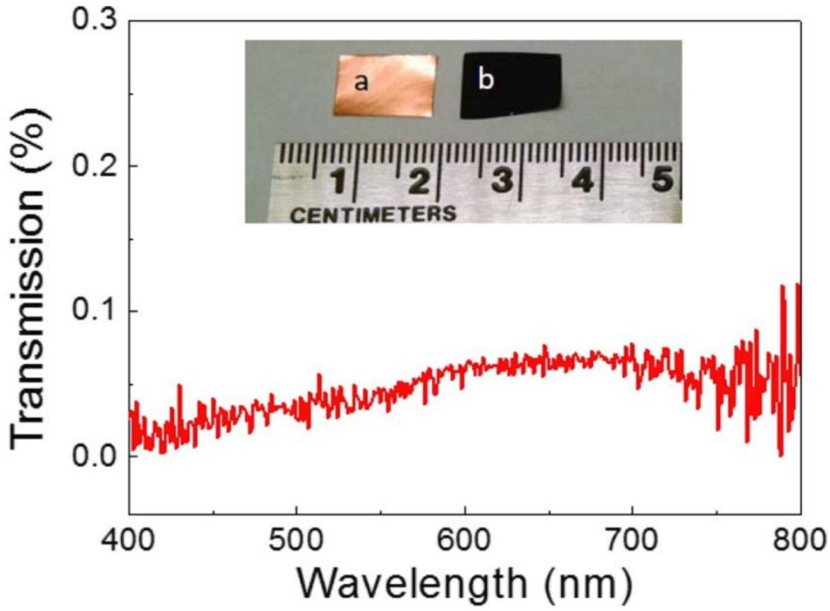

Figure 2.5: Evidences of strong optical absorption by GNSPs: The main panel shows the optical transmission spectrum of GNSPs for wavelengths from 400 nm to 800 nm, revealing transmission <0.1% for the entire range of wavelengths. The inset shows micrographs of a copper substrate (a) before and (b) after the growth of GNSPs. The growth parameters for the micrograph in (b) are given in the last row of Table 1. Here we note that the transmission spectrum was obtained by using a Cary 5000 absorption spectrometer with an integrating sphere , and the GNSPs were transferred from the Cu substrate onto a quartz substreate for the optical measurement. The incident light was sent through the entire GNSPs sheet and the underlying quartz substrate and then was collected by a detector. The baseline signal of the spectrum was obtained by subtracting the transmission signals from a blank quartz substrate as the reference.

as efficient light absorbers for potential applications to photovoltaic cells when combined with proper plasmonic nanostructures.[69]

Next, nanoscale structural properties and chemical compositions of the PECVD-grown GNSPs were investigated by means of TEM and EDS. Measurements were initially performed on standard GNSPs similar to those shown in **Figure 2.4a**. **Figure 2.6a** ~ **2.6c** are TEM top view images, with successively increasing resolution, of GNSPs grown with a 1,2-DCB/CH_4 partial pressure ratio ~ 1.5. From detailed TEM studies, we found that the typical size of GNSPs transferred to the TEM grid was 500 nm ~ 1.0 μm in width and 5 ~ 10 μm in length, as exemplified in **Figure 2.6a**. The shorter lengths than those of the as-grown GNSPs (as represented by the histogram in **Figure 2.4h** may be attributed to the TEM sample preparation steps that involved sonication of GNSPs in solution that led to shortened samples.

These GNSPs were generally flat over large areas and exhibited ordered nanoscale structures, as illustrated in **Figure 2.6b**. High resolution images taken on these flat areas further revealed graphene atomic lattice structures, as shown in **Figure 2.6c**. We found that these GNSPs were mostly multilayers and turbostratic: From selected area diffraction (SAD) in **Figure 2.6d**, the sample exhibited two predominant orientations and exceeded 6 layers in thickness. This finding of multilayer GNSPs seems to differ from Raman spectroscopic studies of the same GNSPs that always revealed both (I_{2D}/I_G) ratios >1 and relatively small FWHM in the *2D*-band and so would seem to imply monolayer

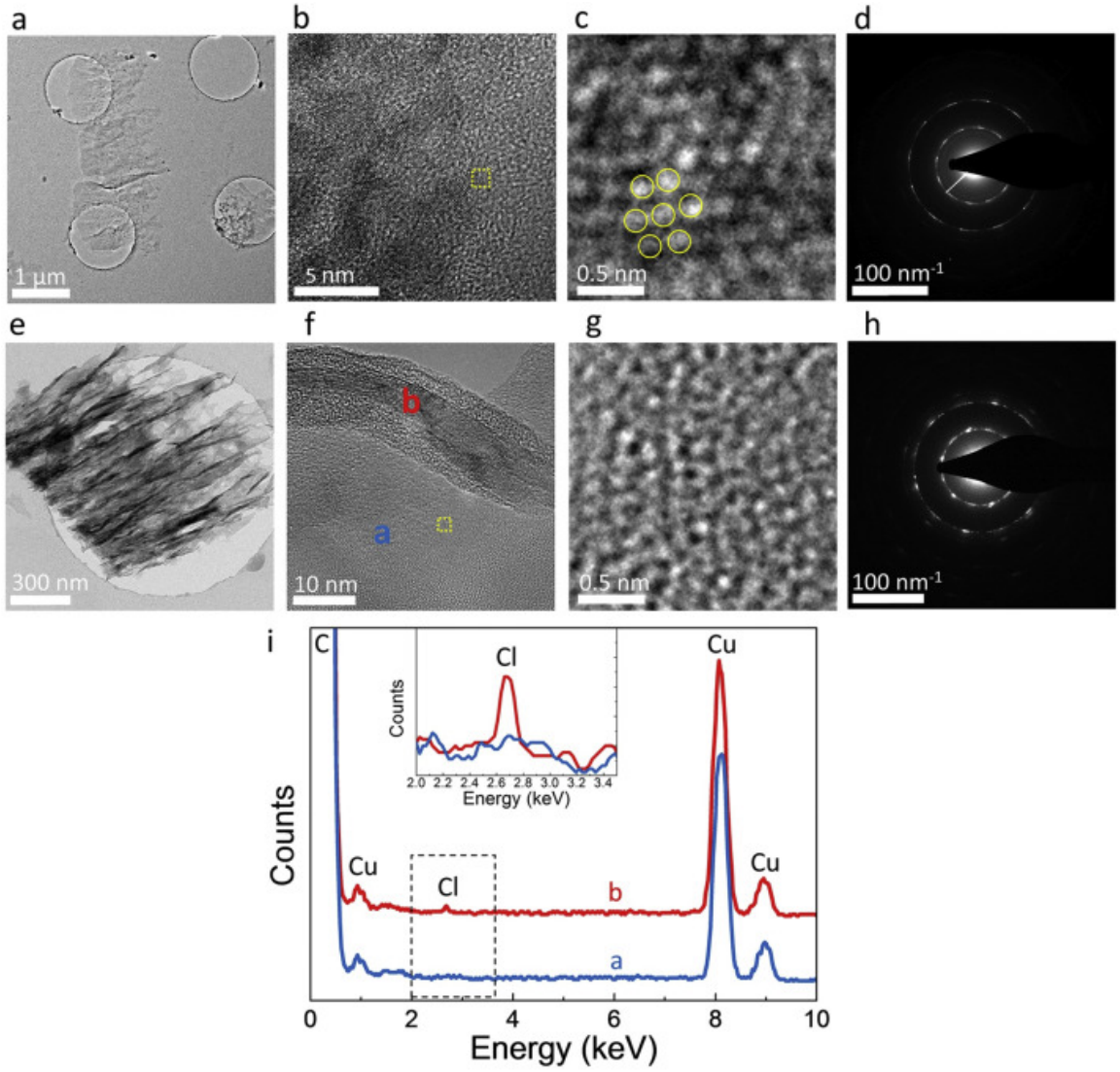

Figure 2.6: (a)-(c) TEM top view images of GNSPs with increasing resolution from large scale to atomic scale images, with (c) being the expansion of a region indicated by the small yellow box in (b). (d) SAD patterns of GNSPs for the region shown in (c). (e)-(f) TEM top view images of graphene nanoflowers from large scale to atomic scale images, with (g) being the expansion of a region indicated by the small yellow box in (f). (h) SAD pattern of the sample region shown in (g). (i) EDS data shows a distinct chlorine peak on a branching region labeled by *b* in (f), which is in stark contrast to the absence of chlorine in flat areas such as the region labeled by *a*. The inset is an expansion of the dashed area shown in the main panel.

GNSPs.[86,88,91] However, we note that the Raman spectra of multilayer graphene sheets with turbostratic stacking (where individual layers separated by a larger than normal interlayer distance) were also found to exhibit (I_{2D}/I_G) ratios > 1.[98] Therefore, our findings derived

from the TEM studies of standard GNSPs can be reconciled with the Raman spectroscopic studies.

In addition to studies of the structural properties, we performed nanoscale EDS measurements on flat, unstrained regions of these standard GNSPs, and found a pure carbon composition without any chlorine or other contaminates. This finding is in contrast to studies of the "nano-flowers" samples where chlorine appeared in regions with bifurcations, branching or strain, as explained below.

In **Figure 2.6e** ~ **2.6g**, we show TEM images with successively increasing resolution that were taken on nano-flower GNSPs grown with a 1,2-DCB/CH_4 partial pressure ratio ~ 2.3. In contrast to the typical images taken on standard GNSPs, **Figure 2.6e** and **2.6f** reveal that nano-flowers generally consisted of a large number of layers, with numerous branching points and reorientations of the layers. In particular, **Figure 2.6f** shows that in the reoriented graphene region the number of graphene layers within the field of view is > 20, whereas graphene atomic structures can be resolved in flat regions, as exemplified in **Figure 2.6g**. Further SAD studies on a flat region of the sample in **Figure 2.6f** exhibit a diffraction pattern that provides evidence for multiple layers, with varying orientations for many individual graphene layers that lead to the disordered circular pattern. On the other hand, a significant chlorine peak in the EDS data is always observed at a large number of branching and reorientation locations in the nano-flower samples, as exemplified in **Figure 2.6i**. This presence of a distinct chorine peak in a branching region of the nano-flowers is in stark contrast to the absence of any chlorine signal in the flat region of the same samples.

We also investigated the electrical properties of the standard GNSPs by aligning them on Au electrodes using the dielectrophoresis techniques.[99,100] We found that the sheet resistance R of a single layer GNSPs to be ranging from ~ 7.0 kΩ/□ to ~ 7.8 kΩ/□ at room temperature, which were larger than that of typical pristine graphene sheet resistance (~ 1 kΩ/□), but were significantly smaller than those values (~ 50 kΩ/□ to ~ 30 kΩ/□) reported for lithographically patterned single-layer GNSPS of comparable widths (100 nm ~ 1 μm),[101] suggesting good conducting properties of our GNSPS even in the absence of excess doping. If we take the work function of undoped graphene to be 4.50 eV,[95] the electron density n_{2D} of our standard GNSPs with $\Phi = 4.45$ eV (and therefore a Fermi energy $E_F \sim 0.05$ eV above the Dirac point) is estimated to be $n_{2D} = \left(\frac{E_F}{\hbar v_F}\right)^2 / \pi \approx 1.0\times10^{11}$ cm^{-2} for a Fermi velocity $v_F = 10^6$ m/s.[25] Therefore, the electrical mobility μ of our GNSPs is found to be $\mu = (n_{2D} e R) = 8000 \sim 9000$ cm^2/V-s at room temperature, which is 5 ~ 10 times smaller than that of our typical PECVD-grown graphene sheets[86] and is about $10^2 \sim 10^3$ times better than that of the vertical graphene nano-sheets reported to date.[85,100]

Post publication experimental results

When initially attempting to grow GNSPs, the first three precursors we tried using were 1,2-dichlorobenzene (1,2-DCB), 1,2-dibromobenzene (1,2-DBB), and 1,2-dibromonapthalene (1,8-DBN). Each of these precursors resulted in effective growth of GNSPs, although 1,2-DBB and 1,8-DBN produced GNSPs in lower yield, which we attribute to the lower vapor pressures of 1,2-DBB and 1,2-DBN causing their low concentration during growth.

Initially, we conjectured these SBPs resulted in growth of GNSPs due to the substituents' electronegativity causing a dipole moment and inducing reactivity. To test this conjecture, we attempted growing GNSPs with phenol and toluene which have strong and weak dipole moments of 0.719 D and 0.293 D, respectively.[102] Contrary to our conjecture, however, using phenol did not result in growth of GNSPs while using toluene resulted in a low yield growth of GNSPs. This clearly indicates that electronegativity and dipole moment were not the critical factors that enabled growth of GNSPs.

Next, we investigated whether the bond dissociation energy between the benzene ring carbon atom and its substituent affected growth of GNSPs. The bond dissociation energies of various SBPs (shown in **Figure 2.7**) and whether they resulted in growth of GNSPs is shown in **Table 2.2**. As mentioned previously, including phenol (BDE = 4.8 eV) did not result in growth, and including toluene (BDE = 4.4 eV) resulted in limited growth, while inclusion of any SBP with a BDE less than or equal to 4.0 eV did result in growth of GNSPs. Further, the input microwave power of each growth is indicated in **Table 2.1**,

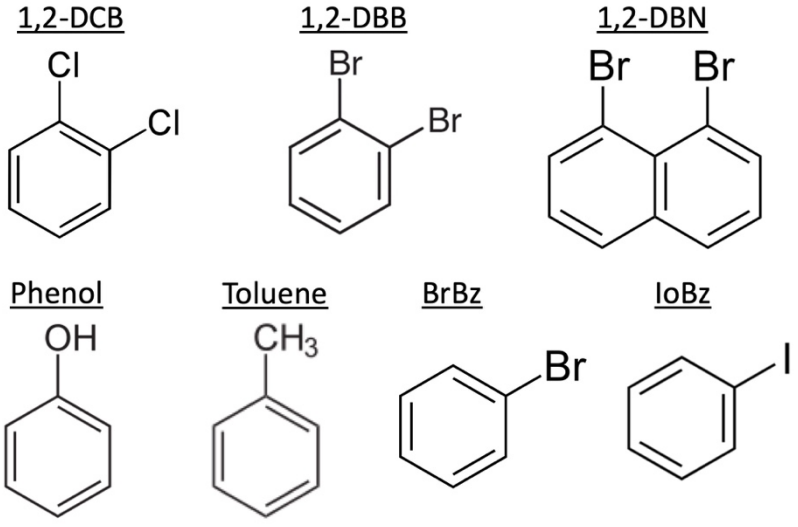

Figure 2.7: Substituted benzene and substituted naphthalene precursors used for synthesis of GNSPs and their abbreviations.

Table 2.2: Bond dissociation energies between aromatic ring and substituent of several SBPs and whether their inclusion resulted in growth at the indicated input microwave power.

Molecule	C-X bond dissociation energy (eV)[103]	GNSPs Deposition?
Phenol	4.8	No
Toluene	4.4	Yes, low yield @ 40 W
1,2-DCB	4.0	Yes, @ 40 W
1,2-DBB	~ 3.5*	Yes, low yield† @ 40 W
1,8-DBN	~ 3.5*	Yes, low yield† @ 40 W
BrBz	3.5	Yes, @ 30 W
IoBz	2.8	Yes, @ 20 W

*Data unavailable, but estimated to be similar to bromobenzene.
†Low yield was likely caused by low concentration of precursor due to low vapor pressure.

showing that inclusion of SBPs with lower BDEs enables growth at lower input microwave powers. For example, while using 1,2-DCB (BDE = 4.0 eV) as the SBP requires 40 W of input microwave power for GNSPs deposition, using IoBz (BDE = 2.8 eV) as the SBP only requires 20 W of input microwave power.

The correlation between SBP and required input microwave power is understood by considering that the input microwave power critically affects the plasma composition, total number of radicals, temperature and particle velocity.[104] Increasing the input microwave power increases the tendency to break chemical bonds (in any molecule) in the plasma, as increased microwave power creates more radicals, higher temperature, and more collisions. However, weaker bonds do not require as high of temperature and collision

energy to break. Therefore, SBPs with lower bond dissociation energies require less input microwave power to form benzene radicals and seed the growth of GNSPs.

Discussion

Based on the aforementioned experimental results, we discuss below likely mechanisms for growth of GNSPs. First, we consider the growth mechanism of VOG materials which use, for example, hydrogen, methane, a microwave induced plasma at low pressure and a heated substrate. In this growth configuration a likely mechanism (though the mechanism is still debated) is that methane forms radicals in the plasma which then form a thin layer of either graphitic or amorphous carbon on the substrate. Grain boundaries and/or defects in the thin carbon layer are then seeding locations for vertical graphene sheets. Carbon radicals then contribute to propagation of the graphene growth and hydrogen radicals remove defects.[45] Growth in our system is likely similar, except that SBPs play some role that negates the need for a heated substrate.

Considering that the BDE of the SBPs critically affects the required input microwave power in order to enable deposition of GNSPs (**Table 2.1**), dissociation of the SBP substituent bond appears to be a kinetic barrier for GNSPs deposition that is overcome by increasing microwave input power or using SBPs with lower BDEs. Accordingly, we suggest that, initially, the SBP substituent bond is broken. This could occur by either impact dissociation or radical reaction dissociation. However, the elevated HCl levels in the RGA during growth (see **Figure 2.4b**) suggest that the chlorine atoms on 1,2-DCB react with hydrogen radicals in order to leave 1,2-DCB, *i.e.*, the SBP bond is broken by radical reaction dissociation with hydrogen.

After the SBP substituent bond is broken, reactive benzene radicals initiate growth of GNSPs. Then, similar to conventional growth schemes, methane radicals propagate growth and hydrogen radicals etch defects, and benzene radicals continue to propagate growth. One may be concerned that some SBPs involve two substituents (*e.g.*, 1,2-DCB) while others involve one (*e.g.*, IoBz). However, the BDE of the C-H bond in a phenyl radical (*i.e.*, C_6H_5) is 3.4 eV,[103] which is weaker than the BDE of many of the SBP substituent bonds, indicating that whether the SBP has one or two substituents is not important.

Regarding the morphological differences between GNSPs and graphene nanoflowers, we propose that these differences are simply due to growth rate. For example, in the graphene nanoflowers, the flowering phenomenon and the excess chlorine may be due to excess growth rate, which results in excess defects as the growth rate far exceeds the etching rate. Defects sites may serve as seeding sites for new graphene nanowalls,[45] leading to excess branching and the flowering phenomenon. Additionally, the lack of etching may enable chlorine defects to maintain in the structure. On the other hand, GNSPs result from a balance between growth and etching such that long sheets of high quality graphene are obtained.

All in all, our empirical findings are suggestive of the importance of both 1,2-DCB precursor molecules and the resulting C_6, C_6H_6 and chlorine radicals in hydrogen plasma for mediating rapid vertical growth of GNSPs with large aspect ratios. In contrast to other reports for PECVD-grown vertical graphene sheets to date that generally required

pretreatment of the substrates and additional substrate heating from 500 °C to 1000 °C,[45,85] our single-step, low-power growth process requires neither active heating nor pretreatment of the substrates, indicating the effectiveness of 1,2-DCB as seeding molecules for the vertical growth of GNSPs.

Conclusions

In summary, we have developed a new high-yield single-step method for growing large quantity GNSPs on various transition-metal substrates by means of PECVD and aromatic precursors such as 1,2-DCB molecules. This efficient growth method does not require any active heating and can reproducibly produce a high yield of ~10 g/m^2 within 20 min at a relative low power of ≤ 60 W. Moreover, the GNSPs thus produced reveal large aspect ratios (up to >~ 130) and can be easily transferred from the growth substrate to any other substrates. Therefore, this new growth method is highly promising for mass production of GNSPs. From studies of the Raman spectra, SEM images, UPS, TEM images, EDS, and electrical conductivity of these GNSPs as functions of the growth parameters, we have also confirmed the high-quality of these GNSPs and found the correlation of the properties of GNSPs with the growth parameters. Based on our experimental findings, we propose a growth and branching mechanism of GNSPs that suggests the important role of the 1,2-DCB precursor molecules in assisting the vertical growth and determining the morphology as well as the large aspect ratio of GNSPs. These findings therefore open up a new pathway to large-scale, inexpensive mass production of high-quality GNSPs for such large-scale applications as supercapacitors and photovoltaic cells.

2.1.2 Generation I growth system description and performance

A schematic of the generation I system is provided in **Figure 2.8**. This system is functionally similar to generation 0. That is, deposition takes place in a ½" outer diameter glass chamber fitted with an Evenson cavity. The key difference in this chamber is that, in an effort to increase the yield of GNSPs, the system splits into eight separate gas lines and has eight chambers and cavities where GNSPs growth can take place. Downstream of the deposition chambers, the lines converge back to a single line. Similar to the previous system, hydrogen and methane gases are injected into the system from high pressure gas cylinders with the flow rate controlled by MFCs, and this system is equipped with two pressure gauges (PG), an RGA, a cold trap (CT), a regulator valve (RV), and a mechanical roughing pump.

There are major differences between this system and generation 0, however. Two vacuum sealed vials can contain multiple precursors (P1 and P2). P1 is connected to the mainline via two manual leak valves (LV2 and LV3), and there is a third manual leak valve

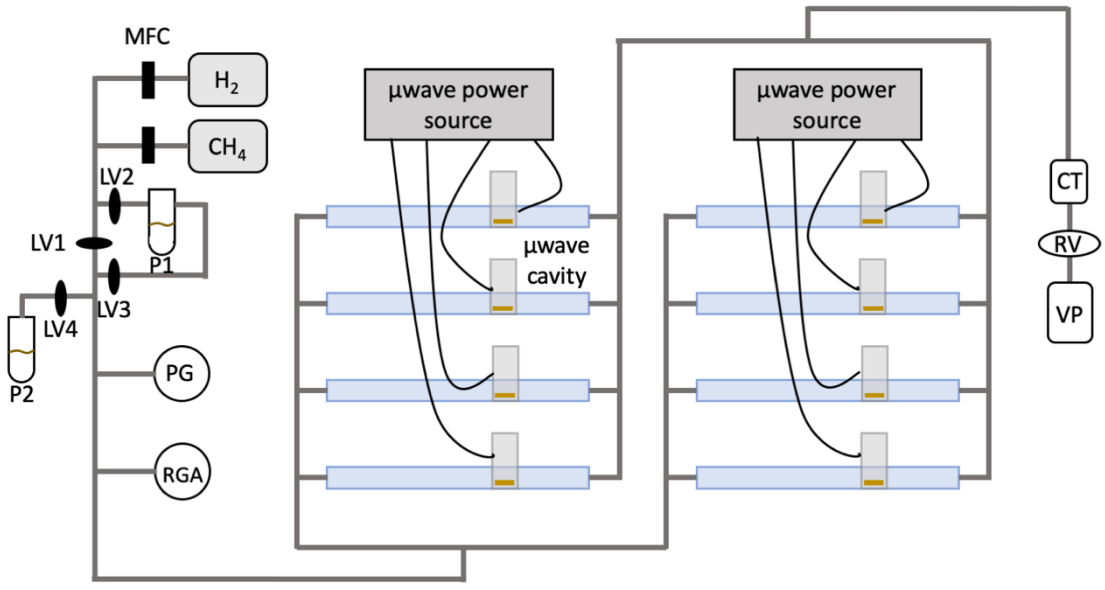

Figure 2.8: Schematic of generation I GNSPs deposition system.

between the points where LV2 and LV3 connect to the main line. The reason for this is that with the gas line splitting into eight separate chambers, the hydrogen and methane gas flowrates are much higher for this system than the previous system, and the evaporation rate of the SBPs becomes insufficient with respect to the higher hydrogen and methane gas flowrates, even with the leak valve completely opened. To remedy this, we include a larger vacuum sealed vial (6" diameter) and included a gas line that passes directly through it. When the gases pass directly through the vial, they efficiently remove evaporated SBPs and induce further evaporation. By adjusting the relative fraction that LV1, LV2, and LV3 are open, we can accurately control the concentration of SBPs in the deposition chambers over a large range of concentrations. Additionally, the second vial (P2) included in this system can hold a second precursor that is delivered into the system via leak valve (LV4). As this vial does not have a gas line pass directly through it, P2 precursors must have a relatively high vapor pressure.

Another difference is that the pressure gauges and RGA are placed upstream of the deposition chamber rather than downstream. This protects these instruments from corrosive gases produced during GNSPs deposition, which is a problem here as this system is bigger and thus produces more corrosive gases.

Similar to the previous system, the adjustable parameters in this system are MFC gas flow rates (2 ~ 100 sccm), the fraction that leak valves are open, input microwave radiation power (0 ~ 200 W) and the chamber pressure (the two pressures gauges have respective ranges of 0.01 ~ 10 Torr and 1 ~ 1000 Torr). A typical recipe for GNSP growth in this system is 5 sccm CH_4 flowrate, 48 sccm H_2 flowrate, 70 W of microwave power, chamber pressure of 3.8 Torr and adjusting the LV1, LV2, and LV3 such that the SBP

signal is ~ 10 times less than the CH_4 signal (as measured by the RGA). To achieve this ratio, LV1 is typically ~ 2/3 closed, and LV2 and LV3 are completely open.

The difference in CH_4 and H_2 flowrates in this system is not surprising (as it is a bigger system), but the change in chamber pressure, microwave power and RGA signal ratios may be surprising. The difference in chamber pressure is accounted for by considering that the pressure is measured before the chamber splits into 8 components. Therefore, the pressure in the deposition chamber is much lower than 3.8 Torr. In fact, we measured that if the pressure gauges were near the deposition chamber and used the same gas flowrates, the pressure was ~ 0.6 Torr. Regarding the higher microwave power, the reason we used 60 W of microwave power on generation 0 is because that microwave source was not stable at microwave powers over 60 W. However, this system involves a newer microwave source model and is stable up to > 150 W. Finally, the difference in RGA signal ratios is accounted for by considering that we used a different RGA model in this system which may have affected the fragmentation rate of each component, and the higher flowrates may have affected the diffusion of relative components to the RGA.

2.1.3 Generation II growth system description and performance

A schematic of the generation II system is provided in **Figure 2.9**. Functionally, this system dramatically differs from generations 0 and I. The deposition chamber is a 12.1 cm inner diameter stainless steel tube (rather than ½" glass tube), the microwave sources are microwave antennae (μWA) rather than cavities (*i.e.*, they emit microwave radiation, but do not have a resonating cavity) and multiple microwave sources emit radiation into a single chamber. The motivation for using this chamber configuration is *i*) the larger chamber size can accommodate larger growth substrates, *ii*) the microwave antennae do

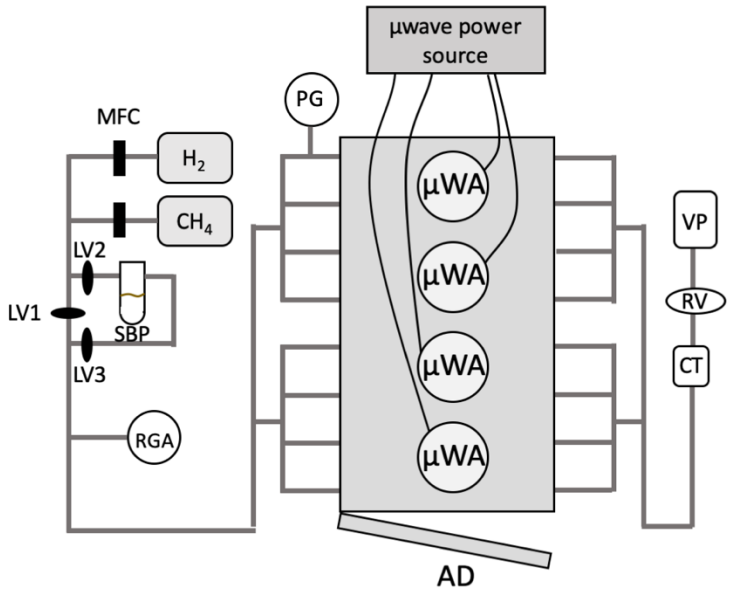

Figure 2.9: Schematic of generation II GNSPs deposition system.

not require a resonance condition and do not require tedious tuning, *iii*) the microwave antennae emit radiation in a diverging cone which increases the volume of the plasma and *iv*) loading/unloading samples into a single chamber is more efficient than using multiple chambers. In other words, this chamber was designed to increase yield and is a prototype for industrial scale growth system of GNSPs, as will be discussed in section *2.1.3*.

For the gas and SBP injection and RGA, this system is similar to generation I. Hydrogen and methane gases are stored in high pressure gas cylinders, and their flow into the system is controlled by MFCs. Injection of SBPs into the system is controlled by three manual leak valves (LV1, LV2, and LV3), similar to injection of P1 into the system for generation I. The RGA is also placed upstream of the deposition chamber.

The pressure gauges are placed after the splitting into eight gas lines for this system. This arrangement was not possible for generation I because it would have made one of the chambers inequivalent to the others and the deposition of GNSPs in each chamber may not

have been identical. In the case of generation II, the gas line arrangement in **Figure 9** becomes feasible because there is only one deposition chamber.

The gases flow into the deposition chamber through eight ports. A longitudinal schematic of the chamber is provided in **Figure 2.10a** and a cross sectional schematic is provided in **Figure 2.10b**. The gases flow into the chamber through eight inlet ports and out of the chamber through eight outlet ports. Four microwave antennae (image in **Figure**

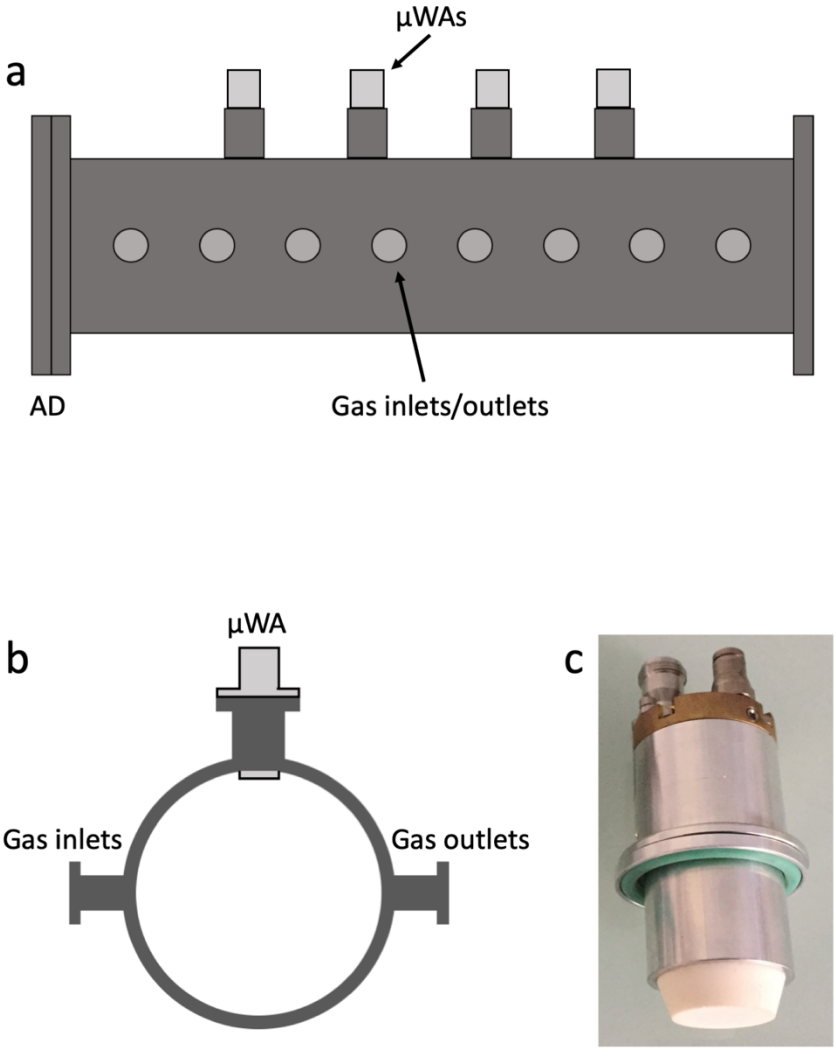

Figure 2.10: a) Longitudinal schematic of generation II chamber. b) Cross sectional schematic of generation II chamber. c) Image of a generation II microwave antenna for the generation II system.

2.10c) attach to the top of the chamber such that the radiation outlet is exposed in the chamber. A vacuum sealable access door (AD) with a glass viewing window is on one end of the chamber. After the gases leave the chamber they pass through a cold trap (CT), a regulator valve (RV) and reach the vacuum pump (VP).

The adjustable parameters in this system are MFC gas flow rates (2 ~ 100 sccm), the fraction that leak valves are open, input microwave radiation power (0 ~ 200 W) and the chamber pressure (the two pressures gauges have respective ranges of 0.01 ~ 10 Torr and 1 ~ 1000 Torr). A typical recipe for GNSP growth in this system is 40 sccm CH_4 flowrate, 0 sccm H_2 flowrate, 180 W of microwave power, chamber pressure of 200 mTorr and adjusting the LV1, LV2 and LV3 such that the SBP signal is ~ 100 times less than the CH_4 signal (as measured by the RGA). To achieve this ratio, LV1 and LV3 are typically fully open, and LV2 is completely closed. Additionally, the copper substrate must be placed ~ 1 cm from the microwave antennae.

The typical recipe for this system is very different from the typical recipes for generations 0 and I. This is in contrast to the very similar effective conditions in the deposition chambers of generations 0 and I despite their different input parameters. Before discussing the specific differences in the recipe for the generation II system, it is worth considering how the plasma is fundamentally different in this chamber. First, since the microwave source is not a resonant cavity, the microwave radiation is not as intense for a given input power. Second, since the chamber is much larger, the plasma is not bound to a small volume. This fundamentally alters the behavior of the plasma. For example, for the small glass chamber in generations 0 and I, radicals produced in the plasma could not as readily diffuse out of the plasma, whereas radicals readily diffuse away from the plasma in

the generation II chamber, which affects the concentrations of species in the plasma. Third, the growth substrate in generations 0 and I was in close physical contact with the ambient environment and therefore was cooled conductively by ambient air. The growth substrate in generation II, on the other hand, is shielded from ambient conditions very effectively by the stainless steel chamber. The temperature of the plasma in the generation 0 and I exceeded 425 °C.[86] Given that heat is an important factor in chemical reactions, so we expect this cooling discrepancy to play a role in the deposition.

Considering these fundamental differences in the plasma, we can understand why the recipe conditions are so different for the generation II system. First, this system requires a high CH_4 flowrate and no input of H_2. This difference may be understood by considering that CH_4 can provide hydrogen radicals to the plasma, and the difference in chamber geometry likely affected radicals such that H_2 is not necessary. Second, the input microwave power of 180 W is justified by considering that the antennae do not incorporate a resonance condition and do not concentrate the microwave radiation. Third, the lower chamber pressure is necessary because the lower pressure enables a larger and more intense plasma, which is necessary because of the lack of plasma confinement in this larger chamber. In fact, 200 mTorr was the lowest pressure achievable with the vacuum pump while injecting gases into the system, and even lower pressures may be preferred. The difference in RGA signal is justified similarly to what was discussed for the generation I RGA signal, *i.e.*, the difference in flowrates likely affects diffusion of species into the RGA chamber. Lastly, the placement of the copper growth substrate was critically important. It was found that placing it ~ 1 cm away from the antenna to be ideal, and placing it even 1 mm too far away from the antenna would result in no growth because the plasma was not

intense enough to yield enough reactive species, whereas placing it too close would result in defective growth, likely because the concentration of components in the plasma was not ideal.

Although the generation II system was successful in producing GNSPs over a larger area, it was problematic for the following reasons. First, the growth substrate had to be very close (~ 1 cm) to the microwave antenna. The cone-like emission of microwave radiation away from the microwave antenna therefore only resulted in growth over ~ 4 cm diameter circle on the growth substrate. This is a much larger growth area than the generations 0 and I systems, but still not sufficiently large for industrial applications. Second, microwave radiation was most intense at the surface of the antenna, which resulted in carbon deposition on the antenna. In principle, the deposit could be removed physically (*e.g.*, by scrapping it off with a steel brush) or by an oxygen plasma, converting the deposited carbon to CO_2, which would then be evacuated by the vacuum pump. Neither solution is desirable in an industrial environment however because each added step is costly to the fabrication procedure.

A schematic design shown in **Figure 2.11** is proposed to amend the aforementioned problems for generation II. Here, the microwave antenna is placed *outside* of the deposition chamber, transmitting the microwaves into the chamber via a glass window. In addition, a deposable glass slide will be placed flush with the window on the *inside* of the chamber. This would amend the first problem (a small deposition area) by allowing the microwave radiation (emitting in a cone shape) to spread to a larger area before enter the chamber where it is absorbed by the plasma and lessens in intensity. The window would also amend the second problem (carbon deposition on the antenna) because the antenna is not in the

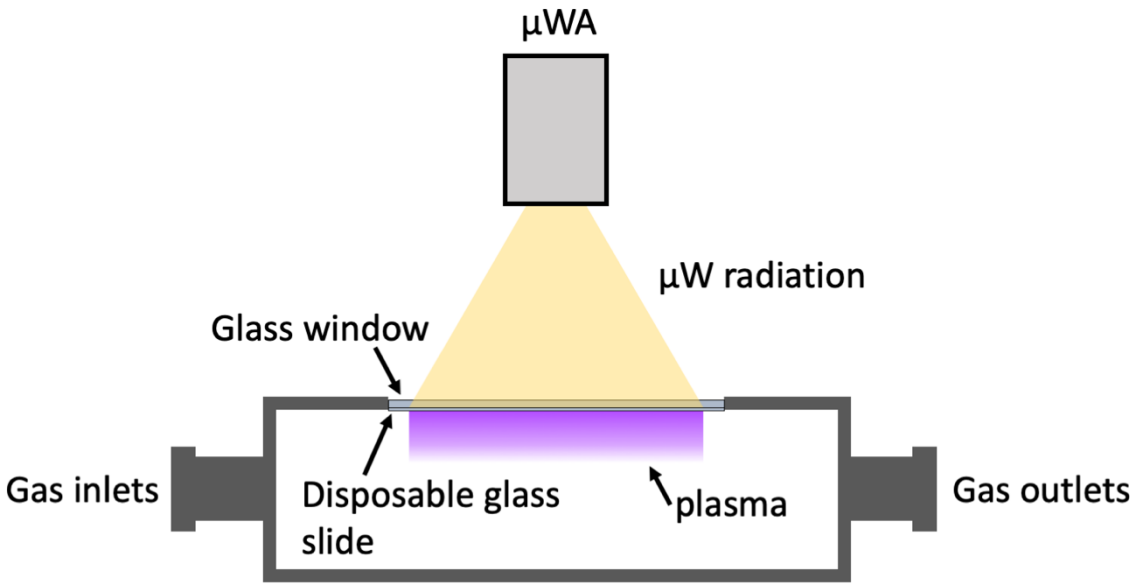

Figure 2.11: A schematic design to amend problems encountered in current generation II system.

chamber. Although this design introduces another problem, which is carbon deposition on the glass window, this problem can be amended by introducing the disposable glass slide which is flush with the glass window. In this configuration, the carbon deposition occurs on the disposable glass slide, and the glass window is preserved. By ensuring that the disposable glass slide is flush with the glass window, little (if any) plasma will be generated between the glass slide and the glass window, and even if there is some plasma generated there, the resulting carbon deposition will be minimal and can quickly be removed by a brief oxygen plasma. In addition, a lower chamber pressure may be effective in order to maintain a more intense plasma.

2.1.4 Perspectives on large scale production

The large scale production of GNSPs could be accomplished in a system similar to schematic in **Figure 2.11**, which has the following features that enable industrial scale production of GNSPs. I) Growth takes place over a large area. II) Multiple microwave

sources can simultaneously operate in a single chamber to grow GNSPs on multiple substrates. In addition, because microwave radiation is absorbed by the plasma, and microwave sources do not interact with each other, deposition chambers can be arbitrarily large and include an arbitrary amount of microwave sources. That is, a chamber can be very long and include many microwave sources that simultaneously grow GNSPs. This concept is shown schematically in **Figure 2.12a**. Also depicted in **Figure 2.12a** is that the large chamber will require multiple vacuum pumps in order to evacuate the large volume.

Two additional features must be added to the generation II system for industrial scale growth. First, a roll-to-roll configuration must be incorporated. Roll-to-roll configurations are widely used in industrial manufacturing, and the working principle is that, because flexible substrates can be rolled onto a cylinder, a flexible substrate can be

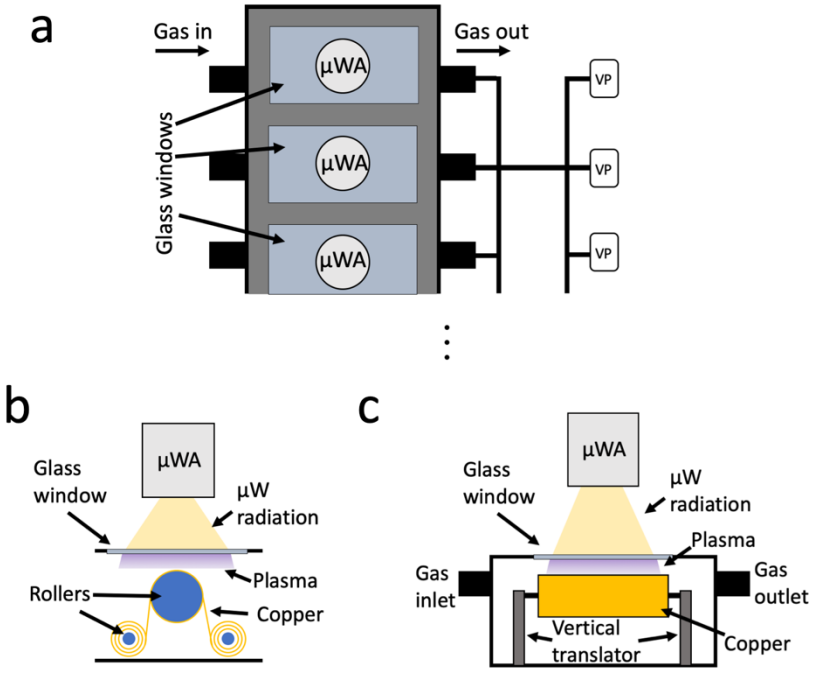

Figure 2.12: Proposed industrial scale fabrication system. a) Top-view schematic of arbitrarily large chamber with many sources and several vacuum pumps. b) Schematic of cross section perpendicular to gas flow demonstrating roll-to-roll configuration. c) Schematic of cross section parallel to gas flow showing height-variable roll-to-roll configuration.

unrolled from one cylinder and rolled onto another cylinder and pass beneath a deposition mechanism between the two cylinders.[105] This is shown schematically for this system in **Figure 2.12b**. Here, copper foil starts wrapped around one cylinder and is unwrapped while simultaneously being wrapped around the other cylinder. A third cylinder is included in this design to bring one section of the copper foil into the plasma while keeping the other sections farther away; this ensures the other parts are not exposed to reactive plasma species. The entire copper foil roll is then exposed to the deposition conditions, and so when the copper is removed a large area of GNSPs can be extracted from it.

As an alternative rolling mechanism, one may suggest a single cylinder plated with copper that is placed underneath the plasma source that is continuously turning, and while GNSPs grow on the top, GNSPs are extracted from the bottom by scrapping them off , which then exposes the copper for further growth when it returns to the top. This configuration would have the advantage of simplicity and recycling copper. Additionally, we have found that copper does not foul during GNSPs deposition, and we typically extract GNSPs from the copper by scrapping them off anyway. However, this alternative configuration has the detrimental feature that while scrapping off the GNSPs in the chamber, GNSPs dust will migrate to and compromise the vacuum pumps.

The second additional feature that must be incorporated for industrial scale growth is a translation stage controlling the height of the substrate during growth. This is necessary purely for practicality. When experimenting with the generation II system, we found that the copper substrate must be ~ 1 cm away from the plasma source, and if the substrate position differed by even 1 mm, the growth was severely impaired. Therefore, in order to

perfectly position each growth substrate, vertical translation stages are likely necessary for each deposition position. A schematic of this concept is shown in **Figure 2.12c**.

2.2 Heteroatom Doping Strategies

The synthesis and LIB application of The synthesis and lithium-ion battery (LIB) application of heteroatom doped graphene will be the subject of Chapters 4 and 5, wherein the novel syntheses of nitrogen-, silicon-, germanium-, and tin-doped graphene will be described. However, in order to present a cohesive and complete description of the synthesis strategies and instrumentation for the fabrication of GNSPs, we include here discussions of what heteroatom-doped graphene is, the principles for synthesizing heteroatom-doped graphene, and the instrumentation for fabricating heteroatom-doped graphene.

2.2.1 Heteroatom-doped graphene

The definition of heteroatom-doped graphene in this thesis and also in the published literature is that heteroatom-doped graphene is a graphene material with individual carbon atoms substituted by atoms of other elements. That is, the integrity of the graphene structure (*e.g.*, the honeycomb lattice) is largely maintained, but a fraction of the carbon atoms are replaced by other elements. Typical heteroatom dopants include nitrogen, boron, phosphorus, sulfur, *etc*.

This definition is distinct from either *graphene functionalization* or *nanoparticle anchoring*. In graphene functionalization, heteroatoms are present in the graphene material via covalent attachment to carbon atoms, but they are not substituted for the carbon atoms. Therefore, the bonding geometry among carbon atoms is largely maintained, but the

carbon-carbon bonds become sp^3 hybridized to accommodate an additional (sp^3) bond for the heteroatom. However, directly distinguishing between doped graphene and functionalized graphene is very difficult, and researchers occasionally term materials as "doped graphene" when the materials are actually functionalized graphene (as inferred by the heteroatom, which may not have a valence configuration amenable to doping). Typical heteroatoms for graphene functionalization include oxygen, chlorine, and fluoride.

In nanoparticle anchoring, on the other hand, nanoparticles are covalently attached to graphene. This is often termed in the literature as, for example, "silicon/graphene composite" or "Si@graphene," and is rarely mistermed as doped graphene because the nanoparticle constituents are easily distinguished by X-ray diffraction and/or Raman spectroscopy. Typical nanoparticles anchored to graphene include gold, platinum, SiO_2, Fe_3O_4, *etc.*, and the motivation for doing so is usually to simply use graphene as a high surface area scaffold for the nanoparticles.

2.2.2 Principles of heteroatom doping of GNSPs by PECVD

Two methods of doping graphene with heteroatoms via PECVD have been developed in this thesis: *i*) introducing heteroatom aromatic radicals (*e.g.*, see **Figure**

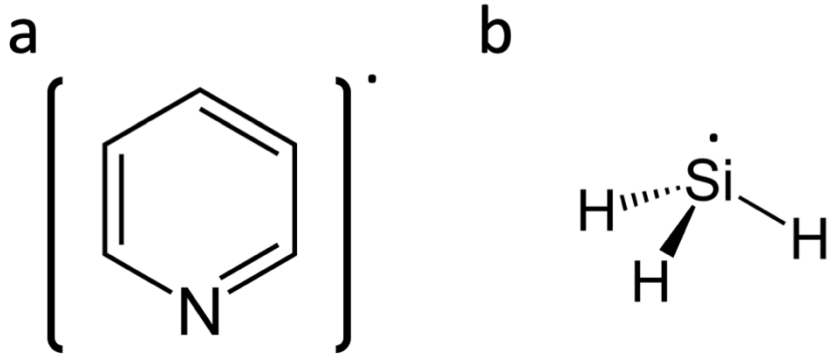

Figure 2.13: (a) Pyridine radical as an example heteroatom aromatic radical and (b) silane radical as an example heteroatom radical.

2.13a) into the plasma during GNSPs growth, and *ii*) introducing heteroatom radicals (*e.g.*, see Figure **2.13b**) into the plasma. The working principle here is quite simple: the heteroatom aromatic radical fills the role of benzene radicals and the heteroatom radical participates in similar chemistries as methane radicals. For example, pyridine radical can seed and propagate the growth of GNSPs, and nitrogen-doping in the pyridinic configuration is achieved (see Chapter 4).

Two practical requirements for fabrication of heteroatom-doped graphene via PECVD relate to the bond dissociation energy (BDE) and vapor pressure of the dopant precursor. Regarding bond dissociation energy, in order to generate the heteroatom (aromatic) radicals in the plasma, a precursor must be selected which has appropriate bond dissociation energies. For example, nitrogen-doped GNSPs can be obtained by injecting 3-chloropyridine instead of 1,2-DCB into the plasma. 3-chloropyridine has a C-Cl BDE equal to 3.9 eV, which is less than the C-Cl BDE for 1,2-DCB.[103] Although we have not explicitly performed the experiment, we expect that heteroatom precursors with a high BDE would not convert to radicals in high yield and the heteroatom would not dope the graphene.

The vapor pressure of the heteroatom precursor is the other practical consideration for heteroatom doping. This is simply because the vapor pressure of a compound dictates how easily it is controllably injected into the vacuum system. Because we conducted a detailed study on the 1,2-DCB-seeded growth of GNSPs, we referred to the vapor pressure of 1,2-DCB (~ 1.4 Torr at room temperature[106]) as a guide to selecting heteroatom dopant precursors. Additionally, gaseous precursors could also be used (*e.g.*, silane), which would require a high pressure gas cylinder and an MFC.

Using the aforementioned criteria, we have successfully used 3-chloropyridine, tetraethylsilane, tetraethyl germanium and tetraethyl tin to accomplish nitrogen-, silicon-, germanium-, and tin-doping of graphene.

2.2.3 Instrumentation

Heteroatom doping of GNSPs was accomplished in the generation I system by inserting the selected precursor in P2 in **Figure 2.8** and controlling its concentration via LV4. For nitrogen-doping, which involved 3-chloropyridine, an aromatic precursor, 1,2-dichlorobenzene was not included during synthesis. For silicon-, germanium-, and tin-doping, the heteroatom precursor was used as well as 1,2-DCB, which was in P1 in **Figure 2.8**.

Chapter 3—Application of GNSPs in supercapacitors

Adapted from

> Jacob D. Bagley, Dorte R. Danielsen, Nai-Chang Yeh, Significant capacitance enhancement via *in situ* exfoliation of quasi-one-dimensional graphene nanostripes in supercapacitor electrodes, under review by *ACS Omega*.

Personal contribution: Fabricated materials, performed all characterizations except SEM, conceived exfoliation procedure, and participated in writing the manuscript.

Introduction

Extensively studied supercapacitor active materials include pure graphene,[107] heteroatom-doped graphene,[108,109] and graphene composites (*e.g.*, with metal oxide nanoparticles).[110] Graphene is attractive as a supercapacitor electrode material due to its high surface area as a two-dimensional material, high carrier mobility, and quantum capacitance.[48,111] An additional advantage is that graphene (as well as other carbon based materials) is also easily deposited on surfaces in precise configurations to make interesting devices such as microsupercapacitors.[112] However, processing of graphene sheets into supercapacitor electrodes typically leads to stacking of graphene sheets,[32] reducing the surface area, and decreasing the carrier mobility,[113] such that the advantages of graphene are often not realized in practical supercapacitor devices. Therefore, it is desirable to develop methods to obtain single-layer graphene in practical supercapacitor devices. Indeed, many reports focus on developing methods to increase the surface area of nanocarbons.[114]

Methods of producing single-layer graphene sheets in high yield include oxidative unzipping of carbon nanotubes,[115] oxidative chemical exfoliation,[116] liquid phase exfoliation,[39] and electrochemical exfoliation.[117] Of these approaches, we find

electrochemical exfoliation particularly interesting because it can potentially be applied *in situ* in a packaged supercapacitor electrode, as demonstrated in this contribution. Electrochemical exfoliation is the process of separating graphite or multilayer graphene into single-layer graphene sheets by applying a voltage to intercalate large ions, separating graphite sheets to single-layer graphene. This has been accomplished in organic,[117] aqueous,[118] and ionic liquid solutions[119] and has been used to produce graphene for field effect transistors,[120] energy storage,[121] transparent conductive electrodes,[122] and gas sensors.[123]

Methods of producing single-layer graphene in high yield include oxidative unzipping of carbon nanotubes,[115] oxidative chemical exfoliation,[116] liquid phase exfoliation[39] and electrochemical exfoliation.[117] Electrochemical exfoliation is the process of separating graphite or multilayer graphene into single-layer graphene sheets by applying a voltage to intercalate large ions, separating graphite sheets to single layer graphene. This has been done in organic,[117] aqueous[118] and ionic liquid[119] solutions and has been used to produce graphene for field effect transistors,[120] energy storage,[121] transparent conductive electrodes[122] and gas sensors.[123] However, if single-layer graphene is desired for these applications, researchers should be cognizant that packaging the exfoliated graphene into a device typically results in stacking of graphene sheets.[32] Of these, we find electrochemical exfoliation particularly interesting because it can potentially be applied *in situ* in a packaged supercapacitor electrode.

Although *in situ* exfoliation of graphitic electrodes typically catastrophically degrades the electrode performance due to loss of electrical contact as individual graphene sheets separate,[35,124,125] we demonstrate in this contribution that by employing quasi-one-

dimensional graphene nanostripes (GNSPs) as the active electrode material, the electrode supercapacitor performance can be enhanced upon *in situ* exfoliation due to the electrical conductivity maintained by the percolating nature of one-dimensional materials. These concepts, *i.e.*, electrical percolation by quasi-one-dimensional materials and *in situ* electrochemical modification of electrodes, are not new and have been explored in other materials,[126,127] but have not been simultaneously studied in carbon nanomaterials to the best of our knowledge. GNSPs are a graphene nanomaterial previously developed in our group that demonstrate chemical purity, good crystallinity, high carrier mobility and quasi-one-dimensionality (*e.g.*, GNSP dimensions are ~ 400 nm × 60 μm).[128] In our study of *in situ* exfoliated GNSPs we employ X-ray diffraction to study structural changes in the material and electrochemical impedance spectroscopy (EIS) to study the behavior of the electrode at various degrees of exfoliation and conjecture that the improved capacitance is due to an increase in surface area.

Results

The quasi-one-dimensional nature of GNSPs is demonstrated in **Figure 3.1**. **Figure 3.1a** is a normal incidence SEM image of GNSPs on the growth substrate without further modification. Here, the one-dimensional nature is not apparent, but the fabricated material can be seen as a vertically oriented graphene material, where graphene grows vertically with respect to the growth substrate and forms a dense interconnected network of graphene sheets. For detailed reviews of vertically oriented graphene see references.[45,46] When dispersed onto a substrate (**Figure 3.1b**), our GNSPs (a particular class of vertically oriented graphene) become apparent as quasi-one-dimensional graphene, *i.e.*, graphene materials that are large in one dimension and small in the other dimensions. Several GNSPs

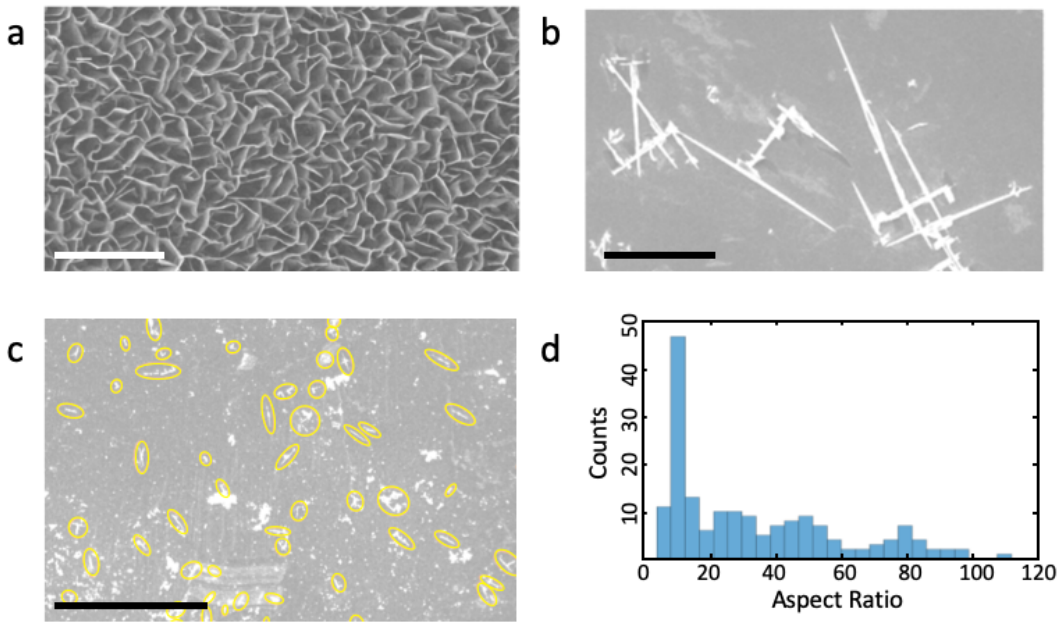

Figure 3.1. a) Normal incidence SEM image of as grown GNSPs. Scale bar: 8 µm. b) SEM image of individual dispersed GNSPs. Scale bar: 16 µm. c) Wide area SEM image of dispersed GNSPs with GNSPs highlighted by orange circles. Scale bar: 200 µm. d) Histogram of aspect ratios of 177 GNSPs.

are visible in **Figure 1b**, but a wider area image (**Figure 3.1c**) shows that the GNSP dispersion contains a large amount of GNSPs with varying dimensions. An analysis of 177 individual GNSPs reveals that the average width and length of GNSPs is ~ 450 nm and ~ 12 µm, respectively. A histogram of analyzed GNSPs aspect ratios is provided in **Figure 3.1d**, where the average aspect ratio is ca. 34:1, and the most frequent aspect ratio is ca. 10:1. (Note: these GNSPs do not exhibit quantum confinement effects as their typical width is ~ 450 nm while quantum confinement effects begin at widths of ~ 40 nm.[129]) The BET surface area was 64 m^2/g.

The successful fabrication of a graphene material was confirmed by Raman spectroscopy and X-ray photoelectron spectroscopy (XPS). The Raman spectrum is presented in **Figure 3.2a**. The *D* (1361 cm^{-1}), *G* (1589 cm^{-1}), and *2D* (2704 cm^{-1}) peaks are

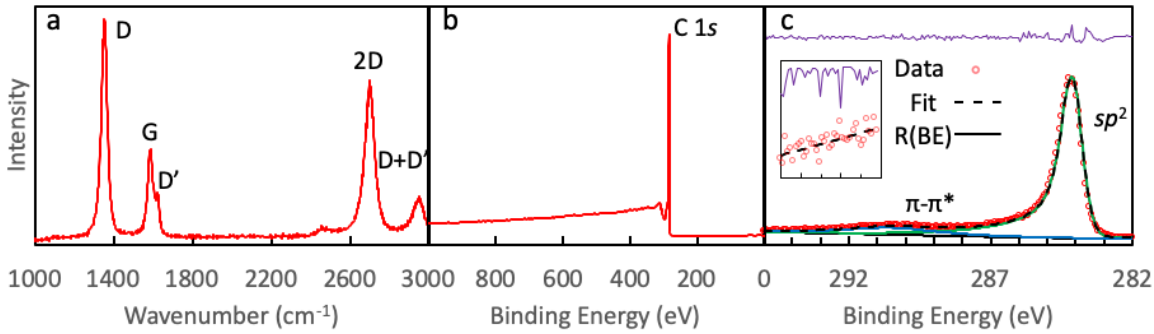

Figure 3.2. a) Raman spectrum, b) XPS survey spectrum and c) high-resolution XPS C 1*s* spectrum of our fabricated GNSPs with fit residuals (R(BE)). Inset: Fitting of section of spectrum outside of the peak area to determine intrinsic noise of measurement; Binding energy range: 292.5~295 eV.

characteristic of graphene, and the *D'* (1609 cm^{-1}) and *D+D'* (2945 cm^{-1}) peaks together with the *G* and *D'* peaks being well resolved classify this as a crystalline graphene nanomaterial according to the three-stage defect model.[130,131] We also acknowledge that the *D*-peak is very intense in this nanomaterial, which may be partially due to the abundant edges.

The XPS survey spectrum (**Figure 3.2b**) demonstrates the chemical purity of the graphene material, as the only visible peak (at ~ 285 eV) corresponds to C 1*s*. To further investigate the nature of the carbon in the material, we studied the C 1*s* peak by a high-resolution narrow scan (Fig. 2c). We fit the C 1*s* spectrum with two components corresponding to sp^2 hybridized C-C bonds (284.1 eV) and a π-π^* satellite (290.5 eV) with a Tougaard background. The sp^2 peak was fit to a Finite Lorentzian line shape with an asymmetry parameter of 0.18 and a full-width at half-maximum of 0.87 eV, consistent with previous reports.[132,133] (The Finite Lorentzian line shape is a convolution of Lorentzian and Gaussian functions with the Lorentzian function asymmetrically raised to different exponentials for binding energies greater than the peak center and binding energies less than the peak center, creating asymmetric tails, which is useful for modeling conducting

materials. The Finite Lorentzian line shape is an established method for modeling the C 1*s* sp^2 component, and various sources discuss its use and practical application.[134–136] Our function was defined as *LF(0.53,1.2,240,250,3)* in the CasaXPS software) The π-π^* satellite was fit with a symmetric Gaussian-Lorentzian function with a width of 3.6 eV. Because the sp^2 peak and the satellite were fairly well resolved, we did not impose constraints on peak widths and peak positions, but the fitted peak positions (*i.e.*, 6.4 eV the separation between the sp^2 and the satellite peak[137]) and the width of the sp^2 peak being consistent with literature confirm the fit is realistic. The residuals spectrum in **Figure 3.2c** also does not demonstrate the need for additional peaks. The fit gives an Abbe criterion of 0.67, which is not ideal as perfect noise around a fit gives an Abbe criterion of 1, but when fit to a line a linear portion of the spectrum absent of peaks (shown in **Figure 3.2c** inset) gives an Abbe criterion of 0.69, suggesting that the Abbe criterion of the peak fit is reasonable based on the noise in this spectrum. (For a practical discussion of judging goodness-of-fit by Abbe criterion, see Reference.[138])

The strong sp^2 peak and the presence of the π-π^* peak verify the graphene crystallinity, *i.e.*, domains with delocalized *p*-orbitals.[133,139] The combined results of Raman spectra and XPS data confirmed that the GNSPs are highly crystalline and chemically pure graphene material. Further characterization of the GNSPs, including transmission electron microscopy, energy-dispersive X-ray spectroscopy, selected area electron diffraction, and ultraviolet photoelectron spectroscopy can be found in reference.[128]

The GNSPs were packaged into a supercapacitor in a coin cell configuration, and the capacitance was measured by cyclic voltammetry at various scan rates between 2 V

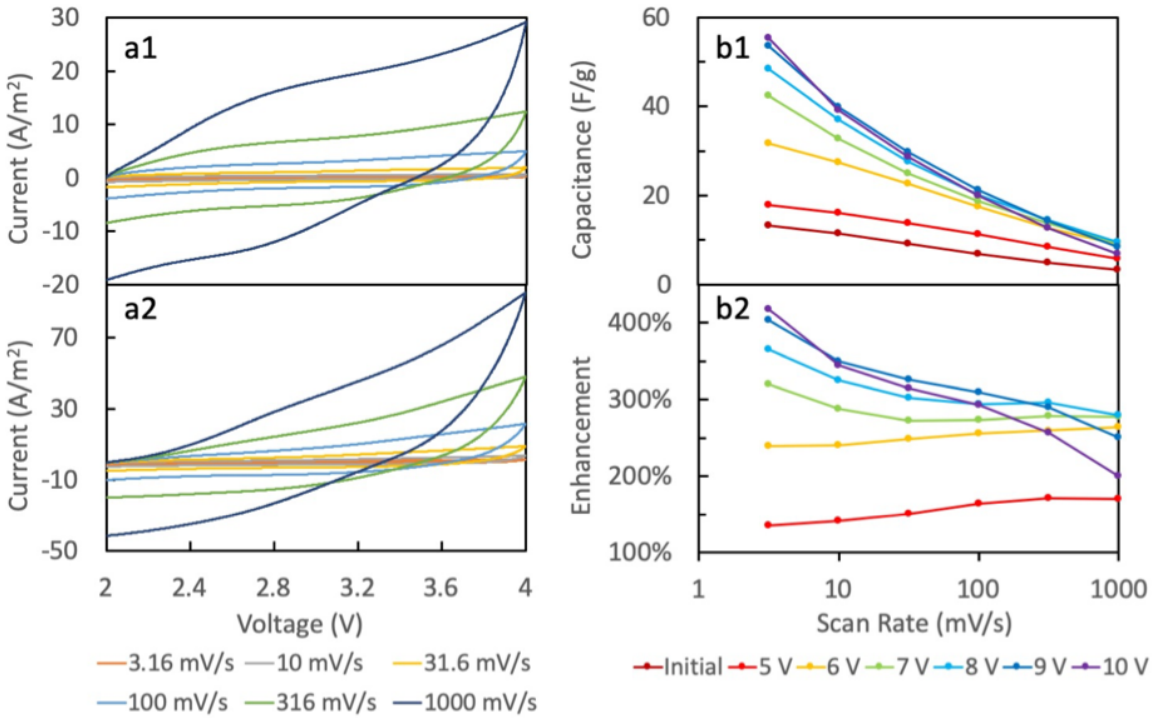

Figure 3.3. a1) Cyclic voltammograms of a pre-exfoliated GNSP electrode. a2) Cyclic voltammograms of a GNSP electrode exfoliated at 10 V. b1) Specific capacitance of each electrode as a function of the scan rate. Here the "initial" curve denotes the capacitance of pre-exfoliated GNSP electrode. b2) Capacitive enhancement of each exfoliated GNSP electrode with respect to the pre-exfoliated GNSP electrode as a function of the scan rate.

and 4 V as shown in **Figure 3.3a1**. The cyclic voltammograms were nearly rectangular, indicating a fairly ideal electrochemical double-layer capacitor process with little contribution from redox processes.[140] The non-idealities, such as the positive slope while charging and negative slope while discharging, may arise from slight changes in the intercalation state of Li^+ or PF_6^- (*e.g.*, Li^+ intercalation could occur at voltages as high as 2.5 V in disordered graphene materials),[37,141] which had also been reported previously in graphene supercapacitors.[107] Additionally, these electrodes demonstrated the classic capacitor behavior of increasing current response with increasing scan rate.[140]

Regarding the claim that Li+ intercalation could occur at ~ 2.5 V, we provide the following discussion. Disordered carbon materials (including graphene, due to stacking

disorder) typically do not demonstrate well defined lithium intercalation potentials.[35] For example, while galvanostatic lithiation and delithiation of crystalline graphite results in well-defined voltage plateaus (see Fig. 8 in reference[35]), galvanostatic lithiation and delithiation of graphene electrodes results in a quasi-exponential curves rather than voltage plateaus as in **Figure 3.4a**. The quasi-exponential curves suggest that the lithium intercalation potentials are continuously distributed throughout the voltage range (even at voltages as high as 2 ~ 3 V vs Li/Li^+). To demonstrate the intercalation phenomenon at ~ 2.5 V more quantitatively, we performed higher resolution galvanostatic discharge/charge measurements at ~ 2.5 V. **Figure 3.4b** (**Figure 3.4c**) shows the first 5 seconds of a galvanostatic discharge (charge) curve after holding the voltage for 5 minutes. A purely capacitive process would result in a linear line with some non-zero slope, while a purely faradaic process would result in a linear line with zero slope.[29] In practice, however, every electrode forms electric double-layers, so when currents or voltage biases are applied to an

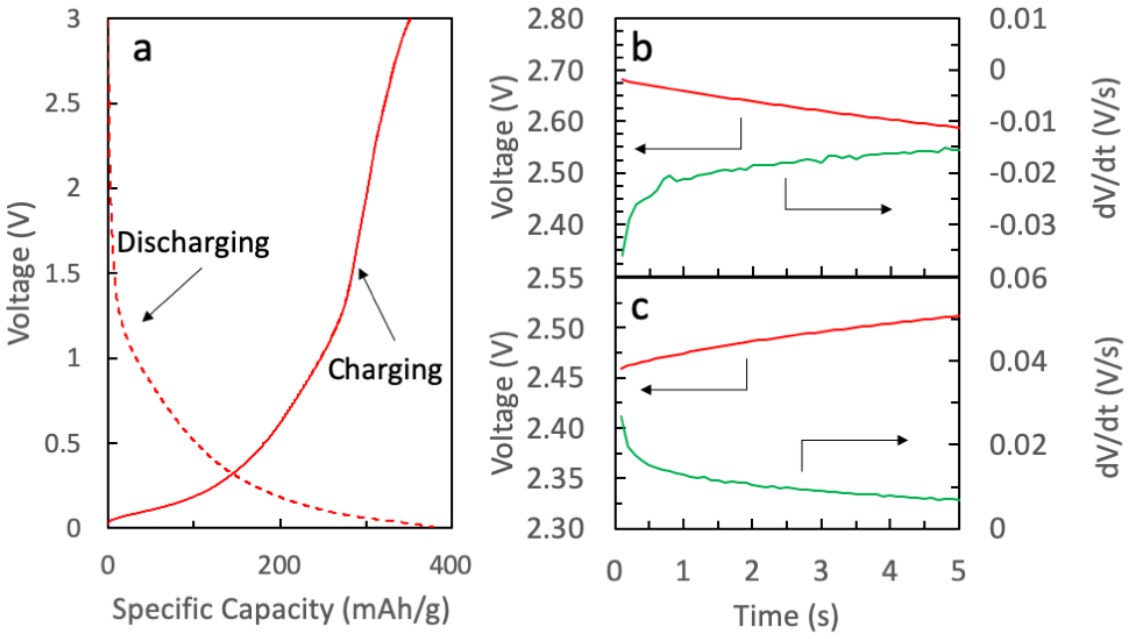

Figure 3.4. a) Galvanostatic discharge and charge of fifth cycle of graphene electrode. First 5 seconds of galvanostatic discharge (b) and charge (c) and their derivatives. Current: 100

electrode, the initial response is capacitive.[29] In addition, the intercalation potentials of graphene are not well defined so a plateau is not observed even after the electric double-layer response. This phenomenon of a fast current response, then a faradaic response is observed in **Figure 3.4b** (**Figure 3.4c**), where the slope is initially more negative (more positive). To emphasize this change in slope, we also plotted the derivative of voltage with respect to time. The derivative clearly demonstrate an initial slope that is more negative (more positive) than the subsequent response, suggesting that some faradaic process (*e.g.*, intercalation) is occurring at these voltages. Additionally, the change in slope should not be interpreted as series resistance as series resistance is not time dependent.[29]

Graphene electrodes were electrochemically exfoliated *in situ* by ramping the cell voltage to 1 V, holding the cell voltage at 1 V for three hours, then ramping the cell voltage to a high voltage, holding the cell voltage at the high voltage for three hours, then ramping down to 2 V. The high voltages ranged from 5 V to 10 V. The rationale for this voltage program was that a high voltage caused intercalation of PF_6^-,[124,142] which, as a large molecule, induced separation of graphene sheets (*i.e.* exfoliation), and the low voltage (1 V) caused intercalation of a Li^+-propylene carbonate complex, which also exfoliated the graphene.[35] We also performed these experiments without the 1 V exfoliation step, and the capacitance of these electrodes did not enhance as well as those that included the 1 V exfoliation step (See **Figure 3.5**).

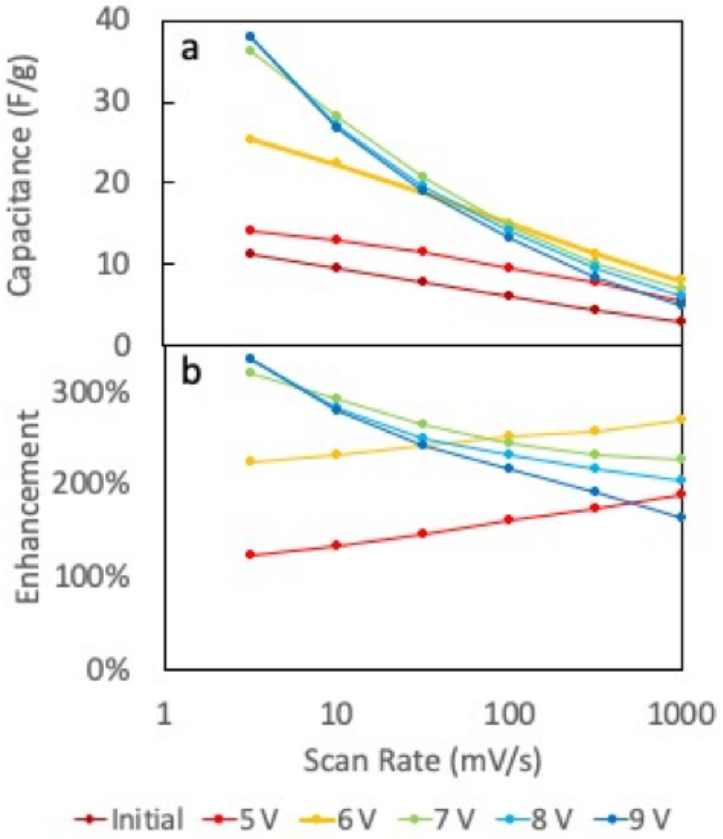

Figure 3.5. Capacitance (a) and enhancement (b) of graphene exfoliated *in situ* via high voltage exfoliation only.

Märkle et al[124] performed a similar exfoliation procedure (*i.e.*, using the same electrolyte (1 M $LiPF_6$ in propylene carbonate/dimethyl carbonate), the same counter/reference electrode (lithium metal) and similarly cycling between relatively low (3 V) and high voltages (5.5 V)) except employing a regular (not quasi-one-dimensional) graphitic material in the working electrode, but observed "[e]lectrical contact loss between the graphite particles themselves and/or particles and the current collector." The only significant difference between the system described in this contribution and the system studied by Märkle et al is that we are employing quasi-one-dimensional GNSPs while they did not, and, as demonstrated herein, instead of observing catastrophic device failure, we observe enhancement due to exfoliation.

Before proceeding we acknowledge that using high exfoliation voltages may initially seem concerning since the stability window of the electrolyte in this configuration is reported as only 6V.[143,144] Indeed, below we conjecture that this high voltage may cause some decomposition that affects ion transport. Further, such high voltages may be dangerous. However, in our experiments we did not observe damage or danger on a macroscopic scale, and the microscopic damages are slight. We believe this is because, although the voltage across the entire coin cell is large, the voltage gradient at any point within the cell is not so large. This behavior is typical of supercapacitors, as ions migrate to biased electrodes and screen the voltage,[29] and ion intercalation into the bulk of the GNSPs electrode may also provide some screening.

After exfoliation, the capacitance was measured again by cyclic voltammetry under the same conditions. The cyclic voltammograms for graphene exfoliated at 10 V is shown in **Figure 3.3a2**. The voltammograms of the electrode exfoliated at 10 V (**Figure 3.3a2**) revealed two differences from the pre-exfoliated graphene (**Figure 3.3a1**): I) the current at a given voltage was much higher, demonstrating a higher capacitance, and II) the non-ideal behavior, *i.e.*, the slope, was more uniform through the voltammogram. This may be due to intercalation behavior through the entire voltage range, which may be made possible by an increase in interlayer spacing spacing and decrease in intercalation potential.

We calculated the specific capacitance, C, the electrode at each degree of exfoliation (the pre-exfoliation capacitance and the capacitance after each exfoliation step) according to

$$C = \frac{\int I \, dV}{2\nu m \Delta V}$$

where $\int I\, dV$ is the integrated area of the current response (I) of the cyclic voltammetry curve with the voltage differential (dV), ν is the scan rate, m is the mass of the graphene and ΔV is the voltage window of the cyclic voltammetry scan. The capacitances are shown in **Figure 3.3b1**. These data follow the classic supercapacitor behavior of decreasing capacitance with increasing scan rate. For the lowest scan rate, the capacitance increased steadily with increasing exfoliating voltage. For the highest scan rate, however, exfoliation at 8 V resulted in the best performance, while exfoliation at 9 V and 10 V resulted in lower capacitance for high scan rates. This decrease in performance for exfoliation at 9 V and 10 V may be due to solvent decomposition on the electrode surface during exfoliation,[143,144] producing byproducts that impair ion transport to and from the electrode such that the capacitance is impaired for high scan rates but not low scan rates.

To quantitatively compare the performance of each exfoliated electrode with respect to the pre-exfoliated electrode, we calculated the capacitive enhancement at each scan rate (E_ν) according to

$$E_\nu = \frac{C_{exfoliated,\nu}}{C_{initial,\nu}}(100\%)$$

where $C_{exfoliated,\nu}$ is the specific capacitance at a scan rate, ν, of the exfoliated graphene and $C_{initial,\nu}$ is the specific capacitance at a scan rate, ν, of the pre-exfoliated graphene. **Figure 3.3b2** plots the capacitive enhancement at each scan rate and demonstrates an enhancement of 418% for graphene exfoliated at 10 V. Additionally, for graphene electrodes exfoliated at 5 V and 6 V, the enhancement *increases* with increasing scan rate, whereas for graphene electrodes exfoliated at 9 V and 10 V, the enhancement *decreases*

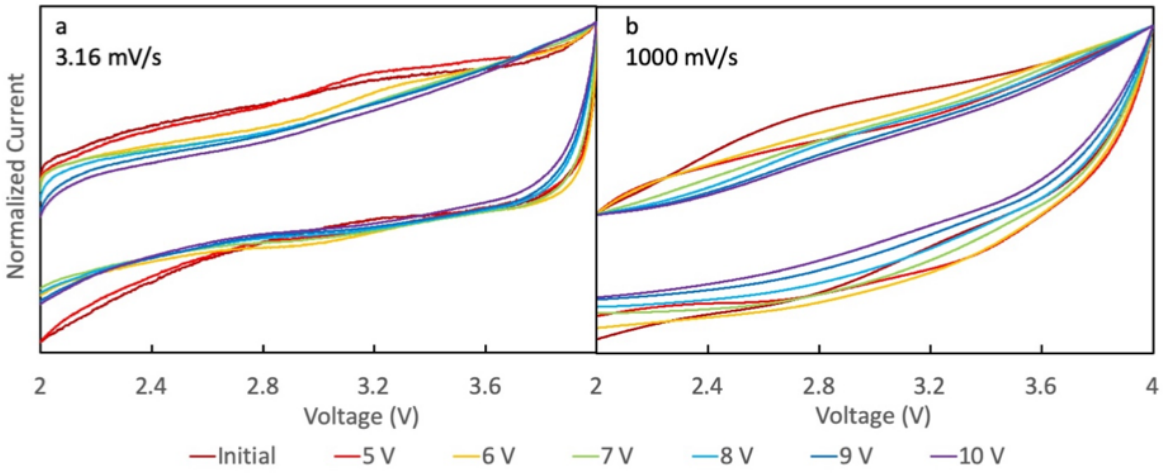

Figure 3.6. Normalized current response for each electrode at 3.16 mV/s (a) and 1000 mV/s (b).

with increasing scan rate. For graphene electrodes exfoliated at 7 V and 8 V the enhancement first decreases then increases with increasing scan rate.

To further understand this increase in capacitance, we investigated whether its origin was associated with an increase in non-faradaic charge storage (*i.e.*, double-layer capacitance) or in faradaic charge storage (*i.e.*, redox reactions). An increase in double-layer capacitance would result from an increase in surface area, while an increase in faradaic charge storage would result from chemical activation of the graphene material such that redox active sites were created. Non-faradaic and faradaic processes can be distinguished by comparing cyclic voltammograms with fast and slow scan rates. Generally, non-faradaic (capacitive) current dominates at fast scan rates, and faradaic current dominates at slow scan rates. Therefore, if a faradaic process is taking place at an electrode, then a redox peak at some voltage will be visible at low scan rates but will be hidden by the non-faradaic current at high scan rates.[29] To determine whether the increased capacitance observed here involved faradaic processes, we normalized the cyclic voltammogram current response for each exfoliation step at the slowest scan rate (**Figure**

3.6a) and the highest scan rate (**Figure 3.6b**). In both plots we found that the current curves were similar and quasi-rectangular for all electrodes, suggesting that the electrochemical processes did not change significantly with exfoliation.

Ideally, we could directly measure the surface area of exfoliated graphene materials (*e.g.*, via BET surface area measurement) to compare their surface area to the original material, but typical surface area measurements (*e.g.*, BET surface area measurement) would require *i*) a fairly large amount of material (compared to typical electrode masses) and *ii*) removing the graphene material from the coin cell current collector (*e.g.*, by scrapping it off), which would likely affect the surface area. Therefore, to further substantiate that the surface area increased with exfoliation, we extrapolated the double-layer capacitance (which is proportional to the surface area) from the cyclic voltammograms.

The initial current response due to a potential sweep is given by

$$i = \nu C_d \left[1 - \exp\left(-\frac{t}{R_s C_d}\right)\right]$$

where i is the current, ν is the voltage scan rate, t is the time, R_s is the solution resistance and C_d is the double-layer capacitance.[29] The initial current response of each electrode for a scan rate of 3.16 mV/s is shown in **Figure 3.7a**. The exponential component is visible in the initial current response, and with increasing exfoliation voltage the exponential component extends to longer times.

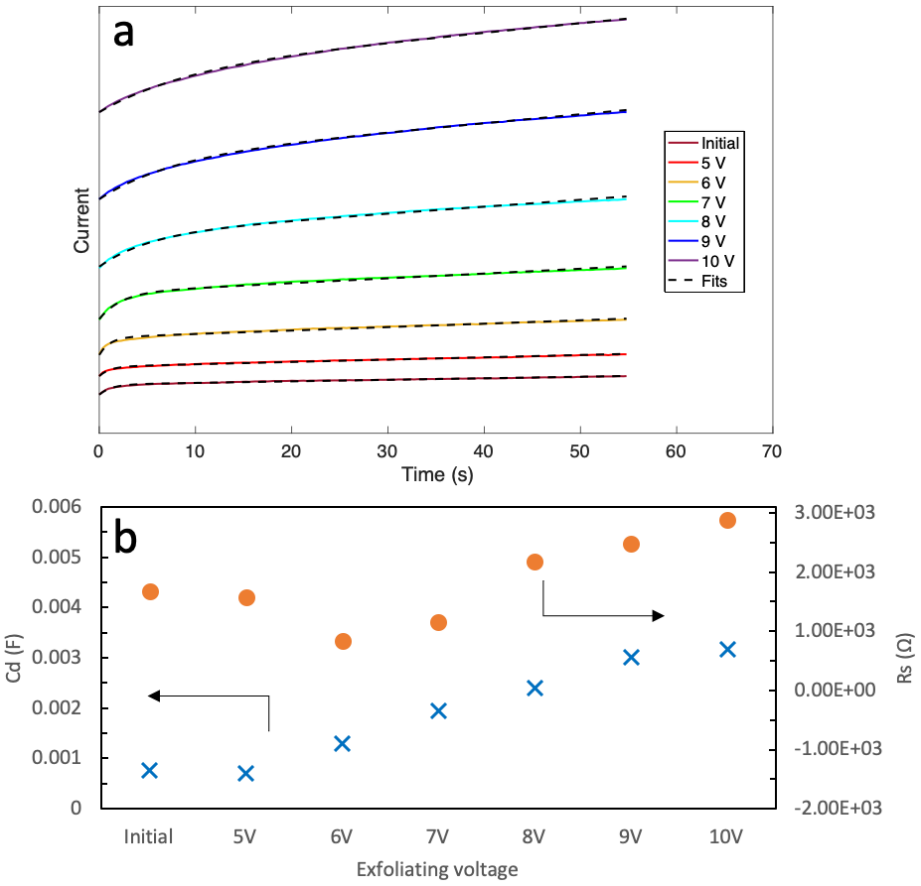

Figure 3.7. a) Initial current response for each degree of exfoliation. Scan rate 3.16 mV/s. b) Extrapolated double-layer capacitance and solution resistance for each degree of exfoliation.

To quantitatively understand the change in double-layer capacitance, we fit these curves to

$$i = \nu C_d \left[1 - \exp\left(-\frac{t}{R_s C_d}\right)\right] + (mt + b)$$

which is the previous equation with a linear component added to it. The linear component was added because the data in **Figure 3.7a** do not have zero slope after the exponential rise (perhaps due to intercalation processes, as discussed previously). The fitting results for C_d and R_s are plotted in **Figure 3.7b**. Indeed, exfoliation does increase the double-layer capacitance, suggesting an increase in surface area. Additionally, the solution resistance

decreases for exfoliation up to 7 V and increases for exfoliation above 8 V, which corroborates the electrochemical impedance spectroscopy data discussed below.

Next, we investigated the effect of exfoliation time on capacitance enhancement. For these experiments, the capacitance was measured then the GNSPs electrode was held at 1 V for 1 hour, then at 6 V for 1 hour, then returned to 2 V for a cyclic voltammogram capacitance measurement. This was repeated for 20 cycles. Similar measurements were also repeated using 10 V instead of 6 V. These voltages (6 V and 10 V) were chosen because 6 V is the electrochemical stability window of the electrolyte,[143,144] and previous measurements demonstrated the greatest enhancement at 10 V. The cycle dependent exfoliation using a high voltage of 6 V and 10 V is shown in **Figure 3.8**. In both cases exfoliation always enhanced the capacitance, but the number of cycles for maximum enhancement differed: For exfoliation at 6 V, the capacitance enhancement plateaued after 2 cycles and resulted in ~ 300% capacitance enhancement, whereas for exfoliation at 10 V, enhancement maximized at ~ 250% after 9 cycles then decayed with increasing cycles.

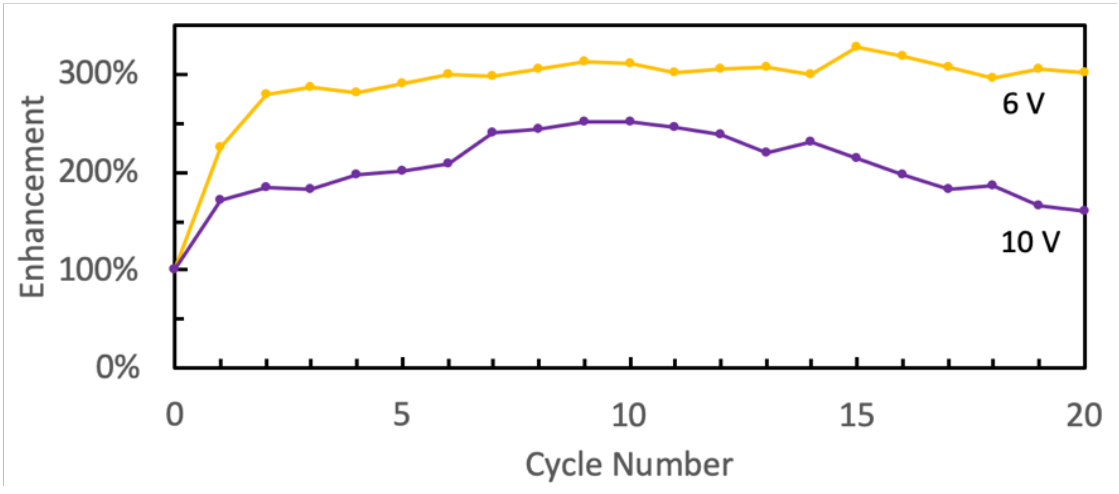

Figure 3.8. Cycle dependent exfoliation using a high voltage of 6V and 10 V.

The data shown in **Figure 3.8** contrasts with the data presented in **Figure 3.3** in two aspects: *i*) in **Figure 3.3** exfoliation at 10 V resulted in higher capacitance than exfoliation at 6 V, and *ii*) in **Figure 3.3** exfoliation at 10 V resulted in ~ 420% capacitance enhancement rather than ~ 250%. We resolve this discrepancy by considering that this electrolyte is not stable under a voltage gradient of 10 V,[143,144] and exfoliating at 10 V may cause solvent decomposition which is destructive to the capacitance. Additionally, exfoliating at lower voltages before exfoliating at 10 V may enable ion transport into the bulk of the electrode (*e.g.*, via pores) that helped screen the total voltage applied to the electrode so that the voltage gradient at the solution-electrode interface was not too intense. In other words, if the electrode was partially exfoliated before applying a high voltage, then when the high voltage was applied, the counter ions in the bulk of the electrode would help screen the voltage for the electrode-solution interface, leading to reduced electrolyte decomposition while enabling further exfoliation.

To better understand the cause of increased capacitance in exfoliated electrodes, we measured the XRD patterns of our GNSP electrodes exfoliated at different voltages for *i*) an as-grown sample, *ii*) graphene exfoliated at 6 V for 20 cycles, and *iii*) graphene exfoliated at 10 V for 20 cycles (**Figure 3.9)**. Interestingly, for both the as-grown graphene and graphene exfoliated at 6 V, the position of the [002] peak was similar, but for graphene exfoliated at 10 V, the [002] peak disappeared. According to Bragg's law ($d_{002} = n\lambda/2\sin\theta$ where n is a positive integer, λ is the incident X-ray wavelength and θ is the diffraction angle), the interlayer spacing in the as-grown graphene and graphene exfoliated at 6 V was 3.40 Å and 3.37 Å, respectively. Given that the [002] peak indicated the interlayer spacing, the presence of the [002] peak suggested that applying a voltage of 6 V

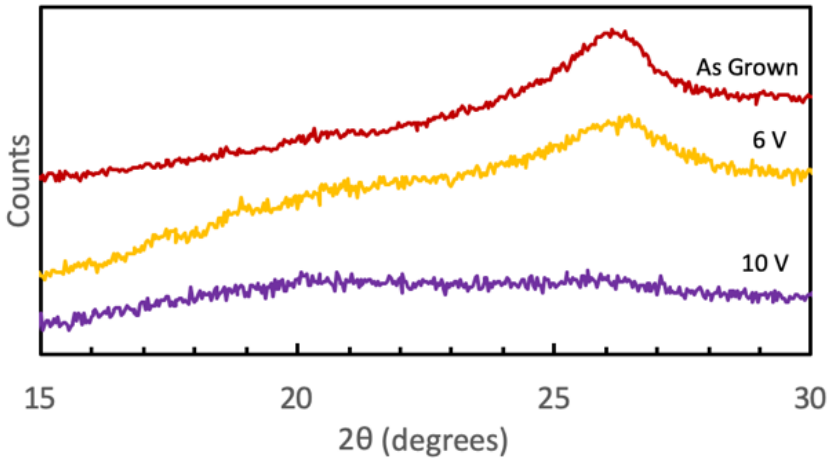

Figure 3.9. XRD pattern near the [002] peak for as-grown graphene, graphene exfoliated at 6 V, and graphene exfoliated at 10 V.

did not fully exfoliate the graphene (*i.e.*, separate it into individual monolayers) even though the peak intensity was reduced and linewidth broadened, whereas applying a voltage of 10 V completely exfoliated the GNSP sample so that there was no longer ordered c-axis stacking.

Finally, we used electrochemical impedance spectroscopy (EIS) to further understand the changes that took place during exfoliation that led to increased capacitance. Nyquist plots for each exfoliation step are shown in **Figure 3.10a**. The impedance data were fit to a modified Randles circuit (**Figure 3.10b**) with **Table 3.1** providing the fit parameters and their standard deviations, as determined by

$$\sigma(p_i) = \sqrt{\frac{2}{\frac{\partial^2}{(\partial p_i)^2}(\chi^2)}}$$

where $\sigma(p_i)$ is the standard deviation of the parameter i, and $\frac{\partial^2}{(\partial p_i)^2}(\chi^2)$ is the second derivative of the dependence of χ^2 (chi-squared) on a change in parameter i.[138] In the

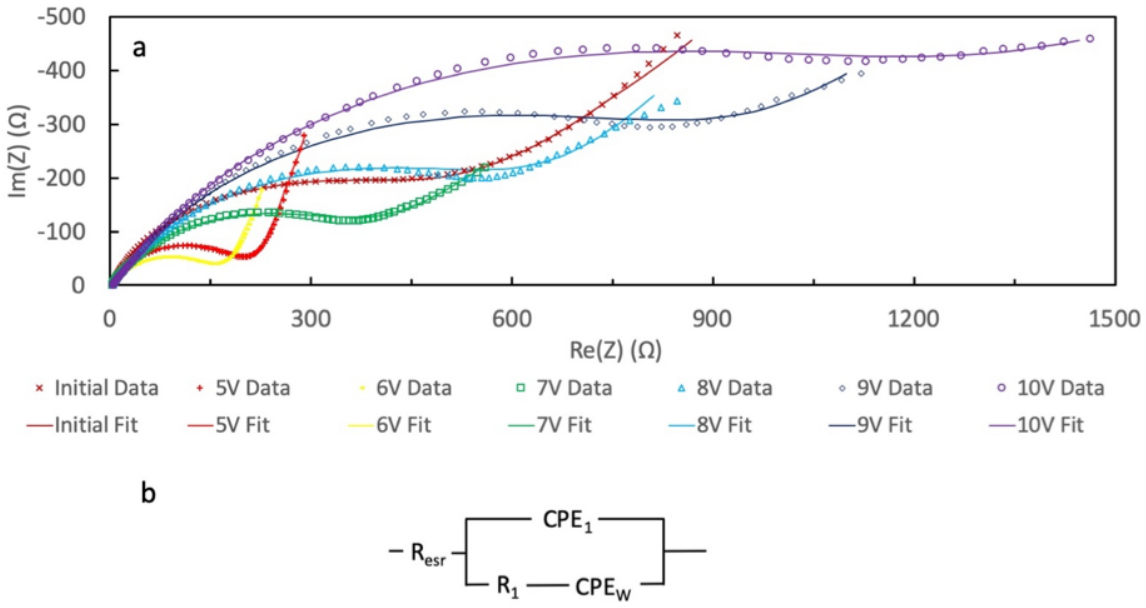

Figure 3.10. (a) Nyquist plots for all electrodes in the range of 0.1 MHz to 1 Hz. (b) Equivalent circuit models for Nyquist plots data.

equivalent circuit, the capacitor and Warburg diffusion elements are replaced with constant phase elements (CPE_1 and CPE_W, respectively) to account for non-idealities.

Before interpreting the equivalent circuits and model parameters, we introduce the mathematical relations of the circuit elements. The impedances of a capacitor (Z_C), Warburg element (Z_W) and constant phase element (Z_{CPE}) are defined as

$$Z_C = \frac{1}{i\omega C},$$

$$Z_W = \frac{1}{Q\sqrt{i\omega}},$$

$$Z_{CPE} = \frac{1}{Q(i\omega)^n},$$

where i is the imaginary number, ω is the radial frequency, C is the capacitance, R is the resistance, and n and Q are constants.[140] In the cases of $n = 1$ and $n = 0.5$, the constant phase element (CPE) becomes identical to the capacitor and Warburg element, respectively. Therefore, a CPE is often used to model non-ideal capacitors and Warburg

Table 3.1: Model fitting parameters of the data in Fig. 7a according to the circuit in Fig. 7b. Fit parameters' variances are given in parentheses.

	Initial	5 V	6 V	7 V	8 V	9 V	10 V
R_{esr} (Ω)	3.0 (0.3)	3.4 (0.3)	3.7 (0.3)	3.8 (0.3)	4.1 (0.3)	4.3 (0.3)	5.8 (0.4)
R_1 (Ω)	420 (10)	211 (3)	158 (3)	350 (10)	620 (10)	980 (20)	1160 (40)
n_1	0.815 (0.007)	0.81 (0.01)	0.77 (0.01)	0.743 (0.008)	0.718 (0.007)	0.696 (0.006)	0.711 (0.004)
Q_1 (S s^n_1) $\times 10^{-6}$	9.5 (0.7)	14 (1)	22 (3)	23 (1)	27 (1)	29 (1)	24.3 (0.8)
n_W	0.45 (0.02)	0.79 (0.02)	0.71 (0.02)	0.45 (0.03)	0.56 (0.03)	0.61 (0.04)	0.40 (0.05)
Q_W (S s^n_W) $\times 10^{-4}$	66 (1)	79 (4)	1.40 (0.08)	13.0 (0.3)	87 (3)	80 (4)	85 (3)

elements.[140,145] For a CPE that is modeling a capacitor, the extent to which n deviates below 1 can be interpreted as the "leakiness" of the capacitor, and for a CPE modeling a Warburg element, values of n deviating above 0.5 indicate diffusion within a porous three-dimensional structure (as opposed to diffusion near a perfect two-dimensional plane).[140,145,146]

We provide the following interpretation of the modeling parameters shown in **Figure 3.10b**. In the equivalent circuit, CPE_1 represents the double layer capacitance, R_1 represents intercalation charge transfer resistance and CPE_W represents diffusion behavior. Additionally, the "leakage" from CPE_1 may represent some intercalation behavior.

Exfoliating to 5 V and 6 V increased Q_1 (which is often interpreted as the capacitance[140]), decreased the intercalation resistance (R_1) and increased n_W (implying three-dimensional diffusion behavior). We physically interpret these parameter changes as an increase in surface area and decrease in intercalation energy barrier due to better

electrolyte contact and an increase in porosity of the material, respectively. Exfoliating at or above 7 V nearly restored the diffusion behavior to a Warburg element, which we interpret as the material becoming sufficiently exfoliated such that pores were large enough to behave quasi two-dimensionally.

For exfoliating voltages above 7 V, R_1 increased substantially with increasing exfoliating voltage. This may be due to electrolyte decomposition, which impeded ion transport[143,144] and likely responsible for the degraded performance at high scan rates for graphene electrodes exfoliated above 7 V (see **Figure 3.3**). Additionally, n_1 decreased to 0.67, indicating a very leaky capacitor. It is interesting, however, that these electrodes demonstrated an increased capacitance (at low scan rates, see **Figure 3.3**) despite electrolyte decomposition. On the other hand, for exfoliating voltages above 7 V, the MSE of the fit increased substantially, indicating that the device no longer complied with a Randles circuit model, which may be attributed to non-idealities caused by electrolyte decomposition.

Discussion

Our capacitance measurements demonstrate that GNSP electrodes can be exfoliated *in situ* to substantially enhance their capacitance (**Figure 3.3**). Comparison of the current responses of each electrode at both fast and slow scan rates indicates that the charge storage processes in the GNSP electrodes are non-faradaic (**Figure 3.6**), which suggests that the increase in capacitance is due to structural rather than chemical changes (*e.g.*, chemical functionalization). Comparing the cycle dependent exfoliated GNSP electrode (**Figure 3.8**) with the gradually exfoliated GNSP electrode (**Figure 3.3**) demonstrates that when exfoliating at 10 V, initial exfoliation at a lower voltage generally results in better

capacitance. Our XRD data (**Figure 3.9**) reveal that an applied voltage of 6 V does not fully exfoliate the GNSP electrode, whereas applying a voltage of 10 V completely exfoliates the electrode. Finally, our EIS data (**Figure 3.10**) suggests that the electrochemical processes have fundamentally altered with exfoliation: The diffusion behavior first shifts from a two-dimensional to a three-dimensional diffusion behavior, suggesting that the material becomes porous upon exfoliation. Additionally, the double-layer capacitance increases and the intercalation resistance decreases, suggesting better electrolyte contact with the material. As the material becomes sufficiently exfoliated, the diffusion returns to a two-dimensional behavior. The EIS data also suggests that some intercalation charge transfer has taken place. However, noting that the electrochemical processes are non-faradaic based on the cyclic voltammetry data, the intercalation charge transfer is likely minimal, although it may account for the observation of non-ideal capacitive charge storage.

We acknowledge that our reported capacitances (55 F/g, see **Figure 3.3b1**) are not particularly good, even for the best performing devices (Liu *et al*,[107] for example, report a capacitance of 154 F/g for a graphene electrode). However, obtaining a high capacitance was not the purpose of this study per se; rather, the purpose of this study was to determine whether graphene electrodes could be exfoliated in situ to enhance their capacitance. In order to meet this purpose we designed experimental conditions to probe this phenomenon rather than obtain a high capacitance. For example, our cyclic voltammetry window was 2 ~ 4 V, whereas it could have been 1 ~ 6 V (the stability window of the electrolyte), which would have increased the measured capacitance but would have also affected the exfoliation. Additionally, our choice of electrolyte ($LiPF_6$/propylene carbonate/dimethyl

carbonate) may not have resulted in the highest capacitance (*e.g.*, previous studies have shown higher capacitance in aqueous electrolytes[107]), but it was chosen because exfoliation of graphene/graphite in $LiPF_6$/propylene carbonate solutions has been a well-studied phenomenon.[35,117] Noting that electrochemical exfoliation of graphite has been demonstrated in other organic solvents, aqueous solvents and ionic liquids,[117–119] similar procedures could be applied to other graphene supercapacitor systems to optimize the enhancement of capacitance. Additionally, graphene supercapacitor electrodes could be exfoliated prior to being assembled in a final device to further improve on the capacitance.

Conclusion

We have demonstrated in this work an increase in capacitance of GNSP electrodes by *in situ* electrochemical exfoliation and provided experimental evidences for a substantial increase in the total surface area of graphene electrode after exfoliation. This development overcomes the typical restacking problems of graphene electrodes that suffer significant reduction of the effective surface area and frustrate the advantages of using graphene electrodes in supercapacitors. Through *in situ* electrochemical exfoliation, we observe more than 400% capacitance enhancement relative to the control samples. Thus, the method of *in situ* electrochemical exfoliation of graphene electrodes together with further optimized electrolyte solutions and/or exfoliation protocols is expected to be a promising approach towards fully realizing the benefits of graphene as superior supercapacitor electrode material.

While the developments in this work are encouraging, practical implementation of this *in situ* exfoliation procedure will require further research due to the low specific capacitance and uncertainty in the long-term performance of *in situ* exfoliated GNSPs

supercapacitor electrodes. In particular, the long-term term cycling stability of *in situ* exfoliation GNSPs will be the subject of future studies. While long-term cycling is typically routine analysis for supercapacitor electrodes, in this case long-term cycling is a time intensive multi-dimensional endeavor as cycling stability will likely be influenced by the exfoliating voltage, the voltage range during cycling and the electrolyte solution. Future studies will also investigate improving the specific capacitance of *in situ* exfoliated supercapacitor electrodes. For example, we are interested in mixing GNSPs with high capacitance carbon materials (*e.g.*, 2% GNSPs in activated carbon) and performing the exfoliation procedure, which may improve the surface area of the activated carbon with the GNSPs maintaining the electrical percolation. We are also interested in using exfoliated GNSPs for form percolating networks among high capacitance metal oxide nanoparticles. Overall, we consider *in situ* exfoliation together with the incorporation of quasi-one-dimensional GNSPs a promising research direction for achieving substantially improved supercapacitors.

Experimental

GNSP Fabrication. GNSPs were fabricated by plasma enhanced chemical vapor deposition (PECVD) described previously.[44,128] Specifically, a microwave induced hydrogen/methane plasma with trace 1,2-dichlorobenzene (Alfa Aesar, 99%) yielded GNSPs on a ~ 0.75 cm x ~ 1.25 cm copper foil (McMaster-Carr, 99.9%) in a ½" outer diameter quartz tube. The PECVD growth system was custom built and consisted of eight parallel deposition chambers each fitted with an Evenson Cavity (Opthos Instruments Inc., Frederick, MD, USA) excited by 70 W of 2.45 GHz microwave power source (ENS 4 x 200 W CPS, Sairem, Décines-Charpieu, France). The plasma volume was ~ 1 cm^3. H_2

(MATHESON, 99.999%) and CH_4 (MATHESON, 99.999%) gases were introduced to the chambers by mass flow controllers (MC series, Alicat Scientific, Tuscon, AZ), and 1,2-dichlorobenzene was placed in a vacuum sealed vial and introduced to the chamber through a leak valve. The pressure in the chamber before splitting into eight chambers was held at 4.8 Torr, the total flow rates of H_2 and CH_4 were 48 sccm and 5 sccm, respectively, and the ratio of CH_4 to 1,2-dichlorobenzene (3-chloropyridine) was ~ 2:1 as measured by a residual gas analyser (RGA; XT300M, Extorr Inc., New Kensington, PA, USA) placed upstream of the deposition chamber and connected via a capillary. The plasma was maintained for ~ 3 hours to synthesize sufficient graphene material for use as a supercapacitor electrode.

GNSP Characterization. The resulting GNSP material was characterized by scanning electron microscopy (SEM), the Bruanauer-the Bruanauer-Emmett-Teller (BET) surface area method, Raman spectroscopy, X-ray photoelectron spectroscopy (XPS) and X-ray diffraction (XRD). SEM was performed in a Hitachi S-4100 (Hitachi, Tokyo Japan) with an accelerating voltage of 5 kV. Individual GNSPs were obtained for imaging by sonicating the copper growth substrate with GNSPs grown on it in N-methyl-2-pyrrolidinone (NMP, Sigma-Aldrich, 99.5%)[39] for 30 minutes, centrifuging the dispersion to remove undispersed chunks of graphitic material at 850 rpm for 90 minutes, extracting one drop of dispersion and evaporating it over a silicon wafer in low vacuum at 70 ºC. The BET surface area was measured in a BELSORP-max volumetric instrument (BEL-Japan Inc.) via equilibrium N_2 adsorption isotherm at 77 K. Raman spectroscopy was performed in a Renishaw M-1000 Micro-Raman (Renishaw, Gloucestershire, UK) spectrometer operating with a 514.5 nm argon ion laser with a spectral resolution of 1 cm^{-1} and a spot size of ~ 20

μm. A dual-wedge polarization scrambler was inserted to depolarize the laser. XPS data were collected using a Kratos AXIS Ultra spectrometer (Kratos Analytical, Manchester, UK). The instrument was equipped with a hybrid magnetic and electrostatic electron lens system, a delay-line detector and a monochromatic Al Kα X-ray source (1486.7 eV). Data were collected at a pressure of ~ 5e-9 Torr with photoelectrons collected at 0° with respect to the sample. The analyzer pass energy was 80 eV for the survey spectrum and 10 eV for all other spectra. The instrument energy scale and work function were calibrated using clean Au, Ag, and Cu standards. The instrument was operated by Vision Manager software v. 2.2.10 revision 5. The data were analyzed using CasaXPS software (CASA Software Ltd). XRD data were collected in a PANalytical X'Pert Pro X-ray powder diffractometer using the Cu Kα1 line (λ = 1.5406 Å) with a tube voltage and current of 40 kV and 20 mA, respectively.

Coin cell preparation. Supercapacitor working electrodes consisted of GNSP material and polyvinylidene fluoride (PVDF, MTI Corporation, ≥99.5%) binder in a 88:12 ratio and were mixed in N-methyl-2-pyrrolidinone (NMP, Sigma-Aldrich, 99.5%) in a centrifugal mixer (AR-100 Thinky U.S.A., Inc., Laguna Hills, CA, USA) at 5000 rpm for 10 minutes. A thin layer of the resulting slurry was spread across a stainless-steel spacer (MTI Corporation) with a spatula and dried at 120 °C in vacuum for 16 hours. Two-electrode 2032-coin cells were assembled in an argon filled glove box (O_2: <0.1 ppm, H_2O: <0.1ppm). The counter/reference electrode was lithium foil (Sigma-Aldrich, 99.9%, 0.75 mm, mechanically cleansed immediately before cell assembly), and the separator was a propylene separator (Celgard 2400). The electrolyte was 1 M $LiPF_6$ in propylene carbonate/dimethyl carbonate (1:1 mixture by volume, both Sigma-Aldrich, ≥99%, stored

over molecular sieves, 3 Å, Beantown Chemical), and ~ 8 drops of electrolyte were used in each coin cell. The electrolyte was mixed in a dried HDPE bottle.

Electrochemical Characterization. All electrochemical measurements were performed on a Reference 600 (Gamry Instruments, Warminster, PA, USA). Capacitance was measured by cyclic voltammetry between 2 ~ 4 V at scan rates of 3.16, 10, 31.6, 100, 316, and 1000 mV/s. Electrochemical impedance spectroscopy measurements were taken potentiostatically at 2 V with a rms voltage of +/- 5 mV. All voltages are with respect to Li/Li^+.

Electrochemical Exfoliation. Three *in situ* exfoliation procedures were investigated as follows. I) The voltage of the graphene electrode was ramped from open circuit potential (~ 2.7 V) to 1 V at a rate of 1 mV/s, held at 1 V for three hours, ramped to a high voltage at a rate of 1 mV/s, held at the high voltage for three hours, then ramped to 2 V at a rate of 1 mV/s. Then the cyclic voltammetry and electrochemical impedance spectroscopy measurements were performed at 2 V. This process was repeated for one cell such that the high voltage on the first cycle was 5 V, then the high voltage on the second cycle was 6 V, as so forth until the high voltage on the last cycle was 10 V. II) The voltage of the graphene electrode was ramped from open circuit potential to 1 V at a rate of 10 mV/s, held at 1 V for one hour, ramped to 6 V at a rate of 10 mV/s, held at 6 V for one hour, then ramped to 2 V at a rate of 10 mV/s, then the capacitance was measured by cycled voltammetry. This process was repeated twenty times. III) The voltage of the graphene electrode was ramped from open circuit potential to 1 V at a rate of 10 mV/s, held at 1 V for one hour, ramped to 6 V at a rate of 10 mV/s, held at 10 V for one hour, then ramped to 2 V at a rate of 10 mV/s,

then the capacitance was measured by cycled voltammetry. This process was repeated twenty times. All voltages are with respect to Li/Li^+.

Chapter 4—Fabrication of Pyridinic-Type Nitrogen-Doped GNSPs and Their Application in Li-ion Battery Anodes

Adapted from

> J. D. Bagley, D. Kishore Kumar, K. A. See, N.-C. Yeh, Selective formation of pyridinic-type nitrogen-doped graphene and its application in lithium-ion battery anodes. RSC Advances 10, 39562-39571 (2020). DOI: 10.1039/D0RA06199A

Personal contribution: Conceived the synthesis procedure, fabricated materials, performed most characterizations, and participating in writing the manuscript.

Introduction

Increasing the energy density of lithium-ion batteries (LIBs) is an important issue in energy research in order to meet growing energy demands and long-term sustainability.[15] The energy density of LIBs depends on the charge storage capacities and potentials of the battery electrode materials. Therefore, one approach to improve LIB energy density is to increase the capacity of the anode, *i.e.*, the amount of lithium that the anode can reversibly accommodate. The current industry standard LIB anode material is graphite, and the processing of graphite for LIBs has been developed to the point that its practical performance is approaching its theoretical capacity.[20,147] Therefore, new materials are being explored to develop next-generation high energy density LIB anodes.[20] Among them, doping graphene with heteroatoms (*e.g.*, nitrogen, boron, etc.) as the anode material is an appealing approach because doped graphene LIB anodes have demonstrated reversible capacities greater than 1000 mA h g−1 (167% higher than graphite) with good lifetimes (>500 cycles).[148–154] Additionally, doped graphene is chemically similar to graphite so that it is compatible with current LIB assemblies (*e.g.*, electrolyte compatibility).

Although doped graphene anodes have demonstrated good performance, the effects of dopant type and dopant configuration on LIB performance is not well understood. This gap in knowledge is in part due to the difficulty in preparing graphene with a single dopant type in a specific configuration, such that measurements to date generally involve convoluted effects from multiple dopants and/or different dopant configurations.

Nitrogen is the most studied graphene dopant, and nitrogen can substitute into the graphene lattice in three different configurations that are termed as graphitic, pyrrolic, and pyridinic, as illustrated in **Figure 4.1**.[155,156] At the graphitic sites, nitrogen bonds to three carbon atoms and preserves the graphene honeycomb lattice. At the pyrrolic sites, nitrogen is adjacent to a vacancy defect and bonds to two carbons that are part of a five-membered ring. At the pyridinic sites, nitrogen is adjacent to a vacancy defect and bonds to two carbons that are part of a six-membered ring. In addition to their structural characteristics, these sites differ electronically so that the specific sites can be identified and quantified by X-ray photoelectron spectroscopy (XPS).[155] Among different types of nitrogen-doped graphene sites, the pyridinic type has been conjectured to yield the highest lithium storage capacity based on empirical results, although LIB applications of nitrogen-doped graphene with purely pyridinic-sites has never been accomplished so that the conjecture cannot be directly verified.[154–158] Thus, the purpose of this work is to examine the validity of current conjectures by studying the performance of nitrogen-doped graphene nanomaterials with predominant pyridinic-type doping in a LIB anode configuration.

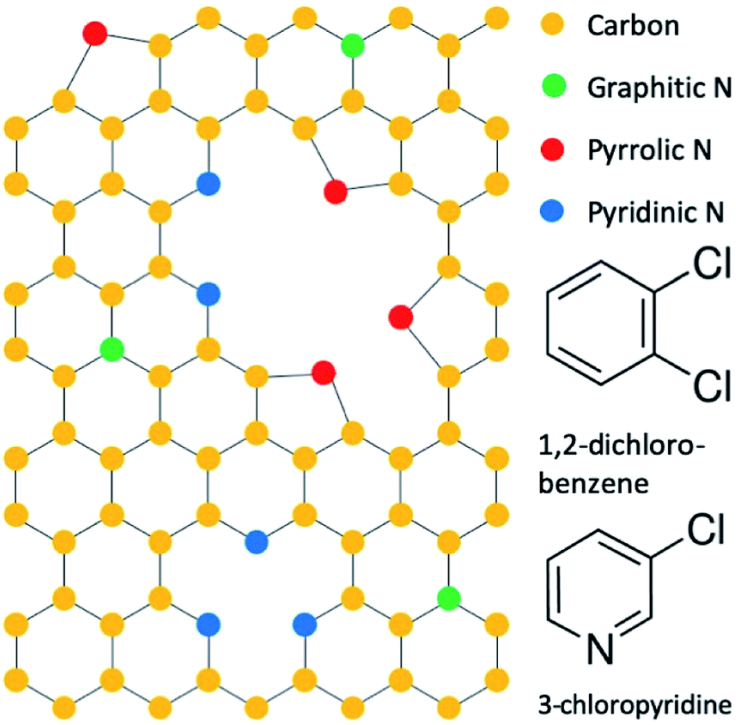

Figure 4.1: Configuration of nitrogen dopants in graphene and precursor molecules 1,2-dichlorobenzene and 3-chloropyridine.

Herein, we report the synthesis of nitrogen-doped graphene nanostripes (N-GNSPs) with predominantly pyridinic sites and the application of such N-GNSPs as the anode material in LIBs. In addition, we report for the first time post-mortem XPS characterization that reveals direct evidences for chemical changes at the nitrogen doped sites during the LIB operation. Although our N-GNSPs have a similar nitrogen content (~8%) as other reports and an unprecedentedly high percentage of pyridinic content (>86% of the nitrogen sites), these materials only demonstrate limited enhancement (~13%) in gravimetric lithium storage capacity when compared to undoped graphene nanostripes (GNSPs). We also observe irreversible chemical changes at the nitrogen sites via XPS during solid electrolyte interphase (SEI) formation, *i.e.*, the electronically insulating and Li+-conducting interface that forms on LIB electrodes due to solvent decomposition during the first cycle. These findings therefore imply that pyridinic sites alone are unlikely responsible

for the enhanced performance of nitrogen-doped graphene observed in previous studies, and further investigations are necessary to understand the effects of nitrogen doping on the performance of LIB anodes.

Experimental

Synthesis of graphene materials. N-GNSPs were synthesized by modifying the plasma enhanced chemical vapour deposition (PECVD) synthesis for GNSPs that was previously presented by Hsu et al.[128] Specifically, a microwave induced hydrogen/methane plasma with trace 1,2-dichlorobenzene (Alfa Aesar, 99%), or 3-chloropyridine (Alfa Aesar, 99%) yielded GNSPs or N-GNSPs on Cu-substrates, respectively. The PECVD growth system was custom built and consisted of eight parallel deposition chambers. Each chamber included a 0.75 cm × 1.25 cm copper foil (McMaster-Carr, 99.9%) in a ½" outer diameter glass tube fitted with an Evenson cavity (Opthos Instruments Inc., Frederick, MD, USA) excited by a 2.45 GHz microwave power source (ENS 4 × 200 W CPS, SAIREM, Décines-Charpieu, France). All chambers simultaneously received 70 W of microwave power, which created a plasma volume of ~1 cm^3. H2 (99.999%) and CH4 (99.999%) gases were introduced to the chamber by mass flow controllers (MC series, Alicat Scientific, Tuscon, AZ, USA), and traces of 1,2-dichlorobenzne (3-chloropyridine) were introduced to the chamber via a leak valve from a vacuum sealed vial of 1,2-dichlorobenzne (3-chloropyridine). The pressure in the chamber before splitting into eight chambers was held at 3.8 Torr, the total flow rates of H2 and CH4 were 48 sccm and 5 sccm, respectively, and the ratio of CH4 to 1,2-dichlorobenzene (3-chloropyridine) was ~2:1 as measured by a residual gas analyser (RGA; XT300M, Extorr Inc., New Kensington, PA, USA) placed upstream of the deposition chamber and connected via a capillary, as detailed in *Note 1*

and schematically shown in **Figure 4.2**. The plasma was maintained for ~3 hours to synthesize sufficient graphene material for use as LIB anodes. We note that the synthesis yield was found to be linear with the growth time at a rate of ~ 6 mg/cm^2 hour per chamber on copper substrates, as described in *Note 2* and demonstrated in **Figure 4.3**. For each LIB electrode slurry (described in *Coin cell preparation*), we used 100 ~ 150 mg graphene. By employing all eight PECVD chambers in parallel for graphene growth, we were able to collect sufficient material in ~3 hours to make an electrode slurry which could make anodes for several coin cells.

Note 1. In order to fabricate large amounts of GNSPs efficiently, we built a PECVD deposition system with eight chambers in parallel shown in **Figure 4.2**. Input of hydrogen and methane gas is controlled by mass flow controllers (MFCs), and input of 3-chloropyridine is controlled by a leak valve which is connected to a vacuum sealed vial. The pressure is measured by a pressure gauge (PG), and the gas composition is measured

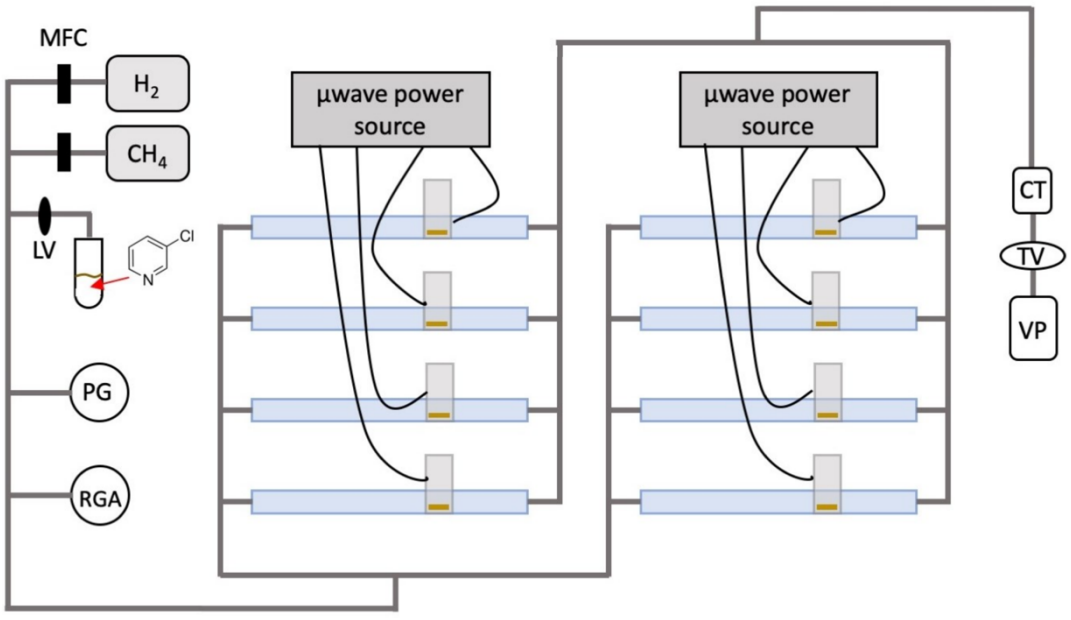

Figure 4.2: Schematic of the eight-chamber PECVD graphene growth system.

by a residual gas analyser (RGA). The gases are split to eight quartz chambers which each have Evenson cavities connected to microwave power sources. A cold trap (CT) captures harmful by products of the reaction (HCl, etc), and a vacuum pump (VP) is continually pumping the system. The pressure is controlled by a throttle valve (TV) that opens and closes with feedback from the pressure gauge to maintain a pressure setpoint. We have also measured the pressure in the quartz chamber, and under the conditions of this experiment (*i.e.*, a pressure of 4.8 Torr at PG and hydrogen and methane flow rates of 48 sccm and 5 sccm, respectively) the pressure in the chamber is ~ 500 mTorr, consistent with the previous report of Hsu *et al*.[128]

Note 2. The yield of N-GNSPs synthesized on copper substrates as a function of time is shown in **Figure 4.3** for one PECVD chamber. A fit of these data reveal a growth rate of ~ 6 mg/cm^2/hr. Our deposition chamber affords ~ 1 cm^2 substrates within each plasma cavity, so our eight chamber growth yields a growth rate of ~ 48 mg/hr of N-GNSPs.

Characterization of fabricated graphene materials. Raman spectroscopy was performed in a Renishaw M-1000 Micro-Raman (Renishaw, Gloucestershire, UK) spectrometer operating with a 514.5 nm argon ion laser with a spectral resolution of 1 cm^{-1} and a spot size of ~20 μm. A dual-wedge polarization scrambler was inserted to depolarize the laser. Scanning electron microscopy (SEM) was performed in a Hitachi S-4100 (Hitachi, Tokyo, Japan) with an accelerating voltage of 5 kV. Helium-ion beam microscopy (HIM) imaging was performed in a ZEISS ORION NanoFab (Pleasanton, CA, USA) with an accelerating voltage of 30 kV, a beam current of 1.2 pA and a working distance of 8.021

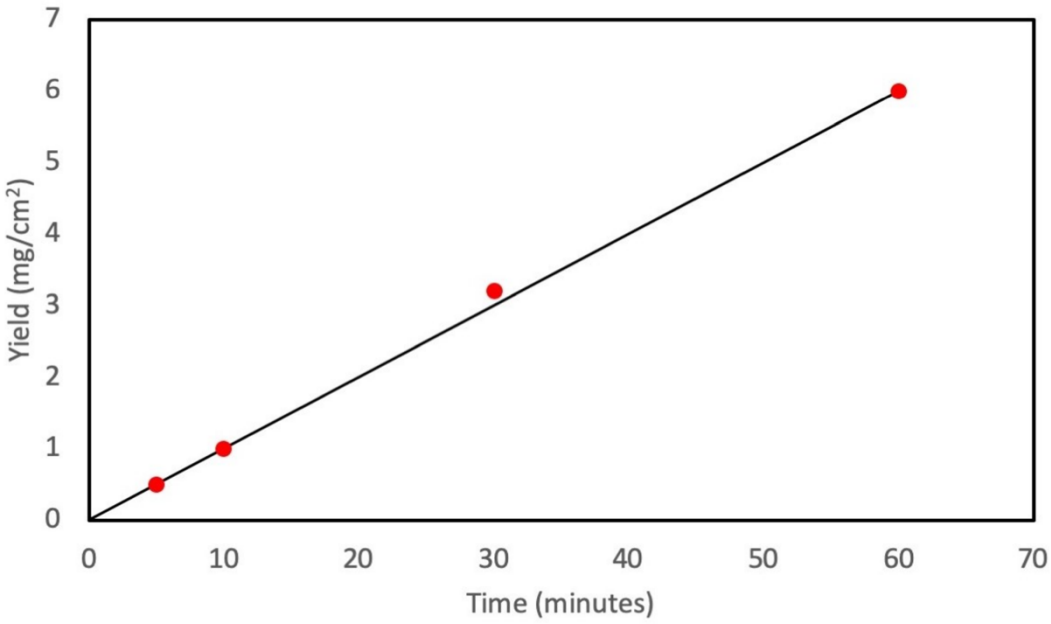

Figure 4.3: Yield of N-GNSPs-*vs.*-time obtained from one PECVD growth chamber.

mm. XPS data were collected using a Kratos AXIS Ultra spectrometer (Kratos Analytical, Manchester, UK). The instrument was equipped with a hybrid magnetic and electrostatic electron lens system, a delay-line detector and a monochromatic Al Kα X-ray source (1486.7 eV). Data were collected at a pressure of ~5×10^{-9} Torr with photoelectrons collected at 0° with respect to the sample. For the survey spectra the analyser pass energy was 80 eV and the step size was 1 eV, and for all other spectra the analyser pass energy was 10 eV and the step size was 0.025 eV. The instrument energy scale and work function were calibrated using clean Au, Ag, and Cu standards. The instrument was operated by Vision Manager software v. 2.2.10 revision 5. The data were analysed using CasaXPS software (CASA Software Ltd). The carbon sp^2 peaks were fit as asymmetric Gaussian–Lorentzian, and all other peaks were fit as symmetric Gaussian–Lorentzian. In addition, the carbon sp^3 and π–π^* satellite peaks were constrained to be 0.8 eV and 6.4 eV higher binding energy than the sp^2 peak, respectively. For post mortem XPS characterizations the

data were boxcar averaged using a width of eleven points to improve the signal-to-noise ratio.

Coin cell preparation. Working electrodes, which consisted of graphene material (GNSP or N-GNSP), carbon black (Super-P, Alfa Aesar, >99%) and polyvinylidene fluoride (PVDF, MTI corporation, >99.5%) binder in a 7:2:1 ratio, were mixed in N-methyl-2-pyrrolidinone (NMP, Sigma-Aldrich, 99.5%) in a centrifugal mixer (AR-100 Thinky USA, Inc., Laguna Hills, CA, USA) at 5000 rpm for 10 minutes. The resulting slurry was spread across copper foil (McMaster-Carr, 99.9%) using a doctor blade with a thickness of 0.2" and dried at 120 °C in vacuum for 16 hours ~7/16" diameter circular electrodes were cut from the dried slurry/copper foil. Separately, as-deposited N-GNSPs on the copper growth substrate were used as working electrodes. Two-electrode 2032 coin cells (MTI) were assembled in an argon filled glove box (with O_2 < 0.1 ppm and H_2O < 0.1 ppm). The counter/reference electrodes were lithium foil (Sigma Aldrich, 99.9%, 0.75 mm, mechanically cleansed immediately before cell assembly), and the electrolyte was 1 M $LiPF_6$ (Sigma Aldrich, ≥99.99%) in ethylene carbonate/dimethyl carbonate (1:1 mixture by volume, both Sigma Aldrich, ≥99%). Dimethyl carbonate was stored over molecular sieves (3 Å, Beantown Chemical) prior to use, and the electrolyte was mixed in a dried HDPE bottle. A polypropylene separator (Celgard 2400) was used and ~8 drops of electrolyte were used in each coin cell. Details of the coin cell fabrication procedure are given in *Note 3* and schematically shown in **Figure 4.4**. After electrochemical cycling, coin cells were disassembled in an argon filled glovebox, and the working electrodes were rinsed with dimethyl carbonate and transferred in an argon filled container directly to the XPS ultrahigh vacuum chamber for post mortem XPS characterization.

Note 3. The procedure for fabrication two types of LIB coin cells with N-GNSPs as the anode is schematically shown in **Figure 4.4**.

Electrochemical characterization. All electrochemical measurements were performed on a Reference 600 (Gamry Instruments, Warminster, PA, USA). Galvanostatic charge–discharge measurements were taken at indicated current densities within a voltage range of 3 V to 0.01 V.

Results

Pyridinic N-GNSP synthesis rationale and comparison to previous syntheses. We accomplished synthesis of predominantly pyridinic type N-GNSPs by modifying precursors used in our previous synthesis of undoped GNSPs.[128] In the original synthesis, trace content of 1,2-dichlorobenzene (structure shown in **Figure 4.1**) in a hydrogen/methane plasma resulted in growth of high quality (in terms of the chemical purity and crystallinity) vertically oriented graphene on a copper substrate. We note that vertically oriented graphene refers to a class of graphene nanomaterials wherein graphene grows vertically with respect to the growth substrate forming wall-like nanostructures on the substrate.[45] We believe that in the synthesis of GNSPs, 1,2-dichlorobenzene forms benzene radicals in the plasma due to the weak C–Cl bonds, which then seed and propagate the graphene structure along with methane radicals assisting the growth and hydrogen radicals etching away defects. The role of methane and hydrogen was proposed by other researchers studying the growth of vertically oriented graphene,[45] and the role of 1,2-dichlorobenzene is corroborated by our previous findings of the RGA data showing substantial increase in C_6 and C_6H_6 during the growth of GNSPs in the presence of 1,2-

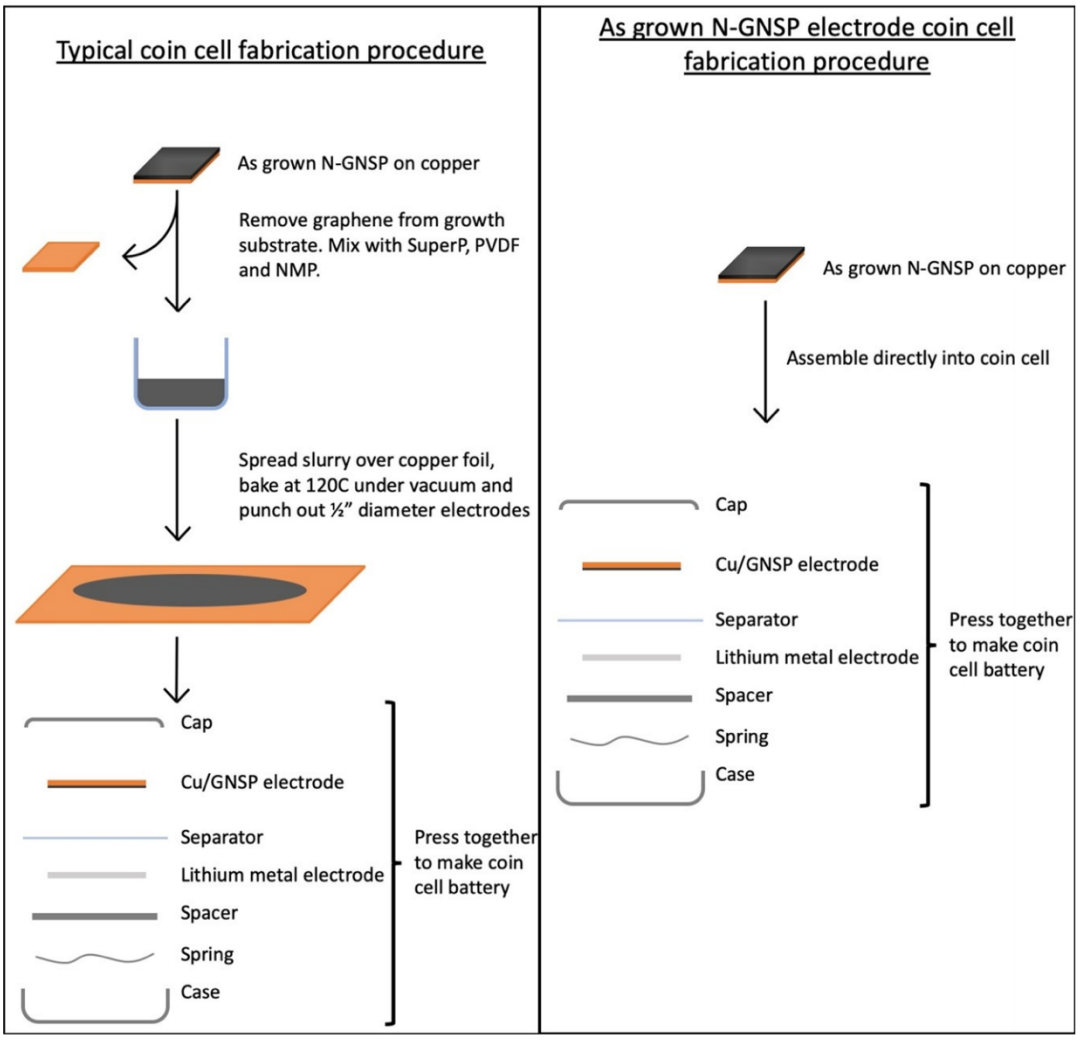

Figure 4.4: Schematic of typical coin cell fabrication (left) and fabrication of coin cell using N-GNSP not removed from the growth substrate.

dichlorobenzene.[128] For the synthesis of pyridinic type N-GNSPs, we replace 1,2-dichlorobenzene with 3-chloropyridine (see **Figure 4.1**). Similarly, we conjecture that 3-chloropyridine yields pyridine radicals in the plasma due to the weak C–Cl bond, which then seed the N-GNSP structures. We further conjecture that the use of 3-chloropyridine for graphene growth yields predominantly pyridinic-type N-GNSPs (see Section *Characterization of the as-grown material*) because the bonding configuration of nitrogen in 3-chloropyridine resembles the bonding configuration of nitrogen in pyridinic graphene sites.

As demonstrated in Section *Characterization of the as-grown material*, we find that this method indeed produces N-GNSPs that are >86% pyridinic-type doping for the nitrogen-doped sites. To the best of our knowledge, this is the highest fraction of pyridinic-type doping that has been accomplished with high yield and good crystallinity. For comparison, we briefly summarize here previous reports of related studies: Bang *et al*.,[159] Mombeshora *et al*.,[160] and Yasuda *et al*.[161] reported selective synthesis of pyridinic type nitrogen-doped graphene. However, the Raman peaks of each of these materials were relatively wide, indicating structural disorder.[130] Yang et al. reported a synthesis of nitrogen-doped graphene with fairly narrow Raman peaks, but the pyridinic doping content was only ∼50%.[162] Wisitsoraat *et al*. reported a nitrogen-doped graphene synthesis with narrow Raman peaks, but the doping type was completely pyrrolic.[163] Finally, Luo *et al*.[164] reported a selective synthesis of pyridinic type nitrogen-doped graphene with narrow Raman peaks, but the material was monolayer graphene, and thus the yield was insufficient for applications in LIB.

Characterization of the as-grown material. Graphene nanomaterials fabricated by the aforementioned PECVD methods were characterized by SEM, helium-ion beam microscopy (HIM), Raman spectroscopy, XPS and electrochemical methods. Normal incidence SEM images of as grown GNSPs and N-GNSPs are shown in **Figure 4.5A** and **B**, respectively. The top edge of the vertical graphene sheets are visible as bright lines in the images. Pores between vertical graphene sheets are darker in the image because electrons cannot escape to the detector from the deep pores. Sheets that do not stand perfectly vertical are visible as medium contrast points in the image. Visually, the GNSPs and N-GNSPs are structurally similar, *i.e.*, they have similar pore and sheet sizes. A cross

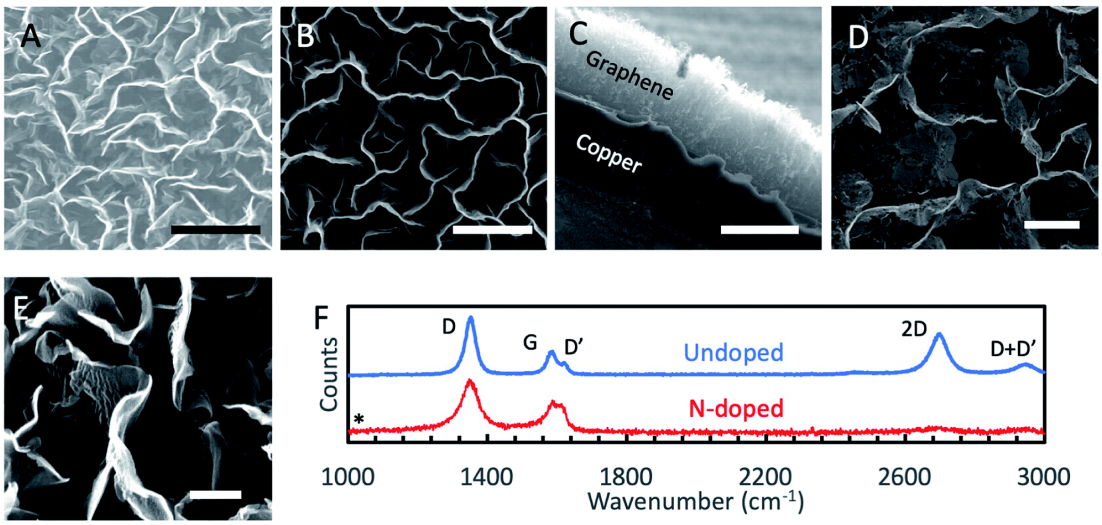

Figure 4.5: (A) Normal incidence SEM image of the as-grown GNSPs. Scale bar: 2 µm. (B) Normal incidence SEM image of the as-grown N-GNSPs. Scale bar: 2 µm. (C) Cross sectional SEM image of the as-grown N-GNSPs. Scale bar: 20 µm. (D) Normal incidence HIM image of the as-grown N-GNSPs, showing perforations at the edges, which we conjecture to result from the vacancies associated with the pyridinic sites. Scale bar: 1 µm. (E) Normal incidence HIM image of the as-grown GNSPs, showing no perforations at the edges. Scale bar: 200 nm. (F) Raman spectra of the undoped GNSPs and N-GNSPs, showing significantly suppressed 2D-band in N-GNSP, which may be attributed to the substantial presence of vacancies due to N-doping. The absence of a peak at 1034 cm^{-1} (marked by an asterisk) demonstrates residual 3-chloropyridine is not present on the sample.

sectional image is shown in **Figure 4.5C**, where the height of the vertical graphene nanomaterial measures at ~20 µm. To further differentiate the microscopic structures of GNSPs and N-GNSPs, we employed HIM imaging, which can resolve features as small as ~3 nm without damaging graphene under correct experimental conditions.[165] **Figure 4.5D** displays a HIM image of N-GNSPs which reveals perforations in the N-GNSPs sheets, whereas **Figure 4.5E** does not show perforations in the GNSPs sheets. Further, previous transmission element microscopy studies on GNSPs do not reveal perforations in GNSPs sheets.[128] We conjecture that pyridinic sites are present at the edges of the perforations, and the perforations are the result of vacancies associated with the pyridinic sites.

The Raman spectrum (**Figure 4.5F**) of GNSPs and N-GNSPs nanomaterials confirms the growth of graphene with the characteristic *D* (1361 cm^{-1}), *G* (1589 cm^{-1}) and *2D* (2704 cm^{-1}) peaks.[131] These materials also exhibit the *D′* (1609 cm^{-1}) and *D* + *D′* (2945 cm^{-1}) peaks which together with the *G* and *D′* peaks being well resolved classify the samples as nanocrystalline graphene material according to the three stage defect model.[130,131] We acknowledge that the *D*-peak is very intense in these graphene samples, which is in part due to the abundant edges.[128]

Comparing the GNSP and N-GNSP spectra, we find that the intensity ratios and the full-width-half-maximum (FWHM) of the *D* and *G* peaks are similar, whereas the *2D* peak is much suppressed in N-GNSPs relative to the undoped GNSPs, which is consistent with previous observation of N-doped graphene materials and may be attributed to the presence of vacancies associated with the N-doped sites.[155,166] The absence of residual 3-chloropyridine on the sample is confirmed by the absence of a peak in the Raman spectrum at 1034 cm^{-1} (marked by an asterisk), which is the position of a very strong 3-chloropyridine Raman signal.[167]

We conducted XPS studies to quantitatively determine the chemical composition and doping type in our materials (see **Table 4.1** for a compositional analysis of the N-GNSPs). The survey spectrum of the undoped GNSP material (**Figure 4.6A**) shows a pure carbon material. The C-1*s* spectrum of the same undoped GNSP material (**Figure 4.6B**) was fit with three peaks corresponding to sp^2 hybridized C–C bonds (284.9 eV), sp^3 hybridized C–C bonds (285.7 eV), and a π–π^* satellite (291.4 eV). The strong sp^2 peak and the presence of the π–π^* peak verify the graphene crystallinity, *i.e.*, domains with

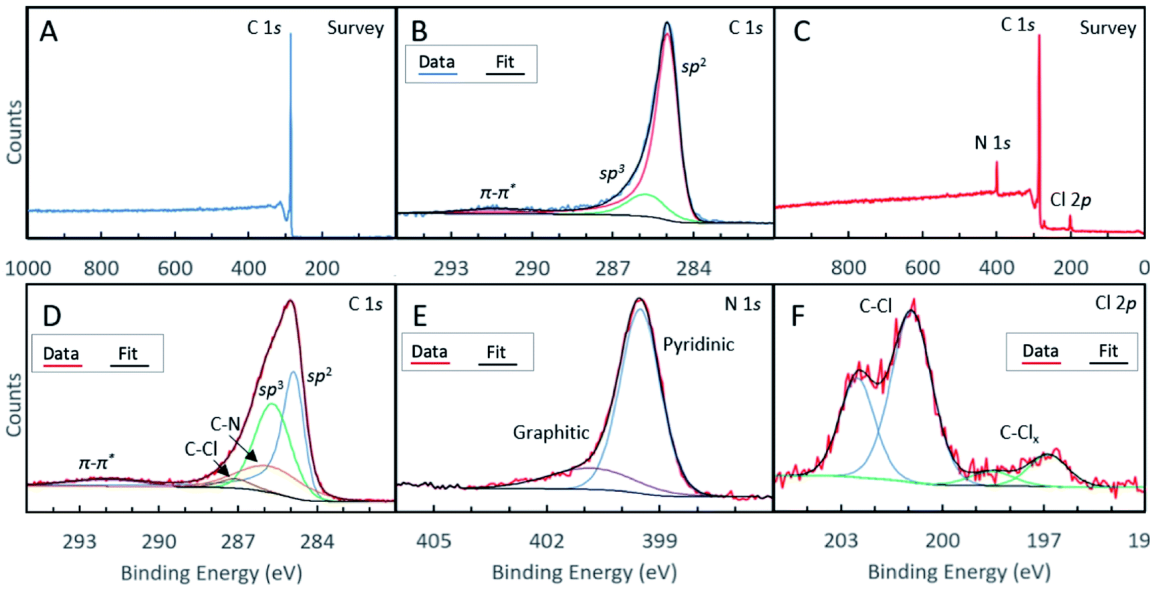

Figure 4.6. (A) XPS survey spectrum of undoped GNSPs, showing pure carbon composition. (B) XPS high resolution C-1*s* spectrum of GNSPs. (C) XPS survey spectrum of N-GNSPs, showing 89.4% carbon, 7.5% nitrogen, and 3.1% chlorine. High resolution XPS spectra of N-GNSPs for (D) C-1*s*, (E) N-1*s*, and (F) Cl-2*p*.

delocalized *p*-orbitals.[133,139] The N-GNSP survey spectrum (**Figure 4.6C**) shows the material is composed of 89.4% carbon, 7.5% nitrogen and 3.1% chlorine. Notably, there is no oxygen peak in our N-GNSPs (even though the sample was exposed to air), which is in contrast to the typical presence of oxygen in other doped graphene materials made at scales appropriate for LIB application.[148–154]

The C-1*s* high resolution spectrum of N-GNSPs (**Figure 4.6D**) is analysed by considering five components that correspond to sp^2 hybridized C–C bonds (284.9 eV), sp^3 hybridized C–C bonds (285.7 eV), C–N bonds (285.8 eV), C–Cl bonds (287.1 eV), and a π–π^* satellite (291.9 eV). The C–C bonds and the satellite peak assignments are justified by the literature (*i.e.*, the peak positions and relative spacings are consistent with previous reports),[168] and the C–Cl and C–N peak assignments are justified by comparing the relative peak intensities of carbon, nitrogen and chlorine components (**Table 4.1**). We acknowledge

Element	Configuration	Peak position (eV)	Concentration (%)	Fraction of total composition (%)
C			89.4	
	sp^2	289.4		24.0
	sp^3	285.7		30.6
	C–N	285.8		16.6
	C–Cl	287.1		3.1
	π–π*	291.9		17.8
N			7.5	
	Pyridinic	399.5		6.5
	Pyrrolic	401.5		1.0
Cl			3.1	
	C–Cl	202.5/200.9		2.8
	$C–Cl_x$	197.8/196.7		0.4

Table 4.1. Compositional analysis of the N-GNSP material from XPS fitting. (Slight discrepancies between fractions and sums are due to rounding)

here that the sp^3-hybridized C-component in the N-GNSP sample is relatively large (30.6% of total composition), which initially seems incongruent with our claim of having a graphene nanomaterial, which should have consisted of purely sp^2-hybridized C. However, noting that XPS is a surface sensitive technique,[169] we attribute the measured sp^3 signals to the edge structure of the GNSPs and N-GNSPs exposed due to the vertical growth, *i.e.*, the sp^3 signal is artificially high because the edges are more exposed than the basal plane. Additionally, the N-GNSPs sample likely has a larger sp^3 component due to more sp^3 defects in the sample, as evidenced by a slightly wider *D* peak and larger *D′* peak in the Raman spectrum.

For the N-1*s* high resolution spectrum, we followed previously reported assignments and fit the data to a superposition of two peaks that corresponded to contributions from the pyridinic sites (399.5 eV) and pyrrolic sites (401.5 eV).[155] We found

that the pyridinic sites accounted for ~86% of the nitrogen content. This is an unprecedentedly large ratio of pyridinic type nitrogen doping sites, particularly considering the relatively narrow Raman peaks (**Figure 4.5F**) and a relatively high yield. In the case of the Cl-2*p* high resolution spectrum (**Figure 4.6F**), we considered the contributions of two components (with four peaks due to the $2p^{1/2}/2p^{3/2}$ splitting), which corresponded to C–Cl bonds (201.9/200.3 eV) and C–Cl_x bonds (197.2/196.1 eV).[170]

Electrochemical characterization. The fabricated graphene nanomaterials (both GNSPs and N-GNSPs) were tested for LIB anode application via galvanostatic charging/discharging (**Figure 4.7A ~ C**) and rate performance analysis (**Figure 4.7D**) by assembling with conductive additive and polymer binder in a coin cell configuration. These data resemble previously reported graphene LIB anode data in that the discharge capacity substantially decreased between the first and second cycles, the redox potentials varied substantially with the state of charge, and the capacity decreased with increasing charge/discharge rates.[148–154] For both GNSPs and N-GNSPs, SEI formation during the first cycle was apparent as a plateau at 800 ~ 700 mV, consistent with the report in literature.[171] After the first discharge, the charge/discharge curves (**Figure 4.7A** and **B**) nearly completely overlapped, indicating that the SEI entirely forms during the first discharge. The reversible capacities of the GNSP and N-GNSP anodes at 100 mA/g are ~373 mAh/g and ~423 mAh/g, respectively (**Figure 4.7A** and **B**), and both anodes returned to these values after cycling at high rates, suggesting minimal capacity fade (**Figure 4.7D**). At 100 mA/g the capacity of N-GNSPs was 13% higher than the capacity of GNSPs; the implications of this observation will be discussed in the *Discussion* section. To compare the voltage profiles of the GNSP and N-GNSP anodes, we plotted in **Figure**

4.7C the voltage as a function of anode state-of-charge (SOC). Both the charge and discharge profiles of N-GNSPs showed a higher redox potential than the undoped GNSPs for all SOC, suggesting that the pyridinic nitrogen had beneficial effects on the reduction kinetics and detrimental effects to the oxidation kinetics.

Additionally, to compare the electrochemically active surface areas of GNSPs and N-GNSPs, we estimated the double layer capacitance (which is linearly proportional to the active surface area) based on the galvanostatic charge/discharge curves, as detailed in *Note 4* and **Figure 4.8**. The estimated double layer capacitance of GNSPs and N-GNSPs is 5.6 F/g and 10.8 F/g, respectively, suggesting that N-GNSPs have a significantly higher surface

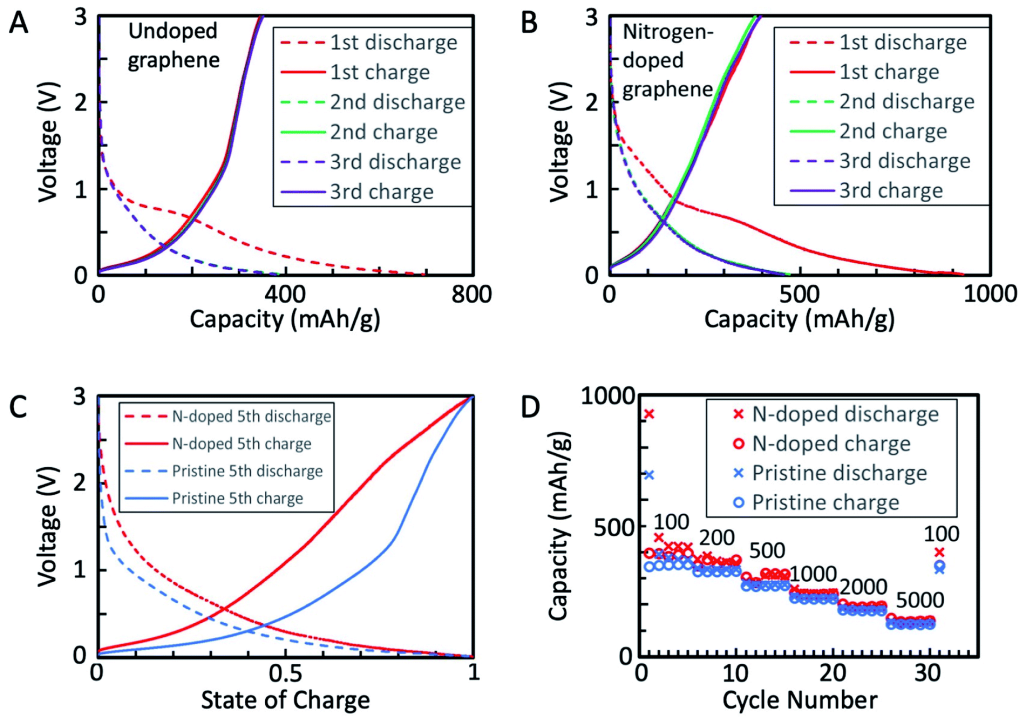

Figure 4.7. (A) First three cycles of galvanostatic charge/discharge for GNSP anode. Rate: 100 mA/g. Note: the second discharge is eclipsed by the third discharge. (B) First three cycles of galvanostatic charge/discharge for N-GNSP anode. Rate: 100 mA/g. Note: the second discharge is eclipsed by the third discharge. (C) Galvanostatic charge/discharge of the fifth cycle of both the GNSP and N-GNSP anodes normalized by state-of-charge. Rate: 100 mA/g. (D) Rate performance of GNSPs and N-GNSPs with the rate of each cycle (in mA/g) indicated above the data. All voltages are referenced to Li/Li^+.

area than GNSPs per unit mass, which is consistent with the perforations of N-GNSPs as imaged in **Figure 4.5D**. While the double layer capacitance for the N-GNSPs electrode is nearly twice of the capacitance of the undoped GNSPs electrode, the lithium storage capacitance of the N-GNSPs electrode is only 14% higher than the GNSPs electrode. This discrepancy suggests that although the double layer capacitance and the lithium storage capacitance follow the same trend between these two materials, they are not necessarily related. That is, the lithium storage capacitance is due to faradaic charge storage rather than non-faradaic charge storage.

Note 4. According to the widely accepted Electrochemical Methods by Bard and Faulkner,[29] double layer capacitance can be estimated from the slope of the voltage-*vs*.-time response due to a current step. To appropriately perform this measurement, however, the electrochemical response must be due to non-faradaic (capacitive) processes rather than faradaic (redox) processes, which can be ensured by measuring the voltage vs time response shortly after the current step, as non-faradaic processes tend to be much faster than faradaic processes. Therefore, we used the first ten seconds of the first galvanostatic discharge of GNSPs and N-GNSPs to estimate their capacitances (shown in **Figure 4.8**). The fairly linear slopes indicate that the electrochemical response during this time is, in fact, dominated by non-faradaic processes, as faradaic processes tend to cause voltage plateaus in galvanostatic measurements. The capacitance is calculated according to

$$Capacitance = \frac{Current}{Slope}$$

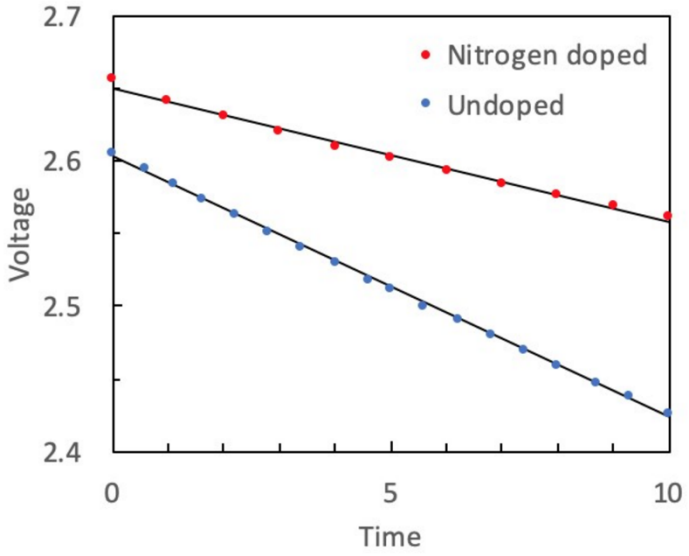

Figure 4.8. First ten seconds of GNSPs and N-GNSPs first galvanostatic discharge curve.

The respective slopes of the GNSPs and N-GNSPs discharge curves are -0.0093 V/s and -0.018 V/s, corresponding to capacitances of 5.6 F/g and 10.8 F/g.

Post mortem XPS characterization of N-GNSP LIB anode. To study the chemical changes that occur at dopant sites during the LIB operation, we performed XPS characterization on N-GNSP anodes after lithium cycling. For these experiments, samples were prepared without polymer binders and conductive additives to simplify data interpretation and to avoid contamination from polymers of the XPS ultrahigh vacuum environment. Rather, because our N-GNSP material grew directly on a copper foil, the as-grown sample with its copper substrate was assembled directly into a coin cell, as shown in the right panel of **Figure 4.4**. Three samples were prepared this way, each with an open-circuit voltage of ~3 V vs. Li/Li^+, and each sample was subjected to different conditions. The first, labelled "rest", was kept at open circuit for ~3 days. The second, labelled "800 mV", was cycled between 3 V (open-circuit voltage) and 800 mV five times, leaving the cell charged at 3 V. The third, labelled "10 mV", was cycled between 3 V (open-circuit

voltage) and 10 mV five times, leaving the cell charged at 3 V. Coin cells were cycled five times to ensure the relevant chemical processes proceeded to completion. Then, each coin cell was de-crimped in an argon-filled glovebox, rinsed with dimethyl carbonate, and dried in a vacuum chamber without being exposed to air. The samples were subsequently transferred to an argon-filled air-tight suitcase directly to the XPS load lock chamber. In addition, the top layers of sample "10 mV" were removed by gently scraping the sample with a spatula in the glovebox to reduce interference from the SEI. In addition, because these samples were very porous (see **Figure 4.5**), the electrolyte salt was not effectively removed from the surface even after rinsing the samples with dimethyl carbonate. The resulting XPS spectra displayed a strong signal from the salt and a weak (and noisy) signal from the graphene material. Therefore, we smoothed the data using boxcar averaging with a width of eleven points. This width was justified as the step size was 0.025 eV, so a width of eleven points was 0.25 eV, which was much smaller than the width of the XPS peaks (see **Figure 4.9**).

XPS analysis of these samples revealed that the nitrogen sites (**Figure 4.9A**) became chemically altered during cycling. We attribute the peak at ~402.1 eV to lithiation of the nitrogen sites (*e.g.*, N–Li^+) and the peak at 404.4 eV to solvent decomposition that resulted in either oxygen functionalization (N–O) or carbonation (N–CO2–R) of the nitrogen sites. These assignments may be justified as follows. Given the composition of the battery cell contents, the only possible chemical functionalization would involve carbon, lithium, oxygen, phosphorus, and fluorine. We can rule out phosphorus and

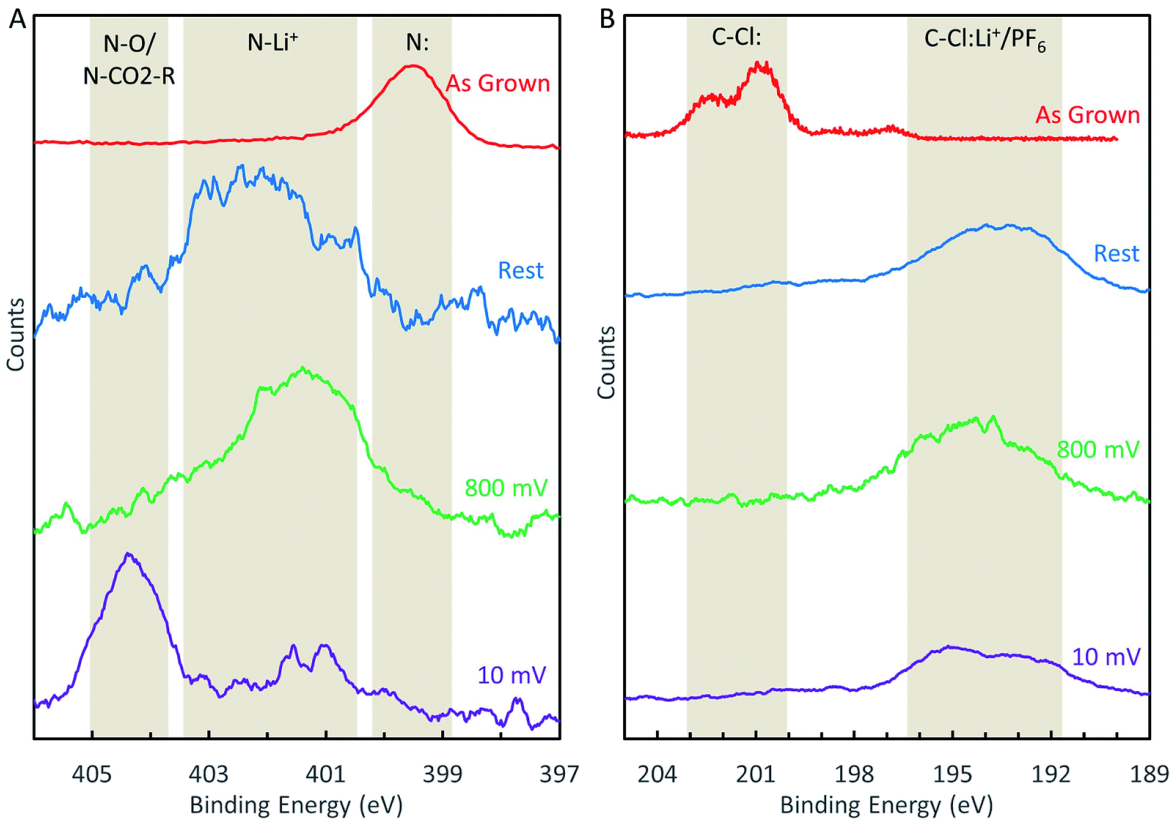

Figure 4.9. (A) Evolution of the N-1*s* XPS peak during LIB cycling. (B) Evolution of the Cl-2*p* XPS peak during LIB cycling.

fluorine functionalization because the N-1*s* binding energies for N–P and N–F bonds were reported in the range 397.3 eV to 400.3 eV and 417.1 eV, respectively, according to the XPS database of National Institute of Standards and Technology (NIST),[172] which differed from our measured peak positions. Therefore, the peak shifts after lithium cycling were likely due to lithiation and carbon/oxygen interactions. We assign N–Li^+ (lithiation) and N–O/N–CO2–R (solvent decomposition) to the peaks at 402.1 eV and 404.4 eV, respectively, because solvent decomposition reactions on nitrogen sites likely occurred during the SEI formation (which was, in fact, solvent and salt decomposition[171]), but the solvent decomposition peak could only appear after the electrode was cycled to potentials beyond the SEI formation potential.

The chlorine 2*p* peak also shifted in the samples assembled into battery cells after lithium cycling (**Figure 4.9B**). However, the peak shifted to a lower binding energy and becomes convoluted with the phosphorus 2*s* peak, the latter resulted from the $LiPF_6$ salt physisorbed to the surface. Therefore, detailed analysis of the chlorine 2p peak was difficult, although it is reasonable to assign the peak to Cl–Li^+ bond,[172] and some forms of solvent decomposition also cannot be ruled out.

Given the aforementioned peak assignments, we may describe the evolution of the nitrogen sites during the LIB charging/discharging cycles as follows. Even in the absence of any applied bias, nitrogen sites will bind Li^+ once assembled in a battery, as illustrated by the "rest" spectrum in **Figure 4.9A**. This N–Li^+ interaction persists when the battery is cycled between 3 V and 0.8 V, as shown by the "800 mV" spectrum in **Figure 4.9A**. If the battery is cycled below 800 mV, nitrogen sites become irreversibly functionalized due to solvent decomposition, as demonstrated by the "10 mV" spectrum in **Figure 4.9A**. We believe that these findings can serve as useful input for computation studies of LIB anode reaction mechanisms, which have not yet considered different chemical shifts of electrode components under different reactions.[158]

Discussion

Our experimental results suggest that selectively pyridinic-type nitrogen-doped graphene nanomaterials do not significantly increase the capacity of graphene nanomaterials. We also suggest that this lack of capacity enhancement is not due to the chlorine dopants as chlorine doping has also been demonstrated to increase the capacity of graphene nanomaterials, *i.e.*, chlorine does not have a deleterious effect on lithium storage

capacity.[152] To understand the origin of improved LIB performance previously reported for pyridinic-type nitrogen-doped graphene materials, we provide in **Table 4.2** a brief summary of the characterization and performance of doped graphitic materials reported in several studies.

For instance, the material used in study 1 of **Table 4.2** has fairly broad *D* and *G* peaks in the Raman spectra, contains significant amounts of other dopants, has a large surface area, and demonstrates a moderately high reversible capacity of ~1000 mAh/g. Study 2 reports a colossally high reversible capacity of 3525 mAh/g, and the nitrogen-doped graphene in this study displays a Raman spectrum with *D* and *G* peaks so broad that they overlap (suggesting strong disorder), has a large surface area, and contains additional sulfur and oxygen dopants. On the other hand, the materials in studies 4 and 5 demonstrate smaller reversible capacities and display moderately broad peaks in the Raman spectra, smaller surface areas, and fewer dopants than the materials in studies 1, 2 and 3. Our work

Study	% nitrogen (% pyridinic)	Other dopants	Raman spectra peaks FWHM (cm^{-1})	Surface area ($m^2\ g^{-1}$)	Reversible capacity (mA h g^{-1})
1	1.5 (33)	15% S 14% O 1% H	D peak: 130 G peak: 140	624	1110
2	1.8 (25)	6% S 5.2% O	D and G peaks are convoluted	906	3525
3	2 (57)	O[a]	D peak: 80 G peak: 70	[a]	900
4	3.1 (65)	3.1% O	D peak: 110 G peak: 80	290	500
5	0 (0)	1.8% P 3.25% O	D peak: 100 G peak: 70	[a]	450
6	7.5 (87)	3.1% Cl	D peak: 65 G peak: 76		423

[a] Authors did not specify the amount.

Table 4.2. Brief comparision of reported reversible capacities, doping and Raman spectra profiles of several studies of graphene LIB anodes.

(study 6 in **Table 4.2**) displays the narrowest Raman peaks, purest nitrogen-doping, and the smallest reversible capacity.

While the comparison in **Table 4.2** is by no means exhaustive, it reveals a trend that better performing doped graphene materials generally contain significant crystalline disorder (as demonstrated by the broad peaks in their Raman spectra) and have larger surface areas. Additionally, graphene materials containing multiple dopants appear to perform better, although this trend cannot be well established based on the limited comparison in **Table 4.2**. On the other hand, researchers have recently substantiated that incorporating multiple dopants in graphene nanomaterials can improve the electrocatalytic effect through the synergism among different heteroatoms or nitrogen sites.[173–175] Such synergetic effects may also take place in the case of LIB applications, although there are insufficient experimental data to draw this conclusion at present.

The phenomenon of high capacity in disordered carbon materials has been studied for decades, and several models have been proposed to explain it (*e.g.*, see Section 2.3.3 in ref.[35]). While many recent studies have focused on incorporating dopants to enhance lithium storage, it is possible that the dopants themselves have little effect on the lithium storage capacity. Rather, structural disorder that is coincident with doping may be the essential factor affecting the lithium storage capacity.

Conclusion

We have demonstrated a novel method of synthesizing nitrogen-doped graphene nanostripes with an unprecedentedly high percentage of pyridinic-type doping (>86% of the nitrogen sites) and good crystallinity, performed studies of such selectively pyridinic

type nitrogen-doped graphene as LIB anode materials, and provided experimental evidences for changes in the chemical state of nitrogen sites during LIB operation for the first time via XPS studies as a function of the cycling voltage. Our findings reveal that pyridinic-type nitrogen-doping alone does not significantly enhance the LIB anode performance when compared to an undoped graphene sample, suggesting that pyridinic sites may not be responsible for the enhanced performance of nitrogen-doped graphene materials observed in previous studies. We hypothesize that strong crystalline disorder, high surface area, and possibly multiple types of dopants in the LIB anode material may be important to increasing the reversible capacity. Additionally, post mortem XPS characterization of the N-GNSP LIB anodes further reveals immediate lithiation of the nitrogen sites upon contact with lithium electrolyte and functionalization of nitrogen sites by solvent decomposition and coincident SEI formation. These findings thus provide useful insights into more intelligent design and mechanistic understanding of doped graphene anodes for better LIB performance.

Chapter 5—Fabrication of Group-IV Element Doped Graphene and Application in Lithium-Ion Batteries

Adapted from

> J. D. Bagley, N.-C. Yeh, Group IV element (silicon, germanium and tin)-doped graphene application in lithium-ion battery anode and deconvolution of effects of doping and disorder performance. *Submitted*.

Personal contribution: Conceived the synthesis procedure, fabricated materials, performed characterizations, and participated in writing the manuscript.

Introduction

A major challenge to further commercial penetration of rechargeable batteries as an essential component to the future of renewable energy is insufficient energy density.[176] One of the many research efforts striving to solve this problem[20] is improving the energy density of the lithium-ion battery (LIB) anode. Graphite is the standard LIB anode material, but the practical performance of graphite has approached to its theoretical lithium storage capacity of 372 mAh/g that corresponds to a stoichiometry of LiC_6).[35] Therefore, next-generation LIB anode materials are being explored to further increase the storage capacity.[20]

A class of material being explored for LIB anodes is heteroatom doped graphene, i.e., graphene with a small fraction of carbon atoms substituted and/or functionalized by such elements as nitrogen, boron, phosphorus, oxygen, etc.[149–153] In particular, one such study has reported a reversible lithium storage capacity of 3525 mAh/g,[153] which is nearly ten times larger than graphite. Besides high lithium storage capacities, heteroatom doped graphene materials are appealing because their chemical similarity to graphite enables compatibility with current LIB assemblies.

The higher lithium storage capacity of doped graphene than graphite has been largely attributed to the higher affinity of dopant sites for lithium.[177] However, due to the difficulty of preparing doped graphene with good crystallinity, most doped graphene materials are disordered, and noting that disorder affects lithium storage capacity in carbon materials,[35] the contribution of doping to lithium storage capacity is not conclusive. Therefore, the correlation between dopants and the enhancement factors of lithium storage capacity has not been systematically investigated.

Separately, crystals of the group IV elements silicon (Si), germanium (Ge) and tin (Sn) are known to exhibit very high energy densities. The fully lithiated states of these Group IV elements correspond to capacities of 4200, 1625 and 994 mAh/g for Si, Ge and Sn, respectively. However, these materials have poor cycle life due to the extreme volume expansion during lithiation, which results in pulverization of anode particles and rupture of the solid electrolyte interface (SEI). Researchers have found that limiting the particle size of these group IV elements to less than ~ 150 nm can mitigate the problems associated with volume expansion.[178] Therefore, many efforts have been dedicated to reducing the particle size of the group IV elements, including using composites of silicon nanoparticles and carbon nanomaterials (*e.g.*, graphene and carbon nanotubes).[179,180]

The concept of reducing the size of the group IV element component can be extended beyond the nanoparticle regime to the atomic regime *via* atomically dispersed group IV element-doped graphene. Silicon-doped graphene has been fabricated by various methods in various configurations for a range of applications.[181–188] However, we are

unaware of any reports of application of Si-doped graphene in lithium-ion batteries or of fabrication of Ge- or Sn-doped graphene.

In this work, we report successful fabrication of Si-, Ge- and Sn-doped graphene nanostripes (GNSPs) and comparative studies of their performance as LIB anode materials. The Si-doped graphene nanostripes (Si-GNSPs) electrode demonstrated good crystallinity and enhanced performance (609 mAh/g) relative to undoped GNSPs, which deconvolved the effects of doping and disorder and unambiguously demonstrated the enhancement of Si-doping on lithium storage capacity. The Ge-doped graphene nanostripes (Ge-GNSPs) electrode and Sn-doped graphene nanostripes (Sn-GNSPs) electrode, on the other hand, exhibited strong disorder and lower capacities of 251 and 204 mAh/g, respectively. Comparing the characterization of the anode materials in this study with previous studies, we conjecture that the impaired lithium storage capacity in Ge- and Sn-GNSPs is primarily due to structural disorder, similar to graphitizing (soft) carbon. Conversely, the enhanced capacity reported for many other doped graphene materials is in part due to structural disorder, similar to non-graphitizing (hard) carbon. Further comparison with other studies suggests that the dopants most beneficial for enhancing lithium storage capacity in graphene are third-row elements.

Experimental

Synthesis of graphene materials. GNSPs and doped GNSPs were by modifying the plasma enhanced chemical vapor deposition (PECVD) synthesis previously reported by Hsu *et al.*[128] A microwave induced hydrogen/methane plasma with traces of 1,2-dichlorobenzene (Alfa Aesar, 99%) yielded undoped GNSPs on copper substrates, and

adding tetraethyl silane (TCI America, ≥ 97%), tetraethylgermanium (Alfa Aesar, 99%), or tetraethyltin (Alfa Aesar, 98%) yielded Si-GNSPs, Ge-GNSPs, and Sn-GNSPs, respectively. The PECVD growth system was custom built and consisted of eight parallel deposition chambers. The chambers were ½" outer diameter glass tubes containing 0.75 cm x 1.25 cm copper foils (McMaster-Carr, 99.9%) and were fitted with Evenson cavities (Opthos Instruments Inc., Frederick, MD, USA) excited by a 2.45 GHz microwave power source (ENS 4 x 200W CPS, Sairem, Décines-Charpieu, France). All chambers simultaneously received 70 W of microwave power, which created a plasma volume of ~ 1 cm^3. H_2 (Airgas, 99.999%) and CH_4 (Airgas, 99.999%) gases were introduced to the chamber by mass flow controllers (MC series, Alicat Scientific, Tuscon, AZ, USA), and 1,2-dichlorobenzene, tetraethyl silane, tetraethylgermanium, and tetraethyltin were introduced to the chamber by leak valves. The pressure in the chamber before splitting into eight chambers was held at 3.8 Torr, the total flow rates of H_2 and CH_4 were 48 sccm and 5 sccm, respectively. A residual gas analyzer (XT300M, Extorr Inc., New Kensington, PA, USA) was connected to the chamber via a capillary placed upstream of the deposition chamber and measured concentrations of CH_4, 1,2-dichlorobenzene and tetraethyl silane. The concentration of 1,2-dichlorobenzene was set such that the signal of the M = 147 peak (1,2-dichlorobenzene) was half the signal of the M = 16 peak (methane). The concentration of tetraethyl silane was set such that the M = 88 peak (tetraethyl silane) was one-fourth the size of the M = 147 peak. Tetraethylgermanium and tetraethyltin could not be detected in the residual gas analyzer even though their masses are within the range of the analyzer, presumably because they broke down in the analyzer and the fragment masses were convoluted with other analytes. For schematic of the growth system, see our previous

publication.[44] The plasma was maintained for ~ 3 hours growing graphene materials at a rate of ~ 6 mg/cm^2-hr per chamber.

Characterization of fabricated graphene materials. Scanning electron microscopy (SEM) was performed in a Hitachi S-4100 (Hitachi, Tokyo, Japan) with an accelerating voltage of 5 kV. Raman spectroscopy was performed in a Renishaw M-1000 Micro-Raman (Renishaw, Gloucestershire, UK) spectrometer operating with a 514.5 nm argon ion laser with a spectral resolution of 1 cm^{-1} and a spot size of ~ 20 μm. A dual-wedge polarization scrambler was inserted to depolarize the laser. Data were analyzed and fit in the Renishaw software, and peaks were fit to Lorentzian line shapes. X-ray diffraction (XRD) data were collected in a PANalytical X'Pert Pro X-ray powder diffractometer using the Cu Kα1 line (λ = 1.5406 Å) with a tube voltage and current of 40 kV and 20 mA, respectively. The XRD data were fit with a custom made fitting procedure. The backgrounds was fit to a high order polynomial, and the peaks were fit to an asymmetric Lorentzian. X-ray photoelectron spectroscopy (XPS) data were collected using a Surface Science Instruments M-Probe ESCA controlled by Hawk Data Collection software (Service Physics, Bend OR; V7.04.04). The monochromatic x-ray source was the Al K α line at 1486.6 eV, directed at 35° to the sample surface (55° off normal). Emitted photoelectrons were collected at an angle of 90° with respect to the sample surface (0° off normal) by a hemispherical analyzer. The angle between the electron collection lens and X-ray source was 35°. Low-resolution survey spectra were acquired between binding energies of 1-1000 eV. Higher-resolution detailed scans, with a resolution of ~ 0.65 eV, were collected on individual XPS lines of interest. The sample chamber was maintained at < 2 x 10^{-9} Torr. The XPS data were

analyzed using the CasaXPS software (CASA Software Ltd.). The peak area and uncertainties were computed by the CasaXPS software.

Coin cell preparation. Working electrodes, which consisted of graphene material (GNSPs, Si-GNSPs, Ge-GNSPs, or Sn-GNSPs), carbon black (Super-P, Alfa Aesar, >99%) and polyvinylidene fluoride (PVDF, MTI Corporation, ≥99.5%) binder in a 7:2:1 ratio, were mixed in N-methyl-2-pyrrolidinone (NMP, Sigma-Aldrich, 99.5%) in a centrifugal mixer (AR-100 Thinky U.S.A., Inc., Laguna Hills, CA, USA) at 5000 rpm for 10 minutes. The resulting slurry was spread across copper foil (McMaster-Carr, 99.9%) using a razor blade with the thickness controlled by tape on either side of the slurry (~ 0.2" thick) and dried at 120 °C in vacuum for 16 hours. ~ 3/16" diameter circular electrodes were cut from the dried slurry/copper foil. Two-electrode 2032 coin cells (MTI) were assembled in an argon filled glove box (with O2 < 0.1 ppm and H2O < 0.1ppm). The counter/reference electrodes were lithium foil (Sigma Aldrich, 99.9%, 0.75 mm, mechanically cleansed immediately before cell assembly), and the electrolyte was 1 M $LiPF_6$ (Sigma Aldrich, ≥99.99%) in ethylene carbonate/dimethyl carbonate (1:1 mixture by volume, both Sigma Aldrich, ≥ 99%). Dimethyl carbonate was stored over molecular sieves (3 Å, Beantown Chemical) prior to use, and the electrolyte was mixed in a dried HDPE bottle. A polypropylene separator (Celgard 2400) was used and ~ 8 drops of electrolyte were used in each coin cell.

Coin cell characterization. Galvanostatic charge-discharge measurements were performed on a Squidstat Prime (Admiral Instruments, Tempe, AZ, USA) at indicated current densities within a voltage range of 3 ~ 0.01 V.

Results

Si-, Ge-, and Sn-GNSPs synthesis rational. We accomplished the synthesis of Si-, Ge-, and Sn-GNSPs by modifying our previous synthesis of GNSPs,[44,128] where trace content of 1,2-dichlorobenzene in a hydrogen/methane plasma resulted in growth of high quality (in terms of the chemical purity and crystallinity) vertically oriented graphene on a copper substrate. Vertically oriented graphene refers to a class of graphene nanomaterials wherein graphene grows vertically with respect to the growth substrate forming wall-like nanostructures on the substrate.[45] We believe that in the synthesis of GNSPs, 1,2-dichlorobenzene forms benzene radicals in the plasma due to the relatively weak C-Cl bonds,[103] which then seed and propagate the graphene structure along with methane radicals assisting the growth and hydrogen radicals etching away defects. The role of methane and hydrogen was proposed by others studying the growth of vertically oriented graphene,[45] and the role of 1,2-dichlorobenzene is corroborated by our previous findings of the RGA data showing substantial increase in C_6 and C_6H_6 during the growth of GNSPs in the presence of 1,2-dichlorobenzene.[128] Tetraethyl silane, tetraethylgermanium and tetraethyltin similarly have weak bonds,[103] and we conjecture that these precursors form reactive silicon, germanium, and tin radicals in the plasma which incorporate into the graphene structure during growth.

Regarding the concentration of these precursors in the growth chamber and the concentration of dopants in the graphene material, we provide the following note. Neither tetraethyl germanium nor tetraethyl tin were detectable in our RGA mass spectrometer system (perhaps due to their low concentration, instability, and/or convolution with other species in the system). Thus, our only control on their concentration in the deposition

chamber was the degree which the leak valve was open, but the degree of opening the leak valve had little effect on the concentration of dopants in the fabricated graphene material, *i.e.*, whether the leak valve was marginally open or fully open the concentration of germanium (tin) in Ge-GNSPs (Sn-GNSPs) was about 1.5% (0.3%).

Separately, tetraethyl silane was easily detectable in the RGA system, and the dependence of silicon concentration in Si-GNSPs on the concentration of tetraethyl silane during growth is given in **Table 5.1**. (We note that the first entry is with the leak valve marginally open, and the last entry is with the leak valve fully open, demonstrating that our system was not capable of producing a large range of tetraethyl silane concentrations.) The data in **Table 5.1** do not show any trend, but rather simply resemble noise around ~ 2%.

The lack of dependence of dopant concentration on precursor concentration suggests that these dopant concentrations may indicate some thermodynamic limit in their solubility in graphene (at least by this fabrication method).

Table 5.1. Dependence of silicon doping in Si-GNSPs on concentration of tetraethyl silane during growth

Ratio of tetraethyl silane to methane	Silicon doping (%)
0.48	2
0.71	2.4
0.75	1.6
0.77	2.6

GNSPs characterization. The characterization presented hereafter demonstrates that *i*) GNSPs and Si-GNSPs are graphene materials with relatively good crystalline order, while Ge-GNSPs and Sn-GNSPs are disordered graphene materials, and *ii*) the dopants in Si-GNSPs, Ge-GNSPs, and Sn-GNSPs are substitutionally doped, atomically dispersed and free of carbides (*i.e.*, carbon atoms around the dopants maintain sp^2 hybridization rather than sp^3 hybridization). We acknowledge that silicon and especially germanium and tin are much larger than carbon, and doping these elements into the graphene structure may induce strain on the graphene lattice. Indeed, computational studies predict that these elements reside outside of the plane,[189,190] and our XRD data (see below) support this prediction. Other computational studies model an alternative scenario of the dopant replacing two carbon atoms instead of one such that the dopant resides closer to, but still not within, the graphene plane. Our characterization techniques employed in this investigation cannot resolve whether the dopants replace a single carbon atom or multiple carbon atoms.

Representative normal incidence SEM images of undoped and doped GNSPs materials on the copper growth substrates is shown in **Figure 5.1**. The SEM image of undoped GNSPs (**Figure 5.1a**) shows the tops of wall-like structures that are randomly oriented and connect and branch away from each other. Previous studies show that GNSPs fabricated with this method can be exfoliated to yield graphene materials with high aspect ratios (*e.g.*, 400 nm wide x 70 μm long),[128] suggesting that, although the wall-like segments only extend 1 ~ 3 μm before connecting with other segments, individual GNSPs extend far beyond single wall-like segments. The SEM image of Si-doped GNSPs (**Figure 5.1b**) appears similar to undoped GNSPs. The Ge-doped (**Figure 5.1c**) and Sn-doped (**Figure**

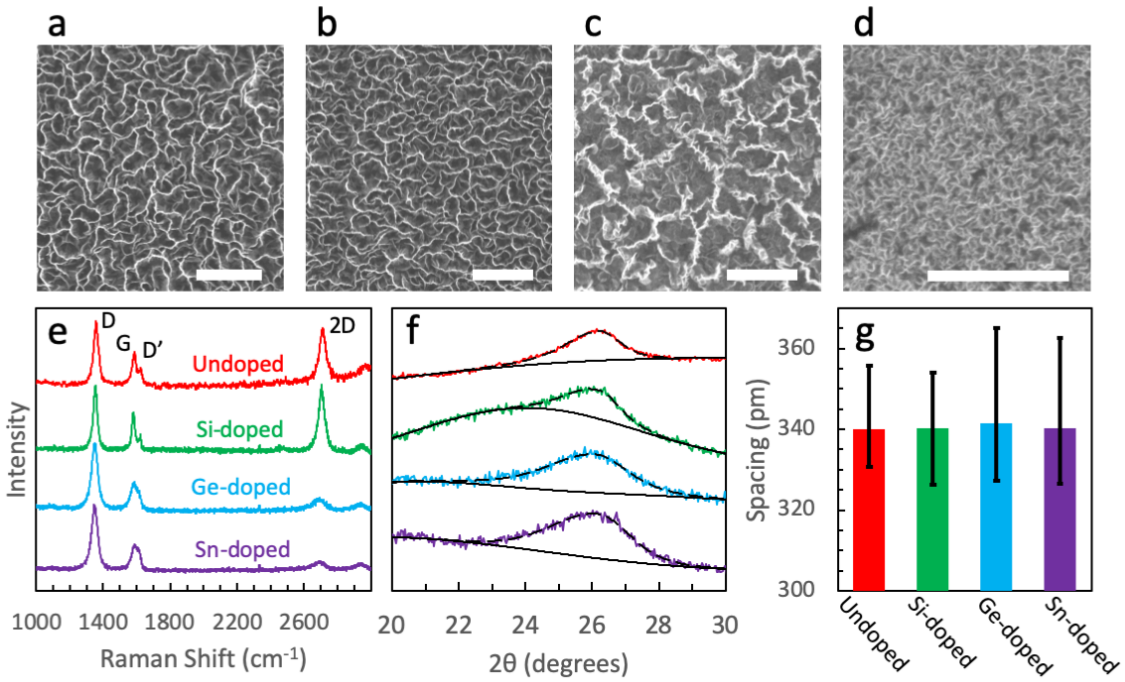

Figure 5.1. Normal incidence SEM images of undoped (**a**), Si-doped (**b**), Ge-doped (**c**) and Sn-doped (**d**) GNSPs. All scale bars: 5 µm (**e)** Raman spectra of undoped and doped GNSPs. **(f)** XRD patterns of GNSPs materials. **(f)** Mode and FWHM of GNSPs interlayer spacings extracted form XRD patterns.

5.1d) GNSPs, on the other hand, appear quite different from undoped GNSPs in that the wall-like segments are shorter and more jagged. This may be due to excessive defects in the Ge- and Sn-doped GNSPs, as evidenced by the Raman and XPS spectra discussed below.

Raman spectra of undoped and doped GNSPs are given in Fig. 1e and confirm the growth of graphene with the characteristic *D* (~ 1360 cm^{-1}), *G* (~ 1590 cm^{-1}) and 2*D* (~ 2704 cm^{-1}) peaks.[88] These materials also exhibit presence of the *D'* peak (~ 1620 cm^{-1}).[88] To quantitatively assess the spectral quality of these materials, the full-widths at half maximum (FWHM) of the *D*, *G* and 2*D* peaks and the intensity ratios of the *D* to *G* peaks (I_D/I_G) and the *D* to *D'* peaks ($I_D/I_{D'}$) are provided in **Table 5.2**. For undoped GNSPs and

Table 5.2. Fit parameters of Raman spectra.

	D peak FWHM (cm^{-1})	*G* peak FWHM (cm^{-1})	*2D* peak FWHM (cm^{-1})	I_D/I_G	$I_D/I_{D'}$
Undoped	35	30	47	2.0	5.5
Si-doped	29	21	46	1.7	6.2
Ge-doped	46	54	117	2.6	9.5
Sn-doped	45	52	115	2.7	8.9

Si-GNSPs, the *D*, *G*, and 2*D* peak widths are relatively narrow, and the I_D/I_G ratios (inversely proportional to the crystalline size) are relatively small as compared to those of Ge-GNSPs and Sn-GNSPs. These spectral characteristics suggest that undoped GNSPs and Si-GNSPs contain fewer defects than Ge-GNSPs and Sn-GNSPs.[130]

The $I_D/I_{D'}$ ratio can indicate the type of defects present in a graphene sample, with $I_D/I_{D'}$ ratios of ~ 3.5, ~ 7, ~ 10.5 and ~ 13 indicating boundary-type defects, vacancy-type defects, hopping (Stone-Wales) type defects and sp^3-type defects, respectively.[191] The respective $I_D/I_{D'}$ ratios of 5.5 and 6.2 in GNSPs and Si-GNSPs indicate a mixture of boundary-type and vacancy-type defects in these materials, and the respective $I_D/I_{D'}$ ratios of 9.5 and 8.9 in Ge-doped and Sn-doped GNSPs indicate a mixture of vacancy- and hopping-type defects. The transition to hopping type defects in Ge- and Sn-doped GNSPs may be due to the large sizes of Ge and Sn such that their doping causes significant dislocations in the graphene structure.

The XRD patterns near the (002) peak (indicating the grpahene interlayer spacing) of undoped and doped GNSPs are given in **Figure 5.1f**. Close inspection of the spectra reveals that the peaks are asymmetric; the tail to lower 2θ is larger than that to higher 2θ, with the asymmetry more dramatic for Ge-GNSPs and Sn-GNSPs. To quantitatively understand the spacings present in the materials, we fit the spectral background and peak (with all fits demonstrating an Abbe Criterion of at least 0.8), and **Figure 5.1g** displays the

resulting mode and FWHM (shown as error bars). Interestingly, the mode (the most frequent value) of the spacing of each material is about the same (~ 340 pm), but the FWHM differs, with the FWHM of Ge-GNSPs and Sn-GNSPs being much larger (especially towards larger spacing or lower 2θ) than the FWHM of GNSPs and Si-GNSPs. The larger spacings observed in Ge-GNSPs and Sn-GNSPs are evidence of the dopant protruding out of the plane. On the other hand, the same mode of spacing for all materials may be attributed to the low concentration of dopants (less than 3%) such that their overall effect on the interlayer spacing is only manifested in the asymmetric broadening of FWHM rather than the average spacing throughout the material.

Complimentary to the Raman spectroscopy data (**Figure 5.1e**, revealing the relative crystallinity and defect content of each sample) and to the XRD data (**Figure 5.1f**, revealing structural characteristics), we provide XPS data (**Figure 5.2**) to reveal the chemical composition, corroborate the relative defect contents, and demonstrate the chemical state of carbon atoms around the dopants. The survey spectra (**Figure 5.2a**) show that the undoped GNSPs are pure carbon, whereas the doped GNSPs contain the target dopant, oxygen, and chlorine as well as carbon. To quantitatively determine the chemical composition of each material we conducted high resolution scans of the carbon 1*s* peak, oxygen 1*s* peak, chlorine 2*p* peak, and an appropriate peak of the target dopant (silicon 2*p*, germanium 3*p* and tin 3*d*). The composition analysis including error estimates for all materials is provided in **Table 5.3**.

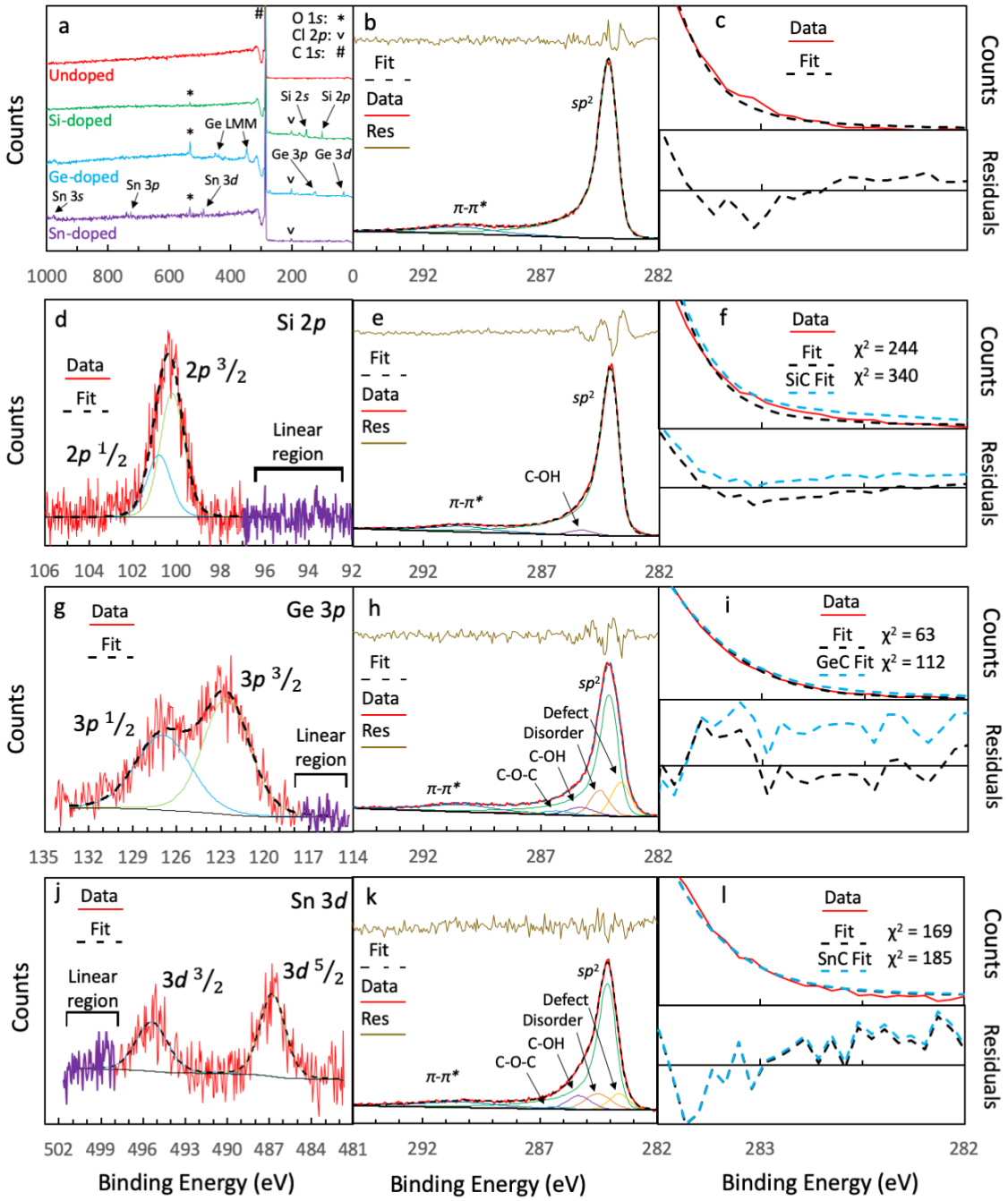

Figure 5.2. XPS survey spectra (**a**) of undoped and doped GNSPs. High resolution XPS scans of undoped GNSPs C 1*s* (**b**), Si-doped GNSPs Si 2*p* (**d**) and C 1*s* (**e**), Ge-doped GNSPs Ge 3*p* (**g**) and C 1*s* (**h**), and Sn-doped GNSPs Sn 3*d* (**j**) and C 1*s* (**k**). Fits of models with and without carbide components and their residuals for GNSPs C 1*s* (**c**), Si-GNSPs C 1*s* (**f**), Ge-GNSPs C 1*s* (**i**), and Sn-GNSPs C 1*s* (**l**).

In order to further verify the relative defect contents and demonstrate that the materials are free of carbides, we quantitatively analyzed the high resolution carbon 1*s*

Table 5.3. Undoped and doped GNSPs compositional analysis according to XPS fittings. Standard deviations of composition are given in parentheses.

	% Carbon	% Oxygen	% Chlorine	% Target dopant	C peak % sp^2
GNSPs	100 (0)	0	0	N/A	87
Si-GNSPs	96 (3)	0.8 (0.8)	0.9 (0.3)	2.0 (0.4)	87
Ge-GNSPs	93 (5)	4 (2)	1.7 (0.5)	1.5 (0.3)	58
Sn-GNSPs	97 (4)	2 (1)	0.6 (0.4)	0.3 (0.2)	64

peak of each sample. We fit undoped GNSPs carbon 1*s* peak (**Figure 5.2b**) with two components corresponding to sp^2 hybridized C-C bonds (284.1 eV) and a π-π* shake-up (290.5 eV) with a Tougaard background. The sp^2 peak was fit to an asymmetric Finite Lorentzian line shape[134–136] and the π-π* shake-up peak was fit to a symmetric Gaussian-Lorentzian. We did not impose any fitting constraints on this spectrum, but the parameters demonstrate that the fit is realistic. That is, the sp^2 asymmetry parameter (0.18), the sp^2 FWHM (0.87 eV) and the relative positions of the sp^2 and π-π* shake-up peaks (284.1 eV and 290.5 eV, a peak separation of 6.4 eV) are all consistent with previous reports.[132,133,137]

To ensure that the fitting parameters are relevant, we performed uniqueness tests on the sp^2 peak area and the FWHM, wherein a 10% change in area resulted in a 160% increase in χ^2, and a 10% change in FWHM resulted in a 130% increase in χ^2, demonstrating that the sp^2 peak parameters are relevant. Here we note that uniqueness testing involves systematically constraining a single parameter at various values while allowing the other parameters to float. If a change in the constrained parameter results in a significant increase in the fit error, then the parameter is considered relevant in the model. Further, a parameter is considered "unique" if a 10% change in that parameter results in at least a 10% increase in χ^2.[192] Finally, to ensure that the model included all the appropriate components, we added many other components that are typically included in carbon 1*s*

peak models (*e.g.*, peaks for defects, disorder, C-OH, C-O-C, C=O and O-C=O at positions 0.4 eV lower, 0.5 eV higher, 1.3 eV higher, 2.3 eV higher, 3.6 eV higher, and 4.7 eV higher binding energies than the sp^2 component[133,134] with the FWHM of the defect and disorder peaks constrained to 0.5 ~ 1.3 eV[133] and the FWHM of the other peaks constrained to 1.2 ~ 1.4 eV[134]), but the fitting procedure reduced these peaks to zero area, demonstrating that these species are not present in significant quantities in the sample. Further analysis of the residuals spectrum in this figure also indicated that there was no need for additional peaks. Altogether, the fitting of XPS data demonstrates that the undoped GNSPs carbon 1*s* spectrum is well described by a sp^2 component and a π-π* shake-up component.

The doped GNSPs carbon 1*s* spectra are more complicated (**Figures 5.2e**, **5.2h** and **5.2k**), but the aforementioned analysis of the undoped GNSPs carbon 1*s* spectrum aided our analysis of the doped GNSPs spectra. In particular, for all doped GNSPs, we constrained the sp^2 component position, the FWHM of the sp^2 component, and the separation between the sp^2 and π-π* shake-up components to be the same as those of the undoped GNSPs. We justified these constraints as all the materials were analyzed in the same system under the same conditions. Additionally, all of the doped GNSPs peak models include the defect, disorder, C-OH, C-O-C, C=O and O-C=O components. In each case the fitting procedure minimized the C=O and O-C=O components to zero area, and for Si-GNSPs the fitting procedure minimized all components to zero except the sp^2, π-π* shake-up and C-OH components.

In each case, we found that the only unique parameter was the area of the sp^2 peak, whose 10% change in area resulted in 50%, 26% and 12% increase in χ^2 for Si-GNSPs,

Ge-GNSPs, and Sn-GNSPs, respectively. Thus, one may be concerned that the aforementioned peak fitting models were irrelevant because they contained only one unique parameter (*i.e.*, the area of the sp^2 peak). However, we emphasize that because the area of the sp^2 component is unique we could confidently report the concentration of the sp^2 components in the carbon 1*s* spectra, although we could not confidently report either the presence or the concentrations of the other components in the sample. Our confidence could be further underscored by our inclusion of a large number of components in the model, *i.e.*, additional components would generally reduce the uniqueness of a parameter by allowing a change in that parameter to be compensated by the large number of floating parameters and still result in a fit with low error. Therefore, our detailed analysis of the carbon 1*s* peaks revealed that the fraction of the sp^2 component was 87%, 87%, 58% and 64% for GNSPs, Si-GNSPs, Ge-GNSPs, and Sn-GNSPs, respectively (see **Table 5.3**). These values derived from XPS studies were consistent with the Raman spectroscopic analysis that revealed significantly fewer defects in GNSPs and Si-GNSPs than in Ge-GNSPs and Sn-GNSPs.

Further analysis of our carbon 1*s* spectra by comparing the quality of fits between models containing a carbide component and those without a carbide component also revealed that carbides were not present in our samples. Here the models that contained the carbide component were based on the model of no carbide plus an additional component with constrained FWHM, position and area. The FWHM was constrained to 0.8 ~ 2 eV, which was justifiable because 0.8 eV was the resolution of our spectrometer and the FWHM of carbide carbon 1*s* peaks was less than 2 eV according to literature.[193–195] The position was constrained to 1 eV lower binding energy than the sp^2 component for Si-

GNSPs, and to 1.1 eV lower binding energy for Ge-GNSPs and Sn-GNSPs, consistent with previous reports[193,195]—in the case of tin carbide, we were unable to find literature reports for corresponding XPS characterization, and so we assumed that its carbon 1*s* component position would be similar to germanium carbide. The areas were constrained by requiring their minimum to at least represent the ratio of dopant to carbon (see **Table 5.3**).

Using the aforementioned conditions, we obtained the peak fits with and without the carbide component in the range near the hypothetical location of the carbide component (282~283.5 eV), as shown in **Figures 5.2c**, **5.2f**, **5.2i** and **5.2l** along with their residuals. In these spectra, the models without the carbide component consistently appeared better, and the residuals spectra further confirmed this finding, showing similar errors as that of the GNSPs residual spectrum (**Figure 5.2c**). As a more rigorous comparison, we calculated the χ^2 of each model (displayed in the figures). The relative increase in χ^2 when the carbide component was included was 39%, 78% and 9% for Si-GNSPs, Ge-GNSPs, and Sn-GNSPs, respectively. We acknowledge that the increase in χ^2 for Sn-GNSPs was not particularly large, but this result was not surprising because the concentration of Sn was very small in Sn-GNSPs (see **Table 5.3**). Furthermore, the inclusion of many other additional components (*e.g.*, defects, disorder, C-OH, *etc.*) underscored the significance of these increases in χ^2, *i.e.*, additional fitting parameters should have enabled the fitting procedure to minimize the errors when the carbide component was included; the fact that the fitting procedure could not minimize the error strongly suggested that the carbide component did not belong in the model for these materials.

The high resolution scans of the target dopants peaks are presented in **Figures 5.2d**, **5.2g** and **5.2j** for Si-GNSPs, Ge-GNSPs, and Sn-GNSPs, respectively, where the components were labeled and a linear region used to evaluate the intrinsic noise *via* the Abbe criterion was indicated.[192] Here we remark that the Abbe criterion is a measure of the goodness-of-fit and ranges between 0 and 2. An Abbe criterion of 1 indicates a perfect Gaussian distribution of noise around a fit.

The spectra in **Figures 5.2d**, **5.2g** and **5.2j** demonstrated that the dopants were all present in a single bonding configuration and were likely atomically dispersed and bonded to carbon, as opposed to bonded to oxygen or chlorine. The Si 2*p* high resolution spectrum in **Figure 5.2d** was fit with two components that represented the $2p^{1/2}$ and $2p^{3/2}$ splitting. Following established procedures, we constrained the peak widths to be the same, the $2p^{1/2}$ component to be half of the $2p^{3/2}$ component and the $2p^{1/2}$ peak position to be 0.6 eV higher than the $2p^{3/2}$ peak position.[196] The fit resulted in an Abbe criterion of 0.87, compared to an Abbe criterion of 0.93 for the linear region. We conclude, therefore, that the peak splitting was due to $2p^{1/2}/2p^{3/2}$ splitting (rather than splitting due to multiple components) and that silicon existed in a single type of bonding environment. A single bonding environment necessarily implied that Si elements in Si-GNSPs were bonded to carbon because they were imbedded in a carbon matrix. Additionally, we note that silicon bonded to oxygen or chlorine would have a $2p^{3/2}$ peak position greater than 102 eV,[197] whereas the $2p^{3/2}$ peak position for our material was ~ 100.3 eV. Therefore, we conclude that the Si elements in Si-GNSPs were atomically dispersed and bonded to carbon.

The germanium 3*p* high resolution XPS spectrum is presented in **Figure 5.2g**, which we fit with two components represented the representing the $3p^{1/2}/3p^{3/2}$ splitting. Following the literature, we constrained the peak widths to be the same and the splitting to be 4 eV.[198] The fit resulted in an Abbe criterion of 0.89, compared to an Abbe criterion of 0.95 for the linear region. We therefore concluded that the two peaks were due to $3p^{1/2}/3p^{3/2}$ splitting, and that the spectrum conformed to germanium in a single bonding environment. Again, the single bonding environment implied that germanium elements were bonded to carbon. Further, the Ge $3p^{3/2}$ component position in our material was ~ 122.6 eV, consistent with germanium bonded to carbon rather than oxygen or chlorine, the latter would have resulted in a position of ~ 125 eV or ~ 124 eV, respectively.[199]

The tin 3*d* high resolution scan is presented in **Figure 5.2j**, which we fit with two components representing the $3d^{5/2}/3d^{3/2}$ splitting. We constrained the peak width to be the same and the peak splitting to 8.6 eV.[200] The fit resulted in an Abbe criterion of 0.99, compared to an Abbe criterion of 1.08 for the linear region. We therefore concluded that the two peaks were due to $3d^{5/2}/3d^{3/2}$ splitting, and the spectrum conformed to Sn in a single bonding environment. Again, the single bonding environment implied that Sn was bonded to carbon. However, the Sn $3d^{5/2}$ component position was ~ 486.8 eV, which did not quantitatively resolve the bonding environment of Sn as Sn-C, Sn-O and Sn-Cl because the reported binding energies in the respective ranges were 485.1 ~ 487.1 eV, 485.6 ~ 487.6 eV and 485.3 ~ 488.1 eV.[201] However, given that the Sn-GNSPs were fabricated by a similar method as Si-GNSPs and Ge-GNSPs, and that the target dopants of Si-GNSPs and Ge-GNSPs were bonded to carbon, we infer that the Sn elements in Sn-GNSPs were also bonded to carbon.

The aforementioned analysis of the positions and shapes of the high resolution spectra of target dopants (**Figures 5.2d**, **5.2g** and **5.2j**) suggested that the dopants were atomically dispersed and substitutionally doped into the graphene structure, and that they were neither in nanoparticle configurations or functionalized (*e.g.*, with oxygen and/or chlorine). This assertion is justifiable because nanoparticles anchored onto graphene would have contained at least two binding configurations of Si-Si and Si-C, whereas substitutional dopants would contain only one binding configuration of Si-C. Additionally, the chemical shifts for Si-GNSPs and Ge-GNSPs were inconsistent with dopant-oxygen or dopant-chlorine bonds, so that they must be dopant-carbon bonds. Additionally, the absence of nanoparticle signals in the Raman spectra (**Figure 5.3**) further indicate dopant nanoparticles do not exist in these materials.[202–205]

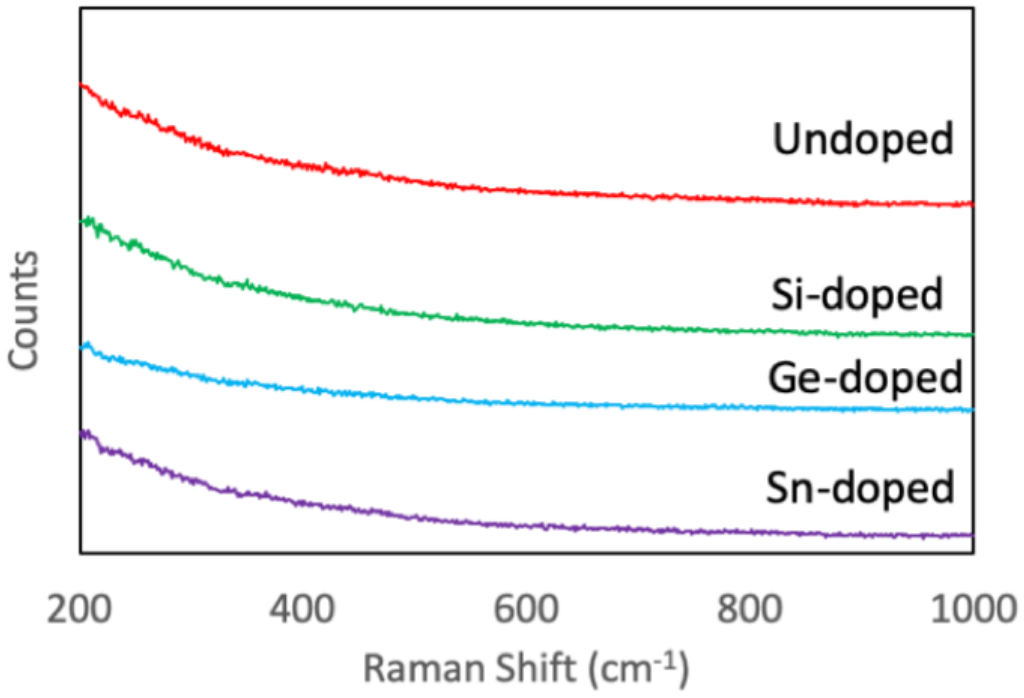

Figure 5.3. Low frequency Raman spectra of undoped and doped GNSPs.

GNSPs electrochemical characterization. GNSPs and doped GNSPs were tested as lithium-ion battery anodes by packaging them in a coin cell configuration using a lithium foil as the counter/reference electrode, and the electrochemical characterization results are summarized in **Figure 5.4**. The first three cycles of the galvanostatic charge-discharge for GNSPs, Si-GNSPs, Ge-GNSPs, and Sn-GNSPs electrodes are given in **Figure 5.4a**, **5.4b**, **5.4c** and **5.4d**, showing reversible capacities of 374 mAh/g, 609 mAh/g, 251 mAh/g, and 204 mAh/g, respectively. For each material, the formation of the solid-electrolyte interphase is apparent in the first discharge as a plateau at starting ~ 0.8 V for GNSPs, Si-GNSPs and Ge-GNSPs and ~ 0.5 V for Sn-GNSPs. The second and third cycles for each material are similar such that the third cycle eclipses the second cycle in **Figure 5.4**, indicating that the solid-electrolyte interphase completely forms during the first cycle. The redox potential for each material significantly changes with state-of-charge, as has been observed for other graphene LIB anodes.

The rate performance between 100 mA/g and 5000 mA/g is shown in **Figure 5.4e**. Similar to other graphene LIB anodes, the capacity decreases with increasing charge/discharge rate. It is interesting to note that GNSPs perform better than Si-GNSPs at a rate of 5000 mA/g even though Si-GNSPs have a much higher capacity than GNSPs at low charge/discharge rates. This may be due to kinetic limitations of lithiation at or near the silicon dopant sites. Because Si-GNSPs performed the best amongst these materials, we did a long term cycling test on Si-GNSPs at 1000 mAh/g, which is shown along with its coulombic efficiency in **Figure 5.4f**. The initial reversible capacity was ~ 311 mAh/g, and the final reversible capacity was ~ 207 mAh/g, which is 67% of the original capacity. The coulombic efficiency is nearly unity throughout the cycling.

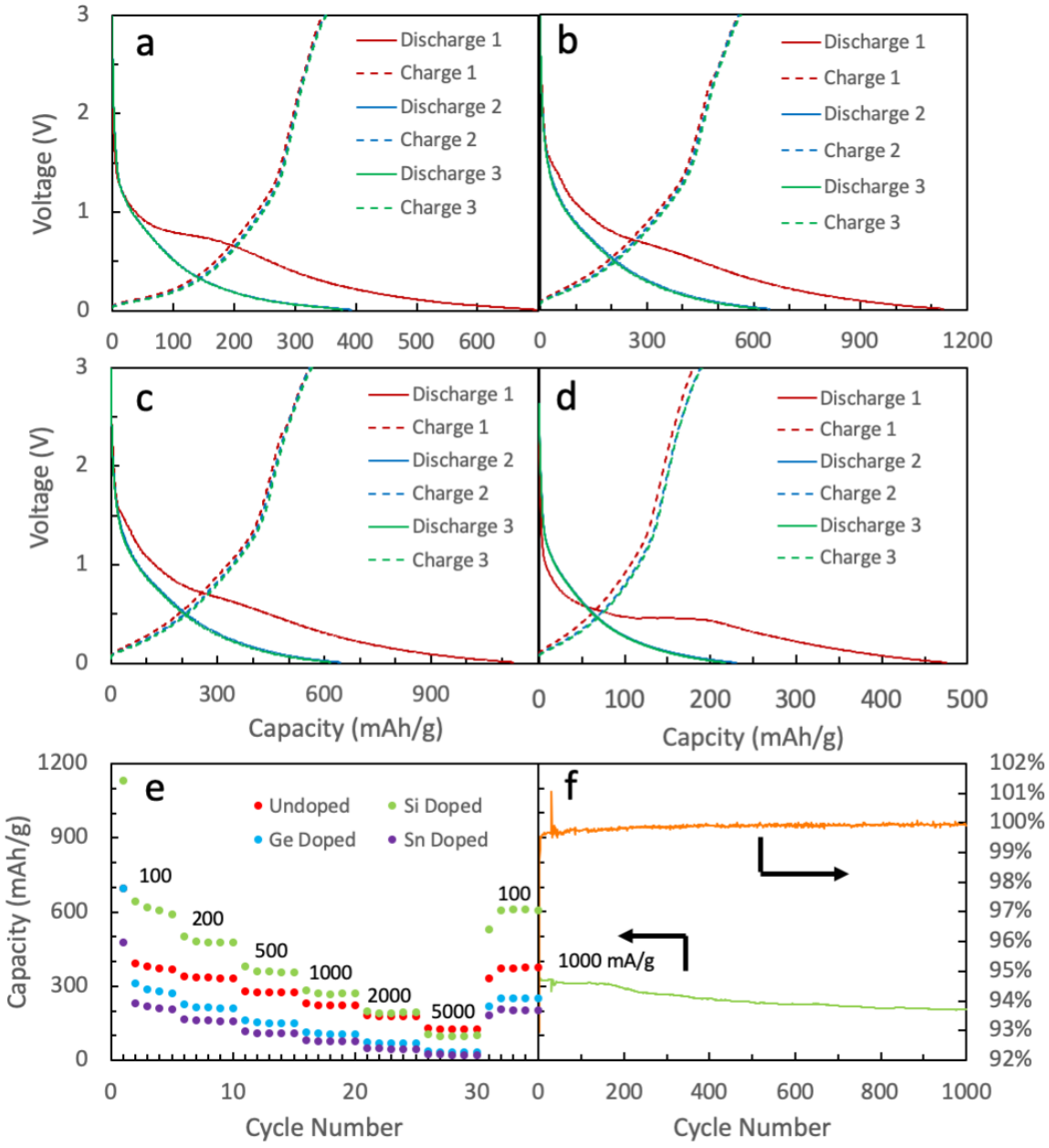

Figure 5.3. First three Galvanostatic discharge/charge cycles of GNSPs (**a**), Si-GNSPs (**b**), Ge-GNSPs (**c**) and Sn-GNSPs (**d**). The second charge and discharge cycles are eclipsed by the third charge and discharge cycles. (**e**) Rate performance of undoped and doped GNSPs. (**f**) Long term cycling performance of Si-GNSPs.

To infer whether double-layer capacitance significantly contributes to the measured capacity and to investigate whether the structure of the materials (*i.e.*, the interlayer spacing) changes significantly during lithium cycling (for example, due to solvated

intercalation[35]), we estimated the double-layer capacitance from the initial voltage-time response of the galvanostatic discharge curves, according to $C_{dl} = current/slope$ (see Bard and Faulkner[29]). The double-layer capacitance of the fresh electrodes and cycled electrodes are given in **Table 5.4** along with the projected charge storage capacity due to the double-layer capacitance. In all cases, the contribution of double-layer capacitance to the charge storage capacity was small: For the GNSPs, Si-GNSPs, Ge-GNSPs, and Sn-GNSPs electrodes, the respective contributions were 1%, 1%, 2% and 3% of the total reversible charge storage capacity. The double-layer capacitance also decreased after cycled (likely due to SEI formation on the surface) for each electrode except Sn-GNSPs. The increase in capacitance on Sn-GNSPs after cycled may be due to increased interlayer spacing from solvated intercalation[35] and may be related to the large size of tin atoms.

Discussion

The Si-GNSPs electrode has a significantly higher specific capacity than the undoped GNSPs electrode, while the Ge-GNSPs and Sn-GNSPs electrodes have significantly lower specific capacity than the undoped GNSPs electrodes. The deleterious effect of Ge- and Sn-doping initially seems peculiar since dopants generally improve the capacitance of graphene materials.[148–152,154,204] We consider two possible causes of their

Table 5.4. Double-layer capacitance and projected contribution of double-layer capacitance to charge storage capacity of initial and cycled electrodes.

	Initial electrodes		Cycled electrodes	
	C_d (F)	Capacity (mAh/g)	C_d (F)	Capacity (mAh/g)
GNSPs	5.5	4.6	5.1	4.2
Si-GNSPs	6.2	5.2	5.8	4.8
Ge-GNSPs	15.6	13.0	7.0	5.8
Sn-GNSPs	5.9	4.9	7.5	6.3

deleterious effect: *i*) electron doping due to the dopants, and *ii*) disorder in the crystal structure. Electron doping seems a plausible explanation for the deleterious effect as it would shift the Fermi level above the Dirac point in the electronic band structure[25] such that the sum of electronic states between the open circuit voltage (~ 3 V *vs.* Li/Li^+, also the Fermi level) and the final discharge voltage (~ 0.01 V *vs.* Li/Li^+) is lower than if the Fermi level is near the Dirac point. Indeed, computational studies predict the Fermi levels of germanium-doped graphene to be higher than graphene.[190,206] However, this conjecture is not consistent with the literature. For example, both boron doping and nitrogen doping (hole doping and electron doping, respectively) enhance the charge storage capacity of graphene.[150]

Alternatively, there is precedence in the literature that disorder in the structure of graphitic materials can strongly affect its charge storage capacity (both towards enhancement and impairment, depending on the type of disorder). It has been well established for decades that graphitizing (soft) disordered carbons have low lithium storage capacity, while non-graphitizing (hard) disordered carbons have high lithium storage capacity (see section *2.3.3* in reference[35]). Graphitizing carbons are carbon materials that become graphitic when heat treated (*e.g.*, at 3000 °C) and have a layered structure similar to graphite, but with very small crystallite domains; non-graphitizing carbons, on the other hand, retain their disorder when heat treated and have a porous structure with small crystallite domains that are skew with respect to each other.[207]

We attribute the poor performance of Ge-GNSPs and Sn-GNSPs to disorder resembling soft carbons. Although distinguishing between soft and hard carbons is not

trivial,[207] our Raman spectra (**Figure 5.1e**, **Table 5.2**) for Ge-GNSPs and Sn-GNSPs show wide peaks and high I_D/I_G ratios, and our XPS data (**Figure 5.2**) for Ge-GNSPs and Sn-GNSPs revealed high defect content. It is unclear whether maintaining good crystallinity is possible with Ge- and Sn-doping due to their much larger atomic sizes relative to carbon, at least we were unable to achieve good crystallinity for Ge- and Sn-doping with the PECVD synthesis method, as determined by Raman spectroscopy.

On the other hand, we were able to achieve good crystallinity and also observed enhanced lithium storage for Si-doping. Indeed, the Raman spectrum of Si-GNSPs revealed narrower peaks and a smaller I_D/I_G ratio than the Raman spectrum of GNSPs (**Figure 5.1e**, **Table 5.2**), suggesting Si-GNSPs have a low defect content compared to GNSPs. Since our undoped GNSPs demonstrated charge storage performance comparable to pristine graphite without being either enhanced or impaired by defects, we expect that the charge storage performance of Si-GNSPs would be similarly unaffected by defects so that the enhanced capacity of Si-GNSPs relative to GNSPs was primarily due to Si-doping.

Here we note that our finding of Si-doping-induced capacity enhancement addresses an understudied aspect in the field of doped graphene LIB anodes: although there are a plethora of studies regarding doped graphene LIB anodes, few studies have attempted to deconvolute the effects of disorder and doping. For example, in a previous report,[44] we studied lithium storage in highly crystalline nitrogen-doped GNSPs and observed only limited enhancement in capacity with doping. In contrast, doped graphene materials that exhibited high lithium storage capacity (*e.g.*, > 1000 mAh/g) were always accompanied by wide Raman peaks, suggesting that highly disordered graphene materials tend to result in

high lithium storage capacity.[44] Thus, we postulated in the previous study that doping itself may not be sufficient for enhanced lithium storage capacity, and disorder that coincided with doping may be critical for the enhancement.

The results of this study appear to inject new understanding of the roles of doping and disorder beyond our previous investigation of nitrogen-doped graphene.[44] Specifically, we note that in the absence of significant disorder, silicon doping results in substantial enhancement in lithium storage capacity while nitrogen doping has little effect. This difference may be attributed to the fact that silicon is a third-row element with additional electronic orbitals (*e.g.*, 3*d*) while nitrogen is a second-row element with a similar electronic structure as carbon. Therefore, silicon doping provides additional binding states for lithium binding resulting from the additional electronic orbitals available to silicon. This conjecture is corroborated by the observation that many of the highest capacity graphene materials are doped by third-row elements (*e.g.*, sulfur and phosphorus).[153,154] On the other hand, even larger atoms such as those in the fourth and fifth rows may lead to either graphitizing (soft) or non-graphitizing (hard) disordered carbons so that the net effect of doping on the lithium storage capacity will depend on the combined contributions of the excess electronic binding states for lithium and the type of disorder. Overall, our studies and comparison with other investigations to date suggest that proper choices of dopants in addition to non-graphitizing disordered carbons are important components to the enhancement of lithium storage capacity.

Conclusions

We have successfully fabricated atomically dispersed silicon-, germanium-, and tin-doped graphene nanostripes and compared their lithium storage performance with undoped graphene nanostripes. We observed a 63% enhancement for silicon-doped graphene nanostripes and a 33% and 45% impairment for germanium- and tin-doped graphene nanostripes, respectively. We conjecture that germanium and tin doping impairs capacity via graphitizing carbon-like disorder induced by their large sizes, and that silicon doping enhances capacity by creating additional electronic states for binding lithium. The good crystallinity of our silicon-doped graphene nanostripes suggests that the enhanced performance is strictly due to doping rather than disorder, which observation is made possible by deconvoluting the effects of disorder and doping. Further experiments deconvoluting the effects of doping and disorder will be beneficial to significantly advancing the lithium storage capacity of the anode material in lithium ion batteries.

Chapter 6—Conclusion

This thesis describes the development of novel methods to synthesize graphene and graphene derivatives as well as the application of these nanomaterials in select energy storage configurations. These graphene nanomaterials fabricated and studied here, both undoped and doped, are unique among most graphene studied in the literature in that they have large length-to-width aspect ratios, and that their production based on a single-step PECVD method without active heating is a scalable approach for producing large amounts of material with good crystallinity and chemical purity. The good crystallinity and chemical purity is especially rare for doped graphene materials available to date.

The large aspect ratios of GNSPs are particularly interesting for supercapacitor and percolating conductor applications. As studied in this thesis, the large aspect ratios appear to maintain electrode conductivity in *in situ* exfoliated GNSPs. Additionally, the large aspect ratios could be exploited as a conductive additive in electrically resistive electrode materials such as activated carbon and $LiFePO_4$, and for fabrication of transparent and/or flexible conductive electrodes, such as porous thin layers of deposited GNSPs that can be largely transparent and yet electrically connected.

By systematically investigating the effect of dopants in highly crystalline graphene, the results thus derived have provided new insights into the mechanisms of enhanced lithium storage in doped graphene materials. This new understanding is expected to help the advancement of high energy density lithium-ion batteries. Finally, although graphene LIB anodes have demonstrated extremely high lithium storage capacity, the Li^+ redox voltage is not favorable. Further studies of the mechanisms in graphene LIB anodes could

be informative for developing carbon anodes with both high lithium storage capacity and favorable Li^+ redox voltages, which would be a prudent focus of future research.

Bibliography

1. Summary for Policymakers — Global Warming of 1.5 °C. https://www.ipcc.ch/sr15/chapter/spm/.
2. Global Emissions. *Center for Climate and Energy Solutions* https://www.c2es.org/content/international-emissions/ (2020).
3. Dones, R., Heck, T. & Hirschberg, S. GREENHOUSE GAS EMISSIONS FROM ENERGY SYSTEMS: COMPARISON AND OVERVIEW. 14.
4. Statistical Review of World Energy | Energy economics | Home. *BP global* https://www.bp.com/en/global/corporate/energy-economics/statistical-review-of-world-energy.html.
5. GEA. *Global Energy Assessment - Toward a Sustainable Future*. (2012).
6. Tsao, J., Lewis, N. & Crabtree, G. Solar FAQs. (2006).
7. Levelized Cost of Energy and Levelized Cost of Storage 2019. *Lazard.com* http://www.lazard.com/perspective/levelized-cost-of-energy-and-levelized-cost-of-storage-2019/.
8. Denholm, P., Ela, E., Kirby, B. & Milligan, M. The Role of Energy Storage with Renewable Electricity Generation. (2010).
9. Elgowainy, A. *et al.* Well-toWheels Analysis of Energy Use and Greenhouse Gas Emissions of Plug-In Hybrid Electric Vehicles. (2010).
10. Lohse-Busch, H. *et al.* Ambient Temperature (20°F, 72°F and 95°F) Impact on Fuel and Energy Consumption for Several Conventional Vehicles, Hybrid and Plug-In Hybrid Electric Vehicles and Battery Electric Vehicle. in 2013-01–1462 (2013). doi:10.4271/2013-01-1462.
11. Thomas, J. Drive Cycle Powertrain Efficiencies and Trends Derived from EPA Vehicle Dynamometer Results. *SAE Int. J. Passeng. Cars - Mech. Syst.* **7**, 1374–1384 (2014).

12. Energy Storage Monitor. (2019).

13. Zablocki, A. Fact Sheet: Energy Storage (2019). (2019).

14. Grid Energy Storage. (2013).

15. Hong, J., Park, S. & Chang, N. Accurate remaining range estimation for Electric vehicles. in *2016 21st Asia and South Pacific Design Automation Conference (ASP-DAC)* 781–786 (2016). doi:10.1109/ASPDAC.2016.7428106.

16. Yong, T. & Park, C. A qualitative comparative analysis on factors affecting the deployment of electric vehicles. *Energy Procedia* **128**, 497–503 (2017).

17. Barth, M., Jugert, P. & Fritsche, I. Still underdetected – Social norms and collective efficacy predict the acceptance of electric vehicles in Germany. *Transportation Research Part F: Traffic Psychology and Behaviour* **37**, 64–77 (2016).

18. Hidrue, M. K., Parsons, G. R., Kempton, W. & Gardner, M. P. Willingness to pay for electric vehicles and their attributes. *Resource and Energy Economics* **33**, 686–705 (2011).

19. White, L. V. & Sintov, N. D. You are what you drive: Environmentalist and social innovator symbolism drives electric vehicle adoption intentions. *Transportation Research Part A: Policy and Practice* **99**, 94–113 (2017).

20. Choi, J. W. & Aurbach, D. Promise and reality of post-lithium-ion batteries with high energy densities. *Nature Reviews Materials* **1**, 1–16 (2016).

21. Wang, Q., Jiang, L., Yu, Y. & Sun, J. Progress of enhancing the safety of lithium ion battery from the electrolyte aspect. *Nano Energy* **55**, 93–114 (2019).

22. Zhao, H. *et al.* Film-forming electrolyte additives for rechargeable lithium-ion batteries: progress and outlook. *Journal of Materials Chemistry A* **7**, 8700–8722 (2019).

23. Costa, C. M., Lee, Y.-H., Kim, J.-H., Lee, S.-Y. & Lanceros-Méndez, S. Recent advances on separator membranes for lithium-ion battery applications: From porous membranes to solid electrolytes. *Energy Storage Materials* **22**, 346–375 (2019).

24. Wang, F. *et al.* Latest advances in supercapacitors: from new electrode materials to novel device designs. *Chemical Society Reviews* **46**, 6816–6854 (2017).

25. Castro Neto, A. H., Guinea, F., Peres, N. M. R., Novoselov, K. S. & Geim, A. K. The electronic properties of graphene. *Rev. Mod. Phys.* **81**, 109–162 (2009).

26. Neto, A. C., Guinea, F. & Peres, N. M. Drawing conclusions from graphene. *Phys. World* **19**, 33–37 (2006).

27. Lee, C., Wei, X., Kysar, J. W. & Hone, J. Measurement of the Elastic Properties and Intrinsic Strength of Monolayer Graphene. *Science* **321**, 385–388 (2008).

28. Luo, B. & Zhi, L. Design and construction of three dimensional graphene-based composites for lithium ion battery applications. *Energy & Environmental Science* **8**, 456–477 (2015).

29. Bard, A., J. & Faulkner, L. R. *Electrochemical Methods: Fundementals and Applications*. (John Wiley & Sons, Inc., 2001).

30. Yang, Z. *et al.* Carbon nanotube- and graphene-based nanomaterials and applications in high-voltage supercapacitor: A review. *Carbon* **141**, 467–480 (2019).

31. Ghoniem, A. F. Needs, resources and climate change: Clean and efficient conversion technologies. *Progress in Energy and Combustion Science* **37**, 15–51 (2011).

32. Yoon, Y. *et al.* Anti-Solvent Derived Non-Stacked Reduced Graphene Oxide for High Performance Supercapacitors. *Advanced Materials* **25**, 4437–4444 (2013).

33. Cao, X., Yin, Z. & Zhang, H. Three-dimensional graphene materials: preparation, structures and application in supercapacitors. *Energy & Environmental Science* **7**, 1850–1865 (2014).

34. Wu, Y., Yuan, X., Zhao, S. & van Ree, T. Introduction. in *Lithium-Ion Batteries: Fundementals and Applications* (CRC Press Taylor and Francis Group, 2015).

35. Winter, M., Besenhard, J. O., Spahr, M. E. & Novák, P. Insertion Electrode Materials for Rechargeable Lithium Batteries. *Advanced Materials* **10**, 725–763 (1998).

36. Zheng, T., Reimers, J. N. & Dahn, J. R. Effect of turbostratic disorder in graphitic carbon hosts on the intercalation of lithium. *Phys. Rev. B* **51**, 734–741 (1995).

37. Yoo, E. *et al.* Large Reversible Li Storage of Graphene Nanosheet Families for Use in Rechargeable Lithium Ion Batteries. *Nano Lett.* **8**, 2277–2282 (2008).

38. Novoselov, K. S. *et al.* Electric Field Effect in Atomically Thin Carbon Films. *Science* **306**, 666–669 (2004).

39. Hernandez, Y. *et al.* High-yield production of graphene by liquid-phase exfoliation of graphite. *Nature Nanotechnology* **3**, 563–568 (2008).

40. Xu, Y., Cao, H., Xue, Y., Li, B. & Cai, W. Liquid-Phase Exfoliation of Graphene: An Overview on Exfoliation Media, Techniques, and Challenges. *Nanomaterials* **8**, 942 (2018).

41. Tarcan, R. *et al.* Reduced graphene oxide today. *Journal of Materials Chemistry C* **8**, 1198–1224 (2020).

42. M. Abdelkader, A., J. Cooper, A., W. Dryfe, R. A. & A. Kinloch, I. How to get between the sheets: a review of recent works on the electrochemical exfoliation of graphene materials from bulk graphite. *Nanoscale* **7**, 6944–6956 (2015).

43. Shi, Q. *et al.* Substrate Developments for the Chemical Vapor Deposition Synthesis of Graphene. *Advanced Materials Interfaces* **7**, 1902024 (2020).

44. Bagley, J. D., Kishore Kumar, D., See, K. A. & Yeh, N.-C. Selective formation of pyridinic-type nitrogen-doped graphene and its application in lithium-ion battery anodes. *RSC Adv.* **10**, 39562–39571 (2020).

45. Bo, Z. *et al.* Plasma-enhanced chemical vapor deposition synthesis of vertically oriented graphene nanosheets. *Nanoscale* **5**, 5180–5204 (2013).

46. Yeh, N.-C., Hsu, C.-C., Bagley, J. & Tseng, W.-S. Single-step growth of graphene and graphene-based nanostructures by plasma-enhanced chemical vapor deposition. *Nanotechnology* **30**, 162001 (2019).

47. Geim, A. K. & Novoselov, K. S. The rise of graphene. in *Nanoscience and Technology* 11–19 (Co-Published with Macmillan Publishers Ltd, UK, 2009). doi:10.1142/9789814287005_0002.

48. Geim, A. K. Graphene: Status and Prospects. *Science* **324**, 1530–1534 (2009).

49. Nakada, K., Fujita, M., Dresselhaus, G. & Dresselhaus, M. S. Edge state in graphene ribbons: Nanometer size effect and edge shape dependence. *Phys. Rev. B* **54**, 17954–17961 (1996).

50. Wakabayashi, K., Fujita, M., Ajiki, H. & Sigrist, M. Electronic and magnetic properties of nanographite ribbons. *Phys. Rev. B* **59**, 8271–8282 (1999).

51. Han, M. Y., Özyilmaz, B., Zhang, Y. & Kim, P. Energy Band-Gap Engineering of Graphene Nanoribbons. *Phys. Rev. Lett.* **98**, 206805 (2007).

52. Kimouche, A. *et al.* Ultra-narrow metallic armchair graphene nanoribbons. *Nat. Comm.* **6**, 10177 (2015).

53. Ruffieux, P. *et al.* On-surface synthesis of graphene nanoribbons with zigzag edge topology. *Nature* **531**, 489–492 (2016).

54. Faccio, R., Denis, P. A., Pardo, H., Goyenola, C. & Mombrú, Á. W. Mechanical properties of graphene nanoribbons. *J. Phys.: Condens. Matter* **21**, 285304 (2009).

55. Xiang, C. *et al.* Functionalized Low Defect Graphene Nanoribbons and Polyurethane Composite Film for Improved Gas Barrier and Mechanical Performances. *ACS Nano* **7**, 10380–10386 (2013).

56. Behnam, A. *et al.* Transport in Nanoribbon Interconnects Obtained from Graphene Grown by Chemical Vapor Deposition. *Nano Lett.* **12**, 4424–4430 (2012).

57. Hwang, W. S. *et al.* Graphene nanoribbon field-effect transistors on wafer-scale epitaxial graphene on SiC substrates. *APL Materials* **3**, 011101 (2015).

58. Li, X., Wang, X., Zhang, L., Lee, S. & Dai, H. Chemically Derived, Ultrasmooth Graphene Nanoribbon Semiconductors. *Science* **319**, 1229–1232 (2008).

59. Wang, Q. *et al.* Fabrication and In Situ Transmission Electron Microscope Characterization of Free-Standing Graphene Nanoribbon Devices. *ACS Nano* **10**, 1475–1480 (2016).

60. Wang, Q. H. *et al.* Understanding and controlling the substrate effect on graphene electron-transfer chemistry via reactivity imprint lithography. *Nature Chemistry* **4**, 724–732 (2012).

61. Han, W., Kawakami, R. K., Gmitra, M. & Fabian, J. Graphene spintronics. *Nature Nanotechnology* **9**, 794–807 (2014).

62. Magda, G. Z. *et al.* Room-temperature magnetic order on zigzag edges of narrow graphene nanoribbons. *Nature* **514**, 608–611 (2014).

63. Grigorenko, A. N., Polini, M. & Novoselov, K. S. Graphene plasmonics. *Nature Photonics* **6**, 749–758 (2012).

64. Brar, V. W., Jang, M. S., Sherrott, M., Lopez, J. J. & Atwater, H. A. Highly Confined Tunable Mid-Infrared Plasmonics in Graphene Nanoresonators. *Nano Lett.* **13**, 2541–2547 (2013).

65. Brar, V. W. *et al.* Hybrid Surface-Phonon-Plasmon Polariton Modes in Graphene/Monolayer h-BN Heterostructures. *Nano Lett.* **14**, 3876–3880 (2014).

66. Myung, S. *et al.* Graphene-Encapsulated Nanoparticle-Based Biosensor for the Selective Detection of Cancer Biomarkers. *Advanced Materials* **23**, 2221–2225 (2011).

67. Jin, Z. *et al.* Metallized DNA nanolithography for encoding and transferring spatial information for graphene patterning. *Nature Communications* **4**, 1663 (2013).

68. Ahuja, P., Sharma, R. K. & Singh, G. Solid-state, high-performance supercapacitor using graphene nanoribbons embedded with zinc manganite. *J. Mater. Chem. A* **3**, 4931–4937 (2015).

69. Echtermeyer, T. J. *et al.* Strong plasmonic enhancement of photovoltage in graphene. *Nature Communications* **2**, 458 (2011).

70. Wang, X. & Dai, H. Etching and narrowing of graphene from the edges. *Nat. Chem.* **2**, 661–665 (2010).

71. Abramova, V., Slesarev, A. S. & Tour, J. M. Meniscus-Mask Lithography for Narrow Graphene Nanoribbons. *ACS Nano* **7**, 6894–6898 (2013).

72. Cai, J. *et al.* Atomically precise bottom-up fabrication of graphene nanoribbons. *Nature* **466**, 470–473 (2010).

73. Vo, T. H. *et al.* Large-scale synthesis of narrow graphene nanoribbons. *Nat. Comm.* **5**, 3189 (2014).

74. Chen, L., Hernandez, Y., Feng, X. & Müllen, K. From Nanographene and Graphene Nanoribbons to Graphene Sheets: Chemical Synthesis. *Angew. Chem. Int. Ed.* **51**, 7640–7654 (2012).

75. Narita, A. *et al.* Bottom-Up Synthesis of Liquid-Phase-Processable Graphene Nanoribbons with Near-Infrared Absorption. *ACS Nano* **8**, 11622–11630 (2014).

76. Daigle, M., Miao, D., Lucotti, A., Tommasini, M. & Morin, J.-F. Helically Coiled Graphene Nanoribbons. *Angewandte Chemie* **129**, 6309–6313 (2017).

77. Yang, W., Lucotti, A., Tommasini, M. & Chalifoux, W. A. Bottom-Up Synthesis of Soluble and Narrow Graphene Nanoribbons using Alkyne Benzannulations. *J. Am. Chem. Soc.* **138**, 9137–9144 (2016).

78. Goldfinger, M. B. & Swager, T. M. Fused Polycyclic Aromatics via Electrophile-Induced Cyclization Reactions: Applications to the Synthesis of Graphite Ribbons. *J. Am. Chem. Soc.* **116**, 7895–7896 (1994).

79. Jordan, R. S. *et al.* Synthesis of Graphene Nanoribbons via the Topochemical Polymerization and Subsequent Aromatization of a Diacetylene Precursor. *Chem* **1**, 78–90 (2016).

80. Sisto, T. J. *et al.* Long, Atomically Precise Donor–Acceptor Cove-Edge Nanoribbons as Electron Acceptors. *J. Am. Chem. Soc.* **139**, 5648–5651 (2017).

81. Genorio, B. *et al.* In Situ Intercalation Replacement and Selective Functionalization of Graphene Nanoribbon Stacks. *ACS Nano* **6**, 4231–4240 (2012).

82. Kosynkin, D. V. *et al.* Highly Conductive Graphene Nanoribbons by Longitudinal Splitting of Carbon Nanotubes Using Potassium Vapor. *ACS Nano* **5**, 968–974 (2011).

83. Wong, C. H. A., Chua, C. K., Khezri, B., Webster, R. D. & Pumera, M. Graphene Oxide Nanoribbons from the Oxidative Opening of Carbon Nanotubes Retain Electrochemically Active Metallic Impurities. *Angew. Chem. Int. Ed.* **52**, 8685–8688 (2013).

84. Ambrosi, A. *et al.* Graphene and its electrochemistry – an update. *Chemical Society Reviews* **45**, 2458–2493 (2016).

85. Hiramatsu, M. & Hori, M. *Carbon Nanowalls: Synthesis and Emerging Applications*. (Springer Science & Business Media, 2010).

86. Boyd, D. A. *et al.* Single-step deposition of high-mobility graphene at reduced temperatures. *Nature Communications* **6**, 6620 (2015).

87. Thermal Conductivity of Metals, Metallic Elements and Alloys. *The Engineering Toolbox* https://www.engineeringtoolbox.com/thermal-conductivity-metals-d_858.html.

88. Ferrari, A. C. *et al.* Raman Spectrum of Graphene and Graphene Layers. *Phys. Rev. Lett.* **97**, 187401 (2006).

89. Ferrari, A. C. Raman spectroscopy of graphene and graphite: Disorder, electron–phonon coupling, doping and nonadiabatic effects. *Solid State Communications* **143**, 47–57 (2007).

90. Dimiev, A. M. *et al.* Direct Real-Time Monitoring of Stage Transitions in Graphite Intercalation Compounds. *ACS Nano* **7**, 2773–2780 (2013).

91. Dimiev, A. M., Bachilo, S. M., Saito, R. & Tour, J. M. Reversible Formation of Ammonium Persulfate/Sulfuric Acid Graphite Intercalation Compounds and Their Peculiar Raman Spectra. *ACS Nano* **6**, 7842–7849 (2012).

92. Sun, Z. *et al.* Large-Area Bernal-Stacked Bi-, Tri-, and Tetralayer Graphene. *ACS Nano* **6**, 9790–9796 (2012).

93. Liu, Z. *et al.* The Application of Highly Doped Single-Layer Graphene as the Top Electrodes of Semitransparent Organic Solar Cells. *ACS Nano* **6**, 810–818 (2012).

94. Hsu, C.-L. *et al.* Layer-by-Layer Graphene/TCNQ Stacked Films as Conducting Anodes for Organic Solar Cells. *ACS Nano* **6**, 5031–5039 (2012).

95. Kim, H. *et al.* Organic solar cells using CVD-grown graphene electrodes. *Nanotechnology* **25**, 014012 (2014).

96. Zhou, Y. *et al.* Quantitative secondary electron imaging for work function extraction at atomic level and layer identification of graphene. *Scientific Reports* **6**, 21045 (2016).

97. Cançado, L. G. *et al.* General equation for the determination of the crystallite size La of nanographite by Raman spectroscopy. *Appl. Phys. Lett.* **88**, 163106 (2006).

98. Malard, L. M., Pimenta, M. A., Dresselhaus, G. & Dresselhaus, M. S. Raman spectroscopy in graphene. *Physics Reports* **473**, 51–87 (2009).

99. Krupke, R., Hennrich, F., Löhneysen, H. v & Kappes, M. M. Separation of Metallic from Semiconducting Single-Walled Carbon Nanotubes. *Science* **301**, 344–347 (2003).

100. Vijayaraghavan, A. *et al.* Dielectrophoretic Assembly of High-Density Arrays of Individual Graphene Devices for Rapid Screening. *ACS Nano* **3**, 1729–1734 (2009).

101. Qi, Z. J. *et al.* Correlating Atomic Structure and Transport in Suspended Graphene Nanoribbons. *Nano Lett.* **14**, 4238–4244 (2014).

102. NIST Computational Chemistry Comparison and Benchmark DataBase.

103. Luo, Y.-R. *Comprehensive Handbook of Chemical Bond Energies*. (Taylor & Francis Group, LLC, 2007).

104. Hassouni, K., Silva, F. & Gicquel, A. Modelling of diamond deposition microwave cavity generated plasmas. *J. Phys. D: Appl. Phys.* **43**, 153001 (2010).

105. Innovating Clean Energy Technologies in Advanced Manufacturing. in *Quadrennial Technology Review 2015* (U. S. Department of Energy, 2015).

106. Benzene, 1,2-dichloro. *NIST Chemistry WebBook* https://webbook.nist.gov/cgi/cbook.cgi?ID=C95501&Units=SI&Mask=4&Type=ANTOINE&Plot=on#ANTOINE.

107. Liu, C., Yu, Z., Neff, D., Zhamu, A. & Jang, B. Z. Graphene-Based Supercapacitor with an Ultrahigh Energy Density. *Nano Lett.* **10**, 4863–4868 (2010).

108. Wu, Z.-S. *et al.* Three-Dimensional Nitrogen and Boron Co-doped Graphene for High-Performance All-Solid-State Supercapacitors. *Advanced Materials* **24**, 5130–5135 (2012).

109. Zhu, Y. *et al.* Carbon-Based Supercapacitors Produced by Activation of Graphene. *Science* **332**, 1537–1541 (2011).

110. Chen, S., Zhu, J., Wu, X., Han, Q. & Wang, X. Graphene Oxide−MnO2 Nanocomposites for Supercapacitors. *ACS Nano* **4**, 2822–2830 (2010).

111. Xia, J., Chen, F., Li, J. & Tao, N. Measurement of the quantum capacitance of graphene. *Nature Nanotechnology* **4**, 505–509 (2009).

112. Li, Y. *et al.* Fabrication of Flexible Microsupercapacitors with Binder-Free ZIF-8 Derived Carbon Films via Electrophoretic Deposition. *BCSJ* **93**, 176–181 (2019).

113. Nagashio, K., Nishimura, T., Kita, K. & Toriumi, A. Mobility Variations in Mono- and Multi-Layer Graphene Films. *Appl. Phys. Express* **2**, 025003 (2009).

114. Tang, J. *et al.* Bimetallic Metal-Organic Frameworks for Controlled Catalytic Graphitization of Nanoporous Carbons. *Scientific Reports* **6**, 30295 (2016).

115. Cataldo, F. *et al.* Graphene nanoribbons produced by the oxidative unzipping of single-wall carbon nanotubes. *Carbon* **48**, 2596–2602 (2010).

116. Li, D., Müller, M. B., Gilje, S., Kaner, R. B. & Wallace, G. G. Processable aqueous dispersions of graphene nanosheets. *Nature Nanotechnology* **3**, 101–105 (2008).

117. Wang, J., Manga, K. K., Bao, Q. & Loh, K. P. High-Yield Synthesis of Few-Layer Graphene Flakes through Electrochemical Expansion of Graphite in Propylene Carbonate Electrolyte. *J. Am. Chem. Soc.* **133**, 8888–8891 (2011).

118. Parvez, K. *et al.* Exfoliation of Graphite into Graphene in Aqueous Solutions of Inorganic Salts. *J. Am. Chem. Soc.* **136**, 6083–6091 (2014).

119. Wei, D. *et al.* Graphene from electrochemical exfoliation and its direct applications in enhanced energy storage devices. *Chemical Communications* **48**, 1239–1241 (2012).

120. Parvez, K. *et al.* Electrochemically Exfoliated Graphene as Solution-Processable, Highly Conductive Electrodes for Organic Electronics. *ACS Nano* **7**, 3598–3606 (2013).

121. Liu, Z. *et al.* Ultraflexible In-Plane Micro-Supercapacitors by Direct Printing of Solution-Processable Electrochemically Exfoliated Graphene. *Advanced Materials* **28**, 2217–2222 (2016).

122. Liu, Z. *et al.* Transparent Conductive Electrodes from Graphene/PEDOT:PSS Hybrid Inks for Ultrathin Organic Photodetectors. *Advanced Materials* **27**, 669–675 (2015).

123. Liu, X., Ma, T., Pinna, N. & Zhang, J. Two-Dimensional Nanostructured Materials for Gas Sensing. *Advanced Functional Materials* **27**, 1702168 (2017).

124. Märkle, W., Tran, N., Goers, D., Spahr, M. E. & Novák, P. The influence of electrolyte and graphite type on the PF6- intercalation behaviour at high potentials. *Carbon* **47**, 2727–2732 (2009).

125. Winter, M., Wrodnigg, G. H., Besenhard, J. O., Biberacher, W. & Novák, P. Dilatometric Investigations of Graphite Electrodes in Nonaqueous Lithium Battery Electrolytes. *J. Electrochem. Soc.* **147**, 2427 (2000).

126. Wulan Septiani, N. L. *et al.* Self-assembly of nickel phosphate-based nanotubes into two-dimensional crumpled sheet-like architectures for high-performance asymmetric supercapacitors. *Nano Energy* **67**, 104270 (2020).

127. Makino, S., Yamauchi, Y. & Sugimoto, W. Synthesis of electro-deposited ordered mesoporous RuOx using lyotropic liquid crystal and application toward micro-supercapacitors. *Journal of Power Sources* **227**, 153–160 (2013).

128. Hsu, C.-C. *et al.* High-yield single-step catalytic growth of graphene nanostripes by plasma enhanced chemical vapor deposition. *Carbon* **129**, 527–536 (2018).

129. Xu, W. & Lee, T.-W. Recent progress in fabrication techniques of graphene nanoribbons. *Mater. Horiz.* **3**, 186–207 (2016).

130. Ferrari, A. C. & Basko, D. M. Raman spectroscopy as a versatile tool for studying the properties of graphene. *Nature Nanotechnology* **8**, 235–246 (2013).

131. Ferrari, A. C. & Robertson, J. Interpretation of Raman spectra of disordered and amorphous carbon. *Phys. Rev. B* **61**, 14095–14107 (2000).

132. Yang, D.-Q. & Sacher, E. Carbon 1s X-ray Photoemission Line Shape Analysis of Highly Oriented Pyrolytic Graphite: The Influence of Structural Damage on Peak Asymmetry. *Langmuir* **22**, 860–862 (2006).

133. Blume, R. *et al.* Characterizing Graphitic Carbon with X-ray Photoelectron Spectroscopy: A Step-by-Step Approach. *ChemCatChem* **7**, 2871–2881 (2015).

134. Kovtun, A. *et al.* Accurate chemical analysis of oxygenated graphene-based materials using X-ray photoelectron spectroscopy. *Carbon* **143**, 268–275 (2019).

135. Major, G. H. *et al.* Advanced Line Shapes in X-Ray Photoelectron Spectroscopy II.The Finite Lorentzian (LF) Line Shape (with some MATLAB code illustrating the use of the subplot function). *Vacuum Technology & Coating* 35–39 (2020).

136. *Peak Model for Highly Oriented Pyrolytic Graphite (HOPG) in CasaXPS*. (CasaXPS Casa Software).

137. Díaz, J., Paolicelli, G., Ferrer, S. & Comin, F. Separation of the ${\mathit{sp}}^{3}$ and ${\mathit{sp}}^{2}$ components in the C1s photoemission spectra of amorphous carbon films. *Phys. Rev. B* **54**, 8064–8069 (1996).

138. Singh, B., Hesse, R. & Linford, M. R. Good Practices for XPS (and other Types of) Peak Fitting. *Vacuum Technology & Coating* 2–7 (2015).

139. Darmstadt, H. & Roy, C. Surface spectroscopic study of basic sites on carbon blacks. *Carbon* **41**, 2662–2665 (2003).

140. Conway, B. E. *Electrochemical Supercapacitors: Scientific Fundementals and Technological Applications*. (Kluwer Academic/Plenum Publishers, 1999).

141. Lian, P. *et al.* Large reversible capacity of high quality graphene sheets as an anode material for lithium-ion batteries. *Electrochimica Acta* **55**, 3909–3914 (2010).

142. Seel, J. A. & Dahn, J. R. Electrochemical Intercalation of PF 6 into Graphite. *J. Electrochem. Soc.* **147**, 892 (2000).

143. Etacheri, V., Marom, R., Elazari, R., Salitra, G. & Aurbach, D. Challenges in the development of advanced Li-ion batteries: a review. *Energy & Environmental Science* **4**, 3243–3262 (2011).

144. Murmann, P. *et al.* Electrochemical Performance and Thermal Stability Studies of Two Lithium Sulfonyl Methide Salts in Lithium-Ion Battery Electrolytes. *J. Electrochem. Soc.* **162**, A1738 (2015).

145. Bisquert, J. & Compte, A. Theory of the electrochemical impedance of anomalous diffusion. *Journal of Electroanalytical Chemistry* **499**, 112–120 (2001).

146. Sharifi-Viand, A., Mahjani, M. G. & Jafarian, M. Investigation of anomalous diffusion and multifractal dimensions in polypyrrole film. *Journal of Electroanalytical Chemistry* **671**, 51–57 (2012).

147. Ko, M. *et al.* Scalable synthesis of silicon-nanolayer-embedded graphite for high-energy lithium-ion batteries. *Nature Energy* **1**, 1–8 (2016).

148. Shan, H. *et al.* Sulfur/Nitrogen Dual-doped Porous Graphene Aerogels Enhancing Anode Performance of Lithium Ion Batteries. *Electrochimica Acta* **205**, 188–197 (2016).

149. Xing, Z. *et al.* One-pot hydrothermal synthesis of Nitrogen-doped graphene as high-performance anode materials for lithium ion batteries. *Scientific Reports* **6**, 26146 (2016).

150. Wu, Z.-S., Ren, W., Xu, L., Li, F. & Cheng, H.-M. Doped Graphene Sheets As Anode Materials with Superhigh Rate and Large Capacity for Lithium Ion Batteries. *ACS Nano* **5**, 5463–5471 (2011).

151. Zhang, C., Mahmood, N., Yin, H., Liu, F. & Hou, Y. Synthesis of Phosphorus-Doped Graphene and its Multifunctional Applications for Oxygen Reduction Reaction and Lithium Ion Batteries. *Advanced Materials* **25**, 4932–4937 (2013).

152. Xu, J. *et al.* Edge-Selectively Halogenated Graphene Nanoplatelets (XGnPs, X = Cl, Br, or I) Prepared by Ball-Milling and Used as Anode Materials for Lithium-Ion Batteries. *Advanced Materials* **26**, 7317–7323 (2014).

153. Ma, X., Ning, G., Sun, Y., Pu, Y. & Gao, J. High capacity Li storage in sulfur and nitrogen dual-doped graphene networks. *Carbon* **79**, 310–320 (2014).

154. Wang, H. *et al.* Nitrogen -doped graphene nanosheets with excellent lithium storage properties. *Journal of Materials Chemistry* **21**, 5430–5434 (2011).

155. Wang, H., Maiyalagan, T. & Wang, X. Review on Recent Progress in Nitrogen-Doped Graphene: Synthesis, Characterization, and Its Potential Applications. *ACS Catal.* **2**, 781–794 (2012).

156. Shao, Y. *et al.* Nitrogen-doped graphene and its electrochemical applications. *J. Mater. Chem.* **20**, 7491–7496 (2010).

157. Reddy, A. L. M. *et al.* Synthesis Of Nitrogen-Doped Graphene Films For Lithium Battery Application. *ACS Nano* **4**, 6337–6342 (2010).

158. Ma, C., Shao, X. & Cao, D. Nitrogen -doped graphene nanosheets as anode materials for lithium ion batteries: a first-principles study. *Journal of Materials Chemistry* **22**, 8911–8915 (2012).

159. Bang, G. S. *et al.* Pyridinic-N-Doped Graphene Paper from Perforated Graphene Oxide for Efficient Oxygen Reduction. *ACS Omega* **3**, 5522–5530 (2018).

160. Mombeshora, E. T., Ndungu, P. G. & Nyamori, V. O. The physicochemical properties and capacitive functionality of pyrrolic- and pyridinic-nitrogen, and boron-doped reduced graphene oxide. *Electrochimica Acta* **258**, 467–476 (2017).

161. Yasuda, S., Yu, L., Kim, J. & Murakoshi, K. Selective nitrogen doping in graphene for oxygen reduction reactions. *Chem. Commun.* **49**, 9627–9629 (2013).

162. Yang, S.-Y. *et al.* A powerful approach to fabricate nitrogen-doped graphene sheets with high specific surface area. *Electrochemistry Communications* **14**, 39–42 (2012).

163. Wisitsoraat, A., Phokaratkul, D., Maturos, T., Jaruwongrangsee, K. & Tuantranont, A. Synthesis and characterization of nitrogen-doped 3D graphene foam prepared by inductively-coupled plasma-assisted chemical vapor deposition. in *2015 IEEE 15th International Conference on Nanotechnology (IEEE-NANO)* 89–92 (2015). doi:10.1109/NANO.2015.7388764.

164. Luo, Z. *et al.* Pyridinic N doped graphene : synthesis, electronic structure, and electrocatalytic property. *Journal of Materials Chemistry* **21**, 8038–8044 (2011).

165. Fox, D. *et al.* Helium ion microscopy of graphene: beam damage, image quality and edge contrast. *Nanotechnology* **24**, 335702 (2013).

166. Das, A. *et al.* Monitoring dopants by Raman scattering in an electrochemically top-gated graphene transistor. *Nature Nanotechnology* **3**, 210–215 (2008).

167. Green, J. H. S., Kynaston, W. & Paisley, H. M. Vibrational spectra of monosubstituted pyridines. *Spectrochimica Acta* **19**, 549–564 (1963).

168. Jackson, S. T. & Nuzzo, R. G. Determining hybridization differences for amorphous carbon from the XPS C 1s envelope. *Applied Surface Science* **90**, 195–203 (1995).

169. Tanuma, S., Powell, C. J. & Penn, D. R. Calculations of electorn inelastic mean free paths. II. Data for 27 elements over the 50–2000 eV range. *Surface and Interface Analysis* **17**, 911–926 (1991).

170. Papirer, E., Lacroix, R., Donnet, J.-B., Nansé, G. & Fioux, P. XPS study of the halogenation of carbon black—Part 2. Chlorination. *Carbon* **33**, 63–72 (1995).

171. Verma, P., Maire, P. & Novák, P. A review of the features and analyses of the solid electrolyte interphase in Li-ion batteries. *Electrochimica Acta* **55**, 6332–6341 (2010).

172. NIST X-ray Photoelectron Spectroscopy Database.

173. Fu, H. *et al.* Synergistic Effect of Nitrogen Dopants on Carbon Nanotubes on the Catalytic Selective Epoxidation of Styrene. *ACS Catal.* **10**, 129–137 (2020).

174. Ning, X. *et al.* Electronic synergism of pyridinic- and graphitic-nitrogen on N-doped carbons for the oxygen reduction reaction. *Chemical Science* **10**, 1589–1596 (2019).

175. Dong, F., Cai, Y., Liu, C., Liu, J. & Qiao, J. Heteroatom (B, N and P) doped porous graphene foams for efficient oxygen reduction reaction electrocatalysis. *International Journal of Hydrogen Energy* **43**, 12661–12670 (2018).

176. Augustine, C. *et al.* Renewable Electrcity Generation and Storage Technologies. Vol 2. of Renewable Electricity Futures Report. (2012).

177. Shin, W. H., Jeong, H. M., Kim, B. G., Kang, J. K. & Choi, J. W. Nitrogen-Doped Multiwall Carbon Nanotubes for Lithium Storage with Extremely High Capacity. *Nano Lett.* **12**, 2283–2288 (2012).

178. Li, W., Sun, X. & Yu, Y. Si-, Ge-, Sn-Based Anode Materials for Lithium-Ion Batteries: From Structure Design to Electrochemical Performance. *Small Methods* **1**, 1600037 (2017).

179. Hyeong Lee, J. *et al.* High-energy-density lithium-ion battery using a carbon-nanotube–Si composite anode and a compositionally graded Li[Ni 0.85 Co 0.05 Mn 0.10]O 2 cathode. *Energy & Environmental Science* **9**, 2152–2158 (2016).

180. Luo, Z., Xiao, Q., Lei, G., Li, Z. & Tang, C. Si nanoparticles/graphene composite membrane for high performance silicon anode in lithium ion batteries. *Carbon* **98**, 373–380 (2016).

181. Zhang, S. J. *et al.* Opening the band gap of graphene through silicon doping for the improved performance of graphene/GaAs heterojunction solar cells. *Nanoscale* **8**, 226–232 (2015).

182. Wang, Z. *et al.* Synthesis of silicon-doped reduced graphene oxide and its applications in dye-sensitive solar cells and supercapacitors. *RSC Adv.* **6**, 15080–15086 (2016).

183. Lv, R. *et al.* Large-Area Si-Doped Graphene: Controllable Synthesis and Enhanced Molecular Sensing. *Advanced Materials* **26**, 7593–7599 (2014).

184. Guo, H.-A. *et al.* Silicon- and oxygen-codoped graphene from polycarbosilane and its application in graphene/n-type silicon photodetectors. *Applied Surface Science* **464**, 125–130 (2019).

185. Rozel, P. *et al.* Properties of Nitrogen/Silicon Doped Vertically Oriented Graphene Produced by ICP CVD Roll-to-Roll Technology. *Coatings* **9**, 60 (2019).

186. Goncalves, A. M. B., Malachias, A., Mazzoni, M. S., Lacerda, R. G. & Magalhães-Paniago, R. Metastable phase formation and structural evolution of epitaxial graphene grown on SiC(100) under a temperature gradient. *Nanotechnology* **23**, 175603 (2012).

187. Wang, Z. *et al.* Synthesis, characterization and electrical properties of silicon-doped graphene films. *Journal of Materials Chemistry C* **3**, 6301–6306 (2015).

188. Liu, Z. *et al.* Novel silicon-doped, silicon and nitrogen-codoped carbon nanomaterials with high activity for the oxygen reduction reaction in alkaline medium. *J. Mater. Chem. A* **3**, 3289–3293 (2015).

189. Jafari, R. & Sohrabi, B. The Hydrophobicity of Doped Graphene by the Fourth Group Elements of the Periodic Table: Theoretical and Computational Studies. *J. Phys. Chem. C* **123**, 24837–24845 (2019).

190. Gholizadeh, R. & Yu, Y.-X. Work Functions of Pristine and Heteroatom-Doped Graphenes under Different External Electric Fields: An ab Initio DFT Study. *J. Phys. Chem. C* **118**, 28274–28282 (2014).

191. Eckmann, A. *et al.* Probing the Nature of Defects in Graphene by Raman Spectroscopy. *Nano Lett.* **12**, 3925–3930 (2012).

192. Singh, B. *et al.* Uniqueness plots: A simple graphical tool for identifying poor peak fits in X-ray photoelectron spectroscopy. *Applied Surface Science* **387**, 155–162 (2016).

193. Smith, K. L. & Black, K. M. Characterization of the treated surfaces of silicon alloyed pyrolytic carbon and SiC. *Journal of Vacuum Science & Technology A* **2**, 744–747 (1984).

194. Takagaki, T., Igari, Y., Takaoka, T. & Kusunoki, I. XPS study of the reaction of the Si(100) surface with a C2H4 beam. *Applied Surface Science* **92**, 287–290 (1996).

195. Gupta, N. *et al.* Synthesis of nano-crystalline germanium carbide using radio frequency magnetron sputtering. *Thin Solid Films* **592**, 162–166 (2015).

196. NIST X-ray Photoelectron Spectroscopy Database; Si 2p Doublet Separation.

197. NIST X-ray Photoelectron Spectroscopy Database; Si 2p3/2.

198. NIST X-ray Photoelectron Spectroscopy Database; Ge 3p Doublet Separation.

199. NIST X-ray Photoelectron Spectroscopy Database; Ge 3p3/2.

200. NIST X-ray Photoelectron Spectroscopy Database; Sn 3d Doublet Separation.

201. NIST X-ray Photoelectron Spectroscopy Database; Sn 3d5/2.

202. Lin, J. *et al.* Pomegranate-Like Silicon/Nitrogen-doped Graphene Microspheres as Superior-Capacity Anode for Lithium-Ion Batteries. *Electrochimica Acta* **215**, 667–673 (2016).

203. Joo, J. *et al.* Porous silicon–graphene oxide core–shell nanoparticles for targeted delivery of siRNA to the injured brain. *Nanoscale Horizons* **1**, 407–414 (2016).

204. Mo, R., Rooney, D., Sun, K. & Yang, H. Y. 3D nitrogen-doped graphene foam with encapsulated germanium/nitrogen-doped graphene yolk-shell nanoarchitecture for high-performance flexible Li-ion battery. *Nature Communications* **8**, 13949 (2017).

205. Wang, B. *et al.* Facile synthesis of the sandwich-structured germanium/reduced graphene oxide hybrid: an advanced anode material for high-performance lithium ion batteries. *Journal of Materials Chemistry A* **5**, 13430–13438 (2017).

206. Rouhani, M. DFT study on adsorbing and detecting possibility of cyanogen chloride by pristine, B, Al, Ga, Si and Ge doped graphene. *Journal of Molecular Structure* **1181**, 518–535 (2019).

207. Harris, P. J. F. Structure of non-graphitising carbons. *International Materials Reviews* **42**, 206–218 (1997).